Universiteit Gent
Faculteit Wetenschappen
Vakgroep Fysica en Sterrenkunde

Mathematical modelling of structure and function of the cardiac left ventricle

Sergei Pravdin

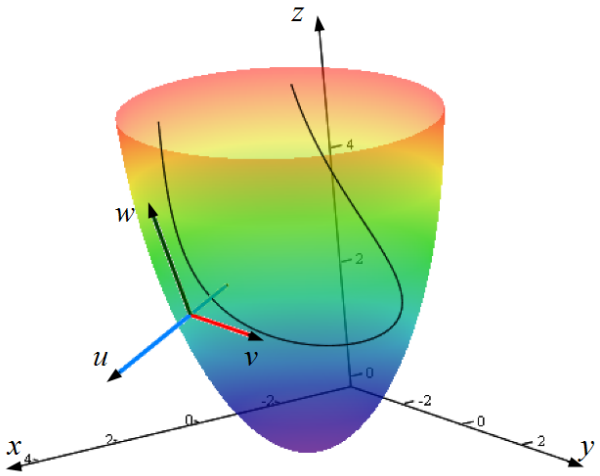

Proefschrift tot het behalen van de graad van
Doctor in de Wetenschappen:
Fysica
Academiejaar 2014-2015

Universiteit Gent
Faculteit Wetenschappen
Vakgroep Fysica en Sterrenkunde

Promotor: Prof. A.V. Panfilov (Universiteit Gent)
Co-promotoren: Prof. V.S. Markhasin (Instituut voor Immunologie en Physiologie, Jekaterinenburg, Rusland),
Prof. V.I. Berdyshev (Instituut voor Wiskunde en Mechanica, Jekaterinenburg, Rusland)

Universiteit Gent
Faculteit Wetenschappen

Vakgroep Fysica en Sterrenkunde
Krijgslaan 281, S9 (WE05), B-9000 Gent, België

Dit werk kwam tot stand met de steun van het
Bijzonder Onderzoeksfonds (BOF) – Universiteit Gent.

Faculteit Wetenschappen

Proefschrift tot het behalen van de graad van
Doctor in de Wetenschappen:
Fysica
Academiejaar 2014-2015

Acknowledgements

I would like to thank

- my promotors V.I. Berdyshev, V.S. Markhasin, A.V. Panfilov;
- my colleagues from Institute of Mathematics and Mechanics named after N.N. Krasovskij (Ekaterinburg, Russia) P.A. Vasev, A.A. Koshelev, A.V. Sozykin, Yu.N. Subbotin, O.V. Ushakova, M.A. Chernoskutov, S.V. Scharf;
- from Institute of Immunology and Physiology (Ekaterinburg, Russia) V.S. Zverev, L.B. Katsnelson, O.E. Solovyova;
- from Ghent University (Belgium) B. Verhegghe, H. Verschelde, A. Defauw, H. Dierckx, G. Nootens;
- from Hangzhou Normal University (China) B.-W. Li;
- from Institute of Continuous Media Mechanics (Perm, Russia) I.N. Shardakov;
- from Institute of Mechanics (Moscow State University named after M.V. Lomonosov), A.K. Tsaturyan

for assistanse in my research and valuable remarks during our discussions.

Contents

List of Figures

List of Acronyms

LV, left ventricle.

DT(I): diffusion tensor (imaging).

MRI: magnetic resonance imaging.

CT: computer tomography.

GF: generating function.

ESS: ε-spiral surface.

RP: resting potential.

IVS: interventricular septum.

AP: action potential.

Terminology

Action potential is a phenomenon in an electrically excitable cell that occurs when its transmembrane potential changes from the resting potential and returns to the resting value after some event such as passing an ionic current or mechanical deformation.

Left ventricle is the most powerful, thickest and most responsible cardiac chamber, which obtains arterial blood from the left atrium and pumps blood to the aorta.

Left ventricle base is the upper part of the chamber that contacts with the left atrium and aorta and is separated from them by fibrous ring and mitral and aortal valves.

Cardiac apex is its caudal (lower) part where the bottom of the left ventricle is situated; the ventricular fibres make the vortex cordis, or cardiac whirpool.

Interventricular septum is the muscular wall separating the two ventricles and formed by two or three layers of myocardium with different fibre direction patterns.

Cardiomyocite is a cardiac muscular cell which can propagate an electrical signal and contract when electrically excited.

Transmembrane potential of a cell is the difference in potential between the intracellular and extracellular space.

Cleavage plane is a fibrous tissue surface separating two layers of myocardium.

Myofibre is a muscular fibre; in the case of the heart, splitting and merging myofibres form a complex three-dimensional net.

Reaction-diffusion system is a system of one partial and several ordinary differential equations having a special term, Laplacian, and describing processes of spread (diffusion) of matter or a characteristic in an excitable (reaction) medium.

Nederlandstalige samenvatting

Een van de meest boeiende studiegebieden in de klinische medicijnwetenschappen is deze die onderzoek doet naar de normale en abnormale functie van het hart. Een zeer interessante recente ontwikkeling in dit gebied is het gebruik van 'multiscale' modelleer methoden. Deze methoden bleken zeer effectief te zijn om de mechanismen van hartritmestroornissen te begrijpen. Hartritmestoornissen zijn de grootste doodsoorzaak in de geïndustrialiseerde wereld. Ze worden veroorzaakt door abnormale excitatie van het hart en de vorming van vortices in hartweefsel. Een van de belangrijkste problemen in de bestudering ervan, is dat ze zich voordoen op het niveau van het hele orgaan. De relatie tussen cellulaire processen en de initiatie van hartritmestoornissen is hierdoor niet triviaal. Belangrijke bijdragen tot dit onderzoeksgebied werden bekomen door gebruik te maken van 'multiscale' modelleer methoden, waarbij het hart beschreven wordt door 'multiscale' modellen die het cellulaire en het hele orgaan niveau integreren. Deze modellen kunnen gebruikt worden om de mechanismen van initiatie van hartritmestoornissen te bestuderen, en om te onderzoeken hoe variaties op het cellulaire niveau deze initiatie beïnvloedt.

Om dergelijke 'multiscale' modellen te bouwen, moeten modellen van hartcellen gecombineerd worden met structurele data van de anatomie van het hart. De ontwikkeling van hartcel modellen begon in 1962, met het klassieke Noble model voor Purkinje vezels van het hart. Tegenwoordig is dit een sterk ontwikkeld onderzoeksgebied en vele modellen, van verschillende complexiteit, zijn beschikbaar.

Dit in tegenstelling tot anatomische modellen, van welke er veel minder beschikbaar zijn. De grootste moeilijkheid bij het opbouwen van dergelijke modellen is de karakterisatie van de anisotropie van hartweefsel. Deze anisotropie is een van de belangrijkste factoren die de golfpropagatie beïnvloedt in het hart.

Het doel van deze thesis is om analytische modellen voor de anisotropie van het hart op te bouwen, en dit in een anatomische accurate setting. Deze modellen gebruiken we dan om zowel normale excitatie van het hart als hartritmestoornissen te bestuderen. In de volgende paragrafen overlopen we de structuur van deze thesis.

Na een inleiding als het eerste hoofdstuk, in het tweede hoofdstuk introduceren we een theoretisch 'rule-based' model voor de anatomie en vezelrichting van de linker ventrikel (LV) van het hart. We vergelijken dit model ook met experimentele data. We stellen een expliciete analytische formulering voor die ons in staat stelt om de vorm en het vezel richting veld van de LV te beschrijven. Het concept van de ventriculaire 'band' architectuur was gegeven door Torrent-Gausp. In onze benadering, is de anisotropie van het hart afgeleid van enkele algemene principes. We veronderstellen dat de LV kan geconstrueerd worden als een set van identieke spiraal oppervlakken. Elk van deze oppervlakken worden op hun beurt bekomen door de rotatie van een zekere curve rond de verticale as. Deze spiraal oppervlakken zijn gevuld met niet snijdende curven, welke myocardium vezels voorstellen. Deze constructie wordt uitgevoerd in een speciaal coördinaten systeem, vastgelegd door de vorm van de LV.

Om ons model te verifiëren, gebruiken we experimentele data van de vezel richting van zowel menselijke als honden harten. We stellen vast dat er een goeie kwalititatieve overeenkomst is met de experimentele data.

In het derde hoofdstuk, ontwikkelen we een numerieke benadering voor ons anatomisch model. Gebaseerd op de analytische beschrijving en het speciale curvilineaire coördinaatsysteem, formuleren we een numerieke benadering voor het construeren van een 'mesh'. Dit gebruiken we dan om het reactie-diffusie systeem dat hartcellen beschrijft numeriek te integreren. Met het anatomische model worden op die manier elektrofysiologische simulaties uitgevoerd op een rechthoekig

'grid'. We passen onze methode toe om het effect van vezel rotatie en elektrische anisotropie van hartweefsel (i.e. de verhouding van de geleidingscoëfficiëten langs en dwars op de vezels) op golfpropagatie te bestuderen. Hiervoor gebruiken we het ten Tusscher–Noble–Noble–Panfilov (2006) ionische model voor menselijke hartcellen. We tonen aan dat de vezel richting de snelheid verhoogt waarmee het hart geactiveerd wordt, en het effect van anisotropie verzwakt. Onze resultaten tonen aan dat de vezel richting in het hart een belangrijke factor is tijdens activatie van het hart. Verder bestuderen we ook de initiële fasen van spiraalgolf dynamica, en demonstreren dat het corresponderende filament drift. We tonen aan dat de snelheid waarmee het filament drift niet monotonisch afhangt van de vezel rotatie hoek.

In het vierde hoofdstuk onderzoeken we in detail spiraalgolf dynamica in ons anatomisch model. We bestuderen op systematische wijze de dynamica van spiraalgolf filamenten, en dit zowel voor positieve als negatieve 'tension'. Ook beschouwen we verscheidene mogelijke vormen van de LV en verschillende graden van anisotropie van hartweefsel. We tonen dat voor positieve filament 'tension', de finale positie van het spiraalgolf filament hoofdzakelijk gedetermineerd is door de dikte van de hartwand. Hoewel, we observeren ook dat door anisotropie het filament naar de apex van de LV wordt aangetrokken. Voor negatieve filament 'tension' verbuigt het filament, en in de meeste gevallen drift het filament naar de apex van het hart. Dit zonder enig, of nauwelijks, verband met de dikte van de LV. We bespreken de mechanismen van de geobserveerde fenomenen, en hun implicaties voor hartritmestoornissen.

In het vijfde hoofdstuk formuleren we een niet axiaalsymmetrische LV anatomie op basis van Pettigrew's spiraal oppervlakken. Vergeleken met het model ontwikkeld in hoofdstuk 1, biedt deze formulering een meer accurate beschrijving van de anatomie van het hart, en kan het makkelijk aangepast worden, bijvoorbeeld in het geval het zou gebruikt worden voor patiënt specifieke modellering. In dit model zijn de ventrikels opgebouwd uit oppervlakken (welke myocardium 'sheets' modelleren). In elk oppervlak zijn de curven zo gedefinieerd dat ze tangen-

tieel liggen ten opzichte van de lokale myocardium richting. Na het fitten van de ventriculaire vorm aan de experimentele data afkomstig van menselijke en honden harten, worden de resulterende vezel orientatie hoeken, in een lokaal coördinatensyteem, uitgerekend in ons model. Deze berekende hoeken worden dan vergeleken met experimentele data over vezel orientatie. We bekomen een goede kwalitatieve – en in sommige LV gebieden – kwantitatieve overeenkomst tussen ons model en experimentele data. Dit model kan gebruikt worden voor het verifiëren van de 'band' hypothese; voor het uitvoeren van verschillende numerieke experimenten die focussen op de invloed van anisotropie op de elektrische excitatie; en voor de simulatie van de mechanische functie van het hart.

We sluiten de thesis af met een conclusie en een vooruitblik op toekomstige onderzoeksrichtingen. In dit laatste deel, generaliseren we de resultaten bekomen in deze thesis, en bespreken we de mogelijke toekomstige ontwikkeling van het model en toepassingen.

English summary

Studies of normal and abnormal cardiac function are among the most important in clinical medicine. One of the most exciting recent developments in this area is the application of multiscale modelling methods to these problems. These methods have turned out to be effective for understanding the mechanisms of cardiac arrhythmias. Cardiac arrhythmias remain the largest cause of death in the industrialized world. They are caused by the abnormal excitation of the heart and the formation of vortices in cardiac tissue. One of the main problems in studying them is that they occur at the level of whole organ, and thus, relation of cellular processes to the onset of the arrhythmias is non-trivial. Valuable contributions to that area are made using the multiscale modelling approach, in which the heart is described by multiscale models from the cellular to the whole organ level. Such models can be used to study the mechanisms of initiation of cardiac arrhythmias and to learn how the changes at the single-cell level affect the onset of arrhythmias.

In order to build such a multiscale model, one needs to combine models of cardiac cells with structural data on anatomy of the heart. The development of single cell cardiac models started in 1962 with the classic Noble model of Purkinje fibres of the heart. Currently, this is a well-developed area, and many models of cardiac cells of different complexity are available. The area of anatomical cardiac models is substantially less developed. The main problem here is to characterize the anisotropy of cardiac tissue, as it is one of the most important factors affecting the wave propagation in the heart.

The aim of this thesis is the development of an analytical model of cardiac anisotropy in an anatomically accurate setting and its application to study normal cardiac excitation and the processes involved with the formation of cardiac arrhythmias. The thesis is organized as follows.

After the Introduction as the first chapter, the second chapter introduces a theoretical rule-based model for the anatomy and fibre orientation of the left ventricle (LV) of the heart and compares it with experimental data. We propose an explicit analytical formulation that allows us to obtain the LV shape and its fibre direction field. The ventricle band concept of cardiac architecture was given by Torrent-Guasp. In our approach, anisotropy of the heart is derived from some general principles. We assume that the LV can be constructed as a set of identical spiral surfaces, each of which can be produced by the rotation of a certain curve around vertical axis. Each spiral surface is filled with non-intersecting curves which represent myocardial fibres. The complete construction is conducted in a special coordinate system set by the LV form. For model verification, we use experimental data on fibre orientation in human and canine hearts and show good qualitative agreement with experimental data.

In the third chapter, we develop a numerical approach for our anatomical model. Based on this analytical description and the special curvilinear coordinate system, we formulate a numerical approach for mesh constructing and use it for the numerical integration of the reaction-diffusion systems describing cardiac cells. With this anatomical model, electrophysiological simulations were performed on a rectangular coordinate grid. We apply our method to study the effect of fibre rotation and electrical anisotropy of cardiac tissue (i.e., the ratio of the conductivity coefficients along and across the myocardial fibres) on wave propagation using the ten Tusscher–Noble–Noble–Panfilov (2006) ionic model for human ventricular cells. We show that fibre rotation increases the speed of cardiac activation and attenuates the effects of anisotropy. Our results show that the fibre rotation in the heart is an important factor underlying cardiac excitation. We also study the initial

phases of scroll wave dynamics in our model and show the drift of a scroll wave filament whose velocity depends non-monotonically on the fibre rotation angle.

The fourth chapter deals with a detailed study of scroll waves in our anatomical model. Here, we perform a systematic study of the dynamics of scroll wave filaments for the cases of positive and negative tension in our anatomical model. We study the various possible shapes of the LV and different degrees of anisotropy of cardiac tissue. We show that for positive filament tension, the final position of the scroll wave filament is mainly determined by the thickness of the myocardial wall; however, anisotropy attracts the filament to the LV apex. For negative filament tension, the filament buckles, and in most cases, tends to approach the apex of the heart with no or slight dependency on the thickness of the LV. We discuss the mechanisms of the observed phenomena and their implications for cardiac arrhythmias.

The fifth chapter presents the formulation of a non-axisymmetric cardiac LV anatomy on the basis of Pettigrew's spiral surfaces. Compared to the model developed in Chapter One, it provides a more accurate description of cardiac anatomy and can be easily modified for patient-specific modelling. In that model, the ventricle is composed of surfaces which model myocardial sheets. In each surface, curves are defined that are tangential to the local myofibre direction. After fitting the ventricular shape to experimental data on human and canine hearts, the resulting fibre orientation angles in the local coordinate system are calculated in our model. The predicted angles are compared to experimental data on fibre orientation. A good qualitative and – in some LV wall areas – quantitative agreement between the model and experimental data is demonstrated. The model can be used both for the band hypothesis verification and for various numerical experiments studying influence of anisotropy on the electrical excitation spread and simulating cardiac mechanical function.

In the last part of the thesis, there is a conclusion and future work section. In this section, we generalize the results obtained in the thesis and discuss ways to further develop the model and its possible future applications.

1

Introduction

1.1 Integrative cardiac models

Integrative mathematical models of complicated hierarchic physiological systems, such as the heart, allow one using a computational mathematical approach to describe these systems at several levels, from the molecular level up to the macrolevel, which characterizes the structure and functions of the whole heart and/or certain chambers, including the LV. A comprehensive analysis of such models of the ventricle in the framework of the numerical experiments gives a way to elucidate mechanisms of the normal and pathological heart performance and to

predict potential methods of the effective therapy, for example, corrections of mechanical and electrical cardiac function disturbances.

Over the last few years, a number of models describing electrical and/or mechanical function of the whole heart or its chambers have been proposed [12, 35, 39, 47, 64, 68, 93, 106, 110, 115, 119, 120]. The most valuable of them are based on detailed description of cardiac anatomy and the fiber orientation field, which is crucial for a correct representation of the physiological function of the heart.

Two approaches for modelling the heart chamber architectonics (including the morphological pattern of the myocardium fibers' orientation) may be marked out. The approaches are more complementary to each other than alternative ones. For convenience, we quite roughly and non-rigorously assign them as empiric and theoretical approaches.

In the empiric approaches, fiber orientation is directly measured in the heart using various experimental techniques, and in theoretical approaches, fiber orientation is generated by some algorithms.

1.2 Examination of individual hearts and empirical models

Very important and useful empiric approach is represented in several well-developed published models [40, 63, 124]. The models are based on the detailed experimental mapping of individual hearts. Currently there are several experimental methods which can be used to measure fiber orientation in the heart. Particularly, Diffusion Tensor Imaging (DTI) technique was used to obtain the hearts' images with the fiber orientation. In this approach, the researcher finds the diffusion matrix coefficients of water molecules in the heart. Then it becomes available to calculate the three eigenvectors of the matrix. They are assumed to be the three main directions of anisotropy in the tussue: the fiber direction vector (the primary

eigenvector), the fiber normal in the sheet plane (the secondary one), and the sheet normal (the tertiary one). As these directions are assumed to be closely connected to the structure of the tissue, it gives us anisotropy of the heart [41, 42, 57, 121]. Such measurements can be done with spatial resolution up to 0.3–0.5 mm and in general produce high quality data which can be used in computer models. Then the images are fractioned as a set of segments with help of the 3D finite element mesh, and a prevailing direction of the fiber orientation in each element of this individual heart is found. Thus detailed 3D myofibers' direction fields are obtained, where every arrow indicates orientation of the myofibers lying near it. Very detailed description of the heart geometry is distinctive feature of these models. Careful experimental verification is also their undoubted virtue.

Another direct measurement of anisotropy can be done via the tedious histological studies of fiber direction in 3D [65, 105] where the researcher makes series of parallel slices of the investigating part of the heart. In every slice angles of fiber slope are measured. When all the angular values are composed, the researcher obtains a full picture of the fiber directions in the organ. More recently B. Smaill's group developed a combined high-resolution serial imaging microscopy technique [117]. This methode contains 5 phases: the first one is in vivo registration of the electrical activity of the heart with help of a set of electrodes, then the heart follows in vivo DT-MRI in order to allow reseachers to obtain its reference geometry. The third stage is pouring the heart with wax to fix it. This procedure brings some distortion to the shape of the 3D structure, so data from the 4th stage, the serial cutting and imaging, needs an inverse processing to level the distortion. The main merit of the technique is its ability to give the undistorted data to a researcher after the final, 5th, phase of the procedure, the computer correction of the data collected.

In [49] the myofibers in the second trimester fetal human heart are investigated using the method of quantitative polarized light microscopy. The hearts were embedded in a transparent resin, polymerized and then sectioned. Afterwards, the elevation and azimuth angles were measured by means of polarized light (see [49]

for any details). Finally, the authors suggested a novel “pretzel” qualitative cardiac model.

The start of quantitative approaches to animal and human heart anatomy describing was established by D. Streeter [105]. Note that all listed approaches are either based on or use results of classical studies of D. Streeter on fiber orientation in the human heart. Streeter not only measured fiber orientation in the heart, but also proposed several hypothesis how this fiber orientation could be reproduced using geometrical transformations. However, these ideas of Streeter were never formulated in a mathematical form.

The question of laminar arrangement in the muscular fibers and sheets is one of the basic matters in the cardiac anatomy. Such an arrangement is hard to measure and still under dabate [34,55,65]. We have not attempted to include it in our present description.

Every directly measured dataset is connected to one concrete patient or laboratory animal and thus cannot be directly used for personalized heart models. Therefore there is a demand for the algorithms which will allow projection of the existing data to any geometry (see e.g. [41]) or developing of algorithms which allows researchers to generate such fiber orientation field from any given geometry data.

At the same time, strictly speaking, any model built on the base of a particular arrow map is a model of one particular heart, as it is difficult to distinguish between the common properties of the heart of the given species and individual specificity of the scanned heart sample. Of course, individual computational models of the heart chamber architectonics built with help of the empirical approach may be developed further up to the species model level. Correct averaging of data obtained via the mapping of the individual heart samples will be necessary for this. Several promising works are being fulfilled in this way [32, 85, 86, 128]. The empiric species models might further, among other things, essentially contribute to the parameter verification of the models developed via the theoretical approach.

Each of the listed experimental methods allows researchers to obtain fiber orientation field and to use it to setup a model. And this is the best approach to study that particular heart for which the measurements were performed. However, in many cases a researcher needs not only to study given anisotropy, but has to be able to modify it, e.g. to study its effects on various electromechanical processes. In addition, in many cases just anatomy, but not fiber orientation is known and some algorithms are needed to build up the anisotropy. Such models are based on generic views on cardiac anatomy, which were obtained in cardiac research for more that 100 years of studies.

1.3 Theoretical models of cardiac anatomy

The theoretical approach to the modelling of the heart chamber architectonics, e.g. which of the LV, issues from the attempts to clarify a general principle (a governing rule) determining orientation of the fibers in the ventricle wall. Such theoretical models may be especially useful when studying basic mechanisms of the heart performance both in norm and pathology.

The discovery of the rotational anisotropy in the myocardium was one of the first fundamental findings in the qualitative heart anatomy. The tangents to the myofibers turn, if we look to them transmurally, and the turning angle equals approximately $120°$. Streeter compared this picture with Japanese fan [105]. Torrent-Guasp suggested considering the myocardium of both ventricles as a “flattened rope” or a band which has two endings and makes a few turns. According to Streeter [105], myofibers are geodesic lines on a set of nested toroids, and outer toroids are more prolate, inner ones are more round. Besides this model, there are many models concerning a few myocardial layers (more often 3 — superficial, middle and deep, see, for example [98]). One can find a more detailed description of the history of cardiac qualitative anatomy in the work [49].

One group of models constructs the architectonics of the myocardial fibers by using the analogy with the muscular sceletal fibers. Different models include

from 1 to 4 systems of myocardial bundles [11, 56, 59, 94, 112]. However, some researchers point to the restrictions of the approach [58, 100, 113].

Another attitude to the LV architectonics considers it as a kind of the vascular musculature, where many junctions between the fibers exist [31, 37, 44, 45, 54].

One of the key questions concerning the LV myocardium concerns its layers, namely their existence and, if they exist, their number and positions. As a rule, the models with sheets have a number of layers inserted one into another [98]. Nevertheless, there exists a layers-based model where their number is indefinite and they do not divide the LV to internal and external parts. We are talking about an early work [111], where Torrent-Guasp proposed a hypothesis on how the cardiac fiber orientation could be reproduced using geometrical transformations. However, this idea has never been formulated in mathematical terms.

Theoretical approaches include rule-based methods [10, 15, 101] or mappings of fibers from animal hearts to the human heart geometry [46]. One of the most recent rule-based methods is a Laplace–Dirichlet algorithm [10] which takes a noisy DTI-derived fiber orientation field as input data and yields, firstly, the transmural and apicobasal directions for the entire myocardium and, secondly, a smooth and continuous fiber orientation field. Another approach was used by Ch. Peskin, who derived fiber orientation field from the principles of mechanical equilibrium [83].

Chadwick considered a cylindrical LV and specified the helix angle linearly depending on point position in the LV wall [20]. Beyar et al. shaped LV into a spheroid and also used linear dependence of the helix angle on the distance between point and the endocardium [12].

An interesting example of the theoretical approach was developed by Theo Arts with coauthors in 1992 [16]. They constructed a model of an ellipsoidal LV, complicated the law of helix angle change to a sectionally quadratic one and quantified orientation of the muscle fibers via the helix fiber angle distribution which was found upon application of the mechanical adaptational principle suggested by Arts et al. in 1982 [8].

1.4 Relation to other anatomical ventricular models

Torrent-Guasp in [111] suggested that the LV can be represented as a set of embedded surfaces, i.e. muscular layers, covered by curves representing the myofibers. This idea was illustrated using Pettigrew's proposal of the surface in form of a planar semicircle with a number of curves drawn on it, which was thereafter transformed to a conical surface. Finally, the heart was considered as a family of such conical surfaces inserted to each other. Unfortunately, Torrent-Guasp's procedure was never explicitly parametrized and of course in its classical way conical surfaces could not provide a proper representation of the LV geometry. It may be noted that Streeter mentioned these ideas as very important, but did not formalize them.

In the first chapter, we propose an analytical formulation based on the Torrent-Guasp's anatomical concept. In particular, we develop a description of heart anatomy using a family of inserted non-conical surfaces, which allows us to represent smooth geometry of the LV properly. Moreover, we use a family of lines predefined at these surfaces to represent cardiac fibers. The entire model can be expressed in terms of analytical functions. We describe the details of model construction and compare its output with experimental measurements of anisotropy in the human and canine LV.

2

Axisymmetrical model of the left ventricle shape and anisotropy

2.1 Background

The results described in this chapter have been published in [88].

In this chapter, we suggest a theoretical model for anatomy and fibre orientation of the LV. The model is based on the ventricle band concept of cardiac architecture given by Torrent-Guasp [111]. In 1972, Torrent-Guasp proposed an

anatomic concept in which both right and left heart ventricles were considered segments of a single myofibre band twisted and wrapped into a double helical coil [111]. Since that time, this concept has been a subject of intense discussion. Many cardiac anatomists [5,6] consider the Torrent-Guasp hypothesis a gross simplification, and a number of imaging scientists propose a more complex organization of the LV micro-architecture [55]. Another group of researchers has a favorable view on the ventricle band concept [18,22,53]. For example, an article signed by more than 20 prominent scientists [17] concludes that 'models such as that of Torrent-Guasp et al., which proposes conduction along fibre orientation in a single muscular band and defies conventional concepts of activation, should be investigated'. In spite of that interest, the Torrent-Guasp model was never formalized and compared to data on measured cardiac anatomy. Note that in our view, features of the model, such as the possibility of representing realistic fibre orientations by a single warped band, can be proved or disproved only by means of mathematical modeling. Regardless of the outcome, such a formulation will be useful.

We follow Torrent-Guasp's approach to build cardiac anatomical models of increasing complexity that also use later measurements by Streeter [105]. We show that this description allows one to represent such properties of heart anisotropy as fibre rotation and its dependence on the latitude, spiralling of fibres at the apex and fibre's maximal angle of torsion about the LV axis. We also perform quantitative comparisons with data from Streeter [105] and Hunter [65], showing good correspondence of the measured fibre orientation fields with that given by our model.

In our model, both the anatomy and fibre orientation field are precisely formulated mathematically. This allows a researcher to apply analytical methods to investigate cardiac electrophysiology and mechanics. In addition, any variations in the shape of the LV and the anisotropy pattern can be reproduced easily by this approach.

2.2 Construction of the LV model

The description of the model consists of several steps, starting with simple shapes and approaching the final LV model. Initial steps follow the representation of Pettigrew's idea (one can see a copy of his figure in Streeter's work [105] (see figure 3)). We then modify its description and obtain the LV model.

A semicircle with chords

Pettigrew began his construction from a semicircle with a set of curves on it [84], as one can see in Streeter's paper ([105], figure 3 a). We describe the figure analytically as follows.

Consider a semicircle with radius K given in the polar coordinate system (P, Φ):

$$0 \le \mathrm{P} \le K, \quad 0 \le \Phi \le \pi. \tag{2.1}$$

Following Pettigrew [84], let us construct a sequence of horizontal chords (figure 2.1):

$$Y = \text{const}, \ 0 < Y < K, \tag{2.2}$$

$$\Phi_0 := \arcsin \frac{Y}{K} \le \Phi \le \pi - \arcsin \frac{Y}{K} =: \Phi_1, \tag{2.3}$$

$$\mathrm{P}(\Phi) = \frac{Y}{\sin \Phi}. \tag{2.4}$$

Here, Φ_0 and Φ_1 are polar angles of the right and the left ends of a chord.

A global idea of the model is to wrap this semicircle onto a surface (e.g. conical). The curves will give fibre orientation on that surface, and then rotation of such a surface will give a 3-D structure of the heart. The first surface that we will construct is a simple cone. We use a semicircle and a cone because the possibility to wrap a sector of circle to a simple cone is a proven mathematical fact and the LV form closely resembles a cone. We consider the semicircle as the part of the Torrent-Guasp "unique myocardial band" which corresponds to the LV. After this wrapping, we will convert the cone to a more complex surface by a non-linear transformation which will allow us to obtain a more feasible LV model.

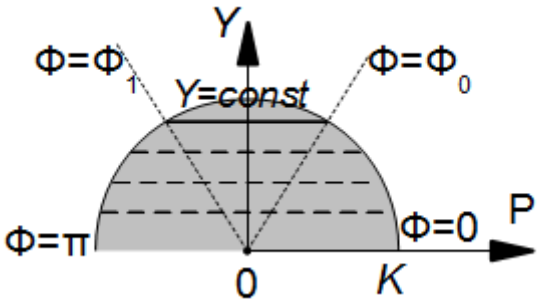

Figure 2.1: *Horizontal chords on the semicircle. The example chords are numbered so that they can be identified after transformations that will be shown below.*

Let us separate the conus slips so as for the base, change of ρ coordinate was equal 0 for the angle $\phi = 0$ and was equal Δ for the angle $\phi = \phi_{\max}$. The two other coordinates of conus points stay the same (Fig. 2.2). This transformation is not isometrical.

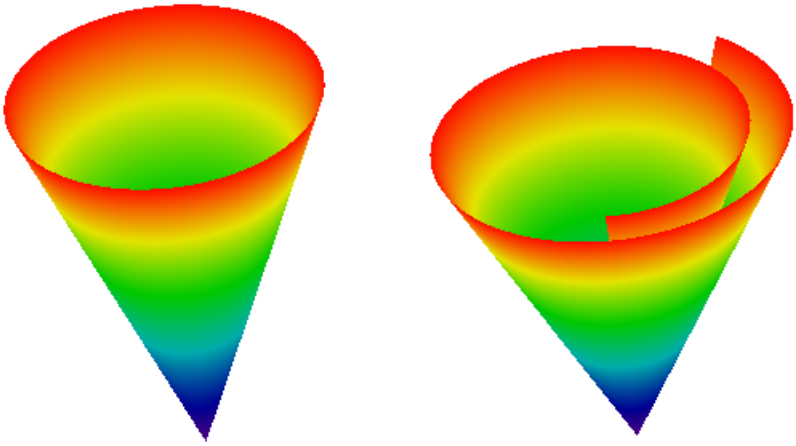

Figure 2.2: *There are a cone on the left and a pseudocone on the right.*

Parametric equation of the new, "'pseudoconical"' surface is

$$\phi(\mathrm{P}, \Phi) = \Phi \cdot \frac{\phi_{\max}}{\pi}, \tag{2.5}$$

$$z(\mathrm{P},\Phi) = \mathrm{P}\cdot\sqrt{1-\left(\frac{\pi}{\phi_{\max}}\right)^2}, \tag{2.6}$$

$$\rho(\mathrm{P},\Phi) = \mathrm{P}\cdot\frac{\pi}{\phi_{\max}}\left(1+\frac{\Delta\phi(\mathrm{P},\Phi)}{\pi K}\right) = \mathrm{P}\cdot\left(\frac{\pi}{\phi_{\max}}+\frac{\Delta\Phi}{\pi K}\right). \tag{2.7}$$

Its explicit equation has the form

$$z(\rho,\phi) = \sqrt{\left(\frac{\phi_{\max}}{\pi}\right)^2-1}\cdot\rho\cdot\left(1+\frac{\Delta\phi}{\pi K}\right)^{-1}. \tag{2.8}$$

Wrapping the semicircle to a cone

In ([105] Figure 3 (b-c)), one can see a wrapping of the semicircle to a surface. We propose the following analytical description of the procedure.

Let us imagine that the semicircle is made of paper. We can wrap this semicircle to a right circular cone (maybe partial or with an overlap) so that the cone vertex corresponds to the semicircle centre (figure 2.3). Let us denote an angle along the cone arc as *cone twist angle* $\phi_{\max}$. We get a cone that becomes closed, if $\phi_{\max} = 2\pi$. We are going to consider only the case where $\phi_{\max} > \pi$. The cone is specified in a cylindrical coordinate system $(\rho,\ \phi,\ z)$ as follows.

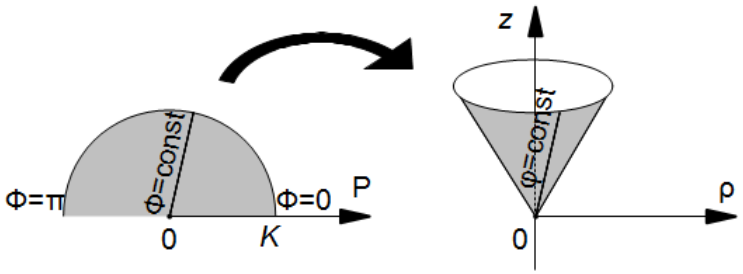

Figure 2.3: *Wrapping of the semicircle to a conic surface.*

First note that curves described by

$$\Phi = \text{const}$$

do not bend during wrapping. Therefore, these curves $\Phi = \text{const}$ are the generatrices of the cone. The parametric equations of the cone are

$$\rho(\mathrm{P}, \Phi) = \mathrm{P} \cdot \frac{\pi}{\phi_{\max}}, \tag{2.9}$$

$$\phi(\mathrm{P}, \Phi) = \Phi \cdot \frac{\phi_{\max}}{\pi}, \tag{2.10}$$

$$z(\mathrm{P}, \Phi) = \mathrm{P}\sqrt{1 - \left(\frac{\pi}{\phi_{\max}}\right)^2}. \tag{2.11}$$

An explicit equation for the object is

$$z(\rho, \phi) = \rho \cdot \sqrt{\left(\frac{\phi_{\max}}{\pi}\right)^2 - 1}. \tag{2.12}$$

Let us note that the semicircumference, limiting the given semicircle, transforms to the cone planar arc, and the centre of the circle becomes the cone's apex.

In order to model not only muscular layers, but also myofibres, one has to look for the position of the transformed chords after the wrapping.

Let us find the chord $Y = \text{const}$ images on the conical surface, by substituting (2.4) into (2.9), (2.10), (2.11):

$$\rho(\Phi) = \frac{Y}{\sin\Phi} \cdot \frac{\pi}{\phi_{\max}}, \tag{2.13}$$

$$\phi(\Phi) = \Phi \cdot \frac{\phi_{\max}}{\pi}, \tag{2.14}$$

$$z(\Phi) = \frac{Y}{\sin\Phi} \cdot \sqrt{1 - \left(\frac{\pi}{\phi_{\max}}\right)^2}. \tag{2.15}$$

The results can be seen in Figure 2.4. It is not difficult to see that rotation of such a simple conical surface around the vertical axis does not give a good representation of the heart anatomy, as it will produce only a conical surface, i.e. a body of zero thickness. To improve that, we will generalize the procedure by introducing dependency of the generatrices on the rotation angle.

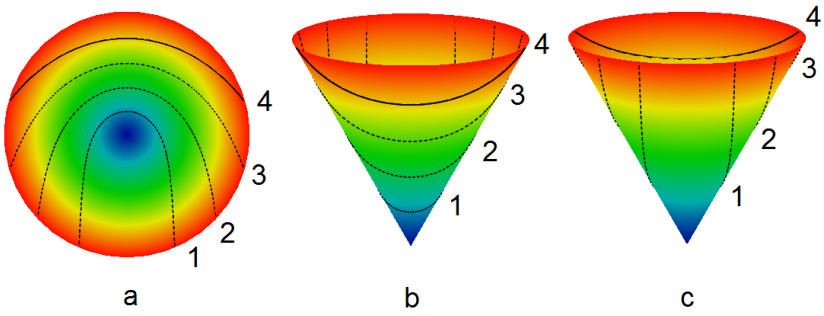

Figure 2.4: *A conical surface with wrapping angle of* $\mathbf{2}\pi$ *and a series of chord images. Bottom view (a); viewing from the top at an oblique angle from two different directions (b and c). Colour represents height, and the chord images are drawn in black. The numbering and line styles of the chord images and of the chords here and in fig. 2.1 are the same.*

Construction of spiral surfaces

In figure 2.3, the cone's generatrix was $z = k\rho$, where k was a constant (see (2.12)), so that it did not depend on the angle ϕ. Let us consider the more general situation when $z = \mathcal{Z}_\phi(\rho)$. Such a generatrix will generate a spiral surface, which will finally give us a proper representation of the heart's geometry.

Let us consider a few examples.

We can first assume that generatrix changes its slope as shown in figure 2.5. It can be formally represented as

$$\mathcal{Z}_\phi(\rho) = \frac{d}{r + \gamma l} \cdot \rho, \tag{2.16}$$

where d, r, l are positive constants, and

$$\gamma = \frac{\phi}{\phi_{\max}}, \tag{2.17}$$

with $0 \leq \gamma \leq 1$. The domain of $\mathcal{Z}_\phi$ is taken

$$D(\mathcal{Z}_\phi) = [0, r + \gamma l]\,,$$

such that the codomain is

$$E(\mathcal{Z}_\phi) = [0, d].$$

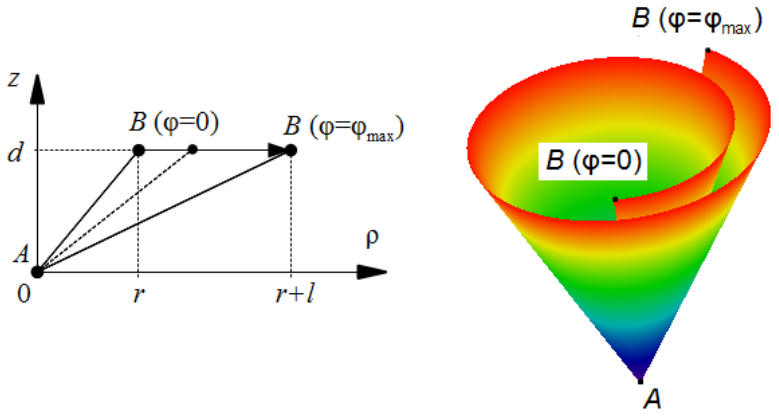

Figure 2.5: *On the left: The construction of the generatrices for a spiral surface, corresponding to the conical LV with a dot vertex. The graph of the function $\mathcal{Z}_\phi(\rho)$ (see (2.16)) connects the points A and B for $\phi = 0$ and $\phi = \phi_{\max}$ by the line segments. On the right: The resulting pseudoconus.*

The conical shape produced by such generatrices is shown in figure 2.5, on the right. We will call it *a pseudoconical surface*.

If we rotate a pseudoconical surface around the vertical axis, we get a conical body that has some resemblance to the LV (it has an LV cavity), but its thickness at the apex will be zero. To improve, we modify the generatrices as follows.

Let us move the end A (see figure 2.5) down by a value $h\gamma$, i.e. proportional to the angle $\phi = \gamma\phi_{\max}$ (h is a positive constant), as shown in figure 2.6:

$$\mathcal{Z}_\phi(\rho) = \frac{d + h\gamma}{r + \gamma l} \cdot \rho + h - h\gamma, \tag{2.18}$$

$$D(\mathcal{Z}_\phi) = [0, r + \gamma l]\,, \quad E(\mathcal{Z}_\phi) = [h - h\gamma, d + h]\,.$$

As a result, the thickness of the LV at the apex will become $h > 0$, which improves our representation. However, a real LV surface is not conical, so we have to use curves as generatrices instead of straight line segments.

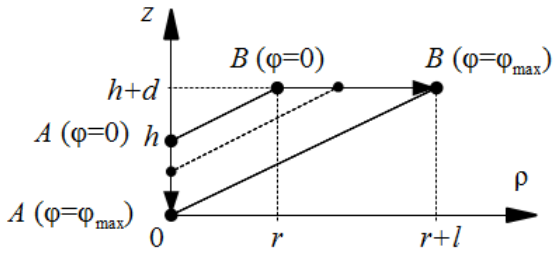

Figure 2.6: *The construction of the generating lines for a spiral surface corresponding to the conical LV with a thick vertex. The graph of the function $\mathcal{Z}_\phi(\rho)$ (see (2.18)) connects the points A and B for $\phi = 0$ and $\phi = \phi_{\max}$ by the line segments.*

Let us connect the same points A and B, as in the previous example, but by an arc (figure 2.7):

$$\mathcal{Z}_\phi(\rho) = (d + h\gamma) \cdot \mathcal{F}_\phi \left(\frac{\rho}{r + \gamma l} \right) + h - h\gamma, \tag{2.19}$$

where the function $\mathcal{F}_\phi$ represents a curved generatrix.

$$D(\mathcal{F}_\phi) = E(\mathcal{F}_\phi) = [0, 1];$$

$$D(\mathcal{Z}_\phi) = [0, r + \gamma l], \quad E(\mathcal{Z}_\phi) = [h - h\gamma, d + h].$$

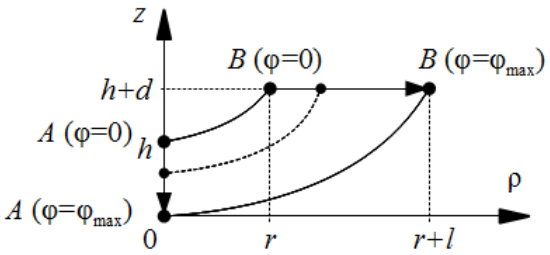

Figure 2.7: *The construction of the generatrices for the salient spiral surface used in modelling the convex LV with a thick vertex. The graph of the function $\mathcal{Z}_\phi(\rho)$ (see (2.19)) connects the points A and B for $\phi = 0$ and $\phi = \phi_{\max}$ by the arcs of curves.*

The following properties are imposed on the function $\mathcal{F}_\phi(\rho)$

1. $D(\mathcal{F}_\phi(\rho)) = E(\mathcal{F}_\phi(\rho)) = [0,1]$

2. $\mathcal{F}_\phi(\rho)$ is continuous and differentiable on $[0,1]$

3. $\mathcal{F}_\phi(\rho)$ increases monotonically on $[0,1]$.

We refer to the functions with these properties as *generating functions* (GF). In the first example $\mathcal{F}_\phi(t) = t, \quad \mathcal{Z}_\phi(\rho) = \mathcal{F}_\phi\left(\frac{\rho}{r+\gamma l}\right) \cdot (d+h)$; in the second example $\mathcal{F}_\phi(t) = t$, and $\mathcal{Z}$ is represented through $\mathcal{F}$ in the same way as in the third example (see (2.19)). Now let us choose a proper GF to construct a more realistic LV.

A model of the LV

To represent the shape of the epicardial LV surface, Streeter [105, pp. 91–92] used the following functions:

$$\rho_{\text{epi}}(\psi) = (r+l)\left(\varepsilon\cos\psi + (1-\varepsilon)(1-\sin\psi)\right); \tag{2.20}$$

$$z_{\text{epi}}(\psi) = (d+h)(1-\sin\psi). \tag{2.21}$$

If $\varepsilon = 0$, the curve AB is a line segment, and if $\varepsilon = 1$, it is a quarter of an ellipse. For intermediate ε values, we get intermediate curves.

For brevity of formulae writing, below we will use the following signs:

$$\varepsilon_c = \varepsilon\cos\psi + (1-\varepsilon)(1-\sin\psi),$$

$$\varepsilon_s = \varepsilon\sin\psi + (1-\varepsilon)\cos\psi.$$

Let us use the following equation of the endocardium in analogy with Streeter's description:

$$\rho_{\text{endo}}(\psi) = r\varepsilon_c; \tag{2.22}$$

$$z_{\text{endo}}(\psi) = d(1-\sin\psi) + h, \tag{2.23}$$

where "latitude" ψ takes values $0^\circ \le \psi \le 90^\circ$ (figure 2.8). Parameters determining the shape are: an inner radius r near the equator; a thickness l near the equator; a thickness h at the apex; a height $H = d + h$.

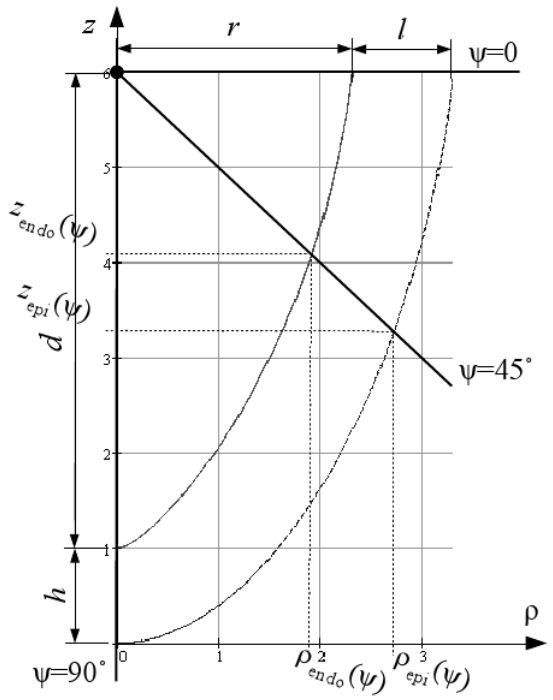

Figure 2.8: *A shape of function representing the endocardial (the solid line, see (2.20), (2.21)) and epicardial (the dashed line, see (2.22), (2.23)) surfaces.*

The form of any intermediate layer between epi- and endocardium is described by the equations:

$$\rho_{\mathrm{mid}}(\psi,\gamma) = (r+\gamma l)\cdot\varepsilon_c, \tag{2.24}$$

$$z_{\mathrm{mid}}(\psi,\gamma) = (d+\gamma h)(1-\sin\psi) + (1-\gamma)h.$$

As a result, after elimination of ψ, we get the following definition of the ε-spiral surface (ESS):

$$z_{\varepsilon\mathrm{sp}}(\rho,\phi) = (d+\gamma h)\mathcal{F}_{\varepsilon\mathrm{sp}}\left(\frac{\rho}{r+\gamma l}\right) + (1-\gamma)h, \tag{2.25}$$

$$\mathcal{F}_{\varepsilon\mathrm{sp}}(t) = \frac{\varepsilon^2 + t(1-\varepsilon) - \varepsilon\sqrt{2t(1-\varepsilon)+\varepsilon^2-t^2}}{(1-\varepsilon)^2+\varepsilon^2}, \tag{2.26}$$

where $\mathcal{F}_{\varepsilon\mathrm{sp}} : [0,1] \to [0,1]$ is the GF of the epicardium, the endocardium and every intermediate layer of the LV wall; $\rho/(r+\gamma l) \in [0,1]$. The spiral surface's border with an angle $\phi = 0$ is located at the endocardial side, and the border with an angle $\phi = \phi_{\max}$ lies at the epicardial side. The LV model is made as a body of revolution of an ESS. See figure 2.10 for an example of a single and multiple nested ESS. We form the LV by using shifted layers (or the rotated spiral surfaces, which is the same) because a thick muscular layer cannot be wrapped to a body of revolution with overlapping, but without any shift of its sheets.

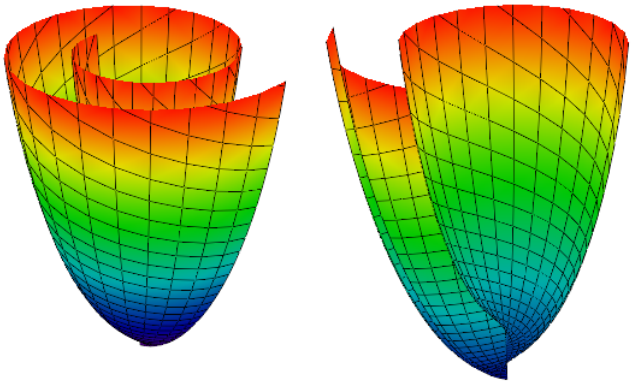

Figure 2.9: *A spiral surface. The lines on it have equations $\rho = const$ and $\phi = const$. Color corresponds height (z coordinate)*

Our description reproduces the form of epicardium from Streeter's work (see figure 40 in [105]), but for endocardium, Streeter uses more complex equations with an additional parameter that he called the 'angle of taper'. However, we found that even without this parameter our function reasonably reproduces the form of the endocardium, and, thus, we decided to use equation (2.25) without further modifications.

In further calculations, we will use the special CS (γ, ψ, ϕ) linked with the spiral surfaces. In this CS, the variable $\gamma \in [0,1]$ describes point position in the LV wall thickness, $\gamma = 0$ corresponds to the endocardium, $\gamma = 1$ corresponds to the epicardium; $\psi \in [0, \pi/2]$ is an analogue of the geographical latitude, $\psi = 0$ is

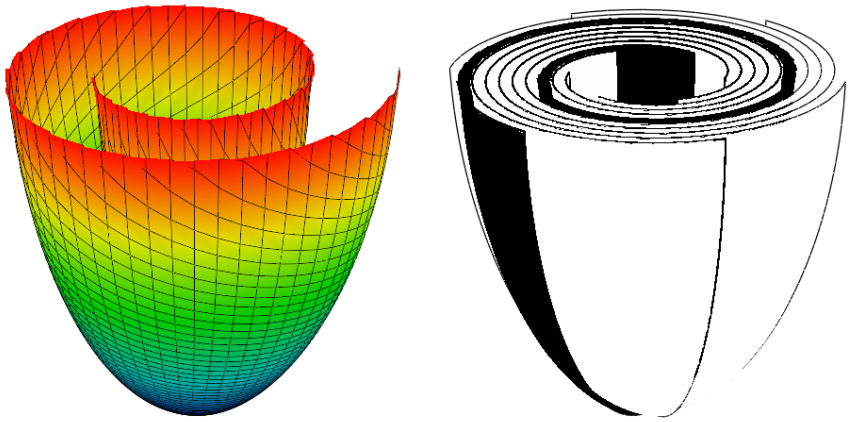

Figure 2.10: *A spiral surface (on the left, the lines have equations $\rho = const$ and $\phi = const$), a schematic representation of the LV obtained (six spiral surfaces rotated by angles 0°, 60°, 120°, 180°, 240° and 300° around the vertical axis (on the right, compare with [105, fig. 3D])). If we consider infinitely many such surfaces, we obtain the whole LV model.*

the upper plain part of the model LV (the equator or zone of the valves and fibrous ring), $\psi = \pi/2$ is the apex; $\phi \in [0, 2\pi]$ is analogue of the geographical longitude. Formulae of transition from the special CS to the cylindrical CS (ρ, ϕ, z) have the following form:

$$\rho = (r + \gamma l)\, \varepsilon_c, \tag{2.27}$$

$$z = (d + \gamma h)\,(1 - \sin\psi) + (1 - \gamma)h. \tag{2.28}$$

In the problem we consider, the coordinates lie in the following limits:

$$0 \le z \le d + h; \quad 0 \le \rho \le r + l.$$

Together with the LV base equation $z = d + h$, the formulae (2.27)–(2.28) let one get an LV surface model without fibres.

An important advantage of the special CS is that equations of the epicardium, endocardium, and equator are written there in a very simple form.

Epicardium equation in the special CS is

$$\gamma = \gamma_1, \tag{2.29}$$

in the cylindrical coordinates:

$$\rho = (r + \gamma_1 l)\varepsilon_c, \tag{2.30}$$

$$z = d + h - (d + \gamma_1 h)\sin\psi. \tag{2.31}$$

Endocardium equation in the special CS is

$$\gamma = \gamma_0, \tag{2.32}$$

in the cylindrical coordinates:

$$\rho = (r + \gamma_0 l)\varepsilon_c, \tag{2.33}$$

$$z = d + h - (d + \gamma_0 h)\sin\psi. \tag{2.34}$$

Equator equation in the special CS is

$$\psi = 0, \tag{2.35}$$

in the cylindrical coordinates:

$$\rho = r + \gamma l, \tag{2.36}$$

$$z = d + h. \tag{2.37}$$

Spiral surfaces

Myocardial layers are modelled as surfaces filling the LV by rotation of one surface about (vertical) LV symmetry axis. A common view of an SS is shown in Fig. 2.9.

Parametric equation of spiral surface in the cylindrical CS has the form

$$\begin{aligned}
\rho(\gamma,\psi) &= (r + \gamma l)\,\varepsilon_c, \\
\phi(\gamma,\psi) &= \phi_0 + \phi_{\max}\gamma, \\
z(\gamma,\psi) &= (d + \gamma h)\,(1 - \sin\psi) + (1 - \gamma)h,
\end{aligned}$$

where $\phi_{\max}$ is dimensionless parameter affecting fibre rotation about the LV axis.

Finally, the ε-spiral surface (ESS) definition is

$$z_{\mathrm{sp1}}(\rho,\phi) = (d + \gamma h)\mathcal{F}_{\varepsilon sp}\left(\frac{\rho}{r + \gamma l}\right) + h - \gamma h, \tag{2.38}$$

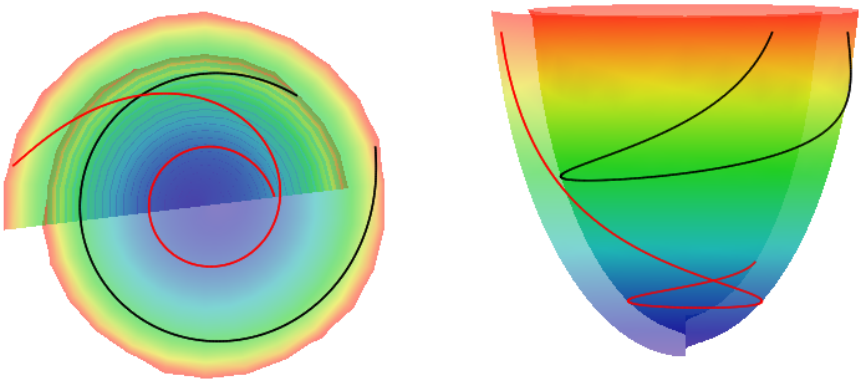

Figure 2.11: *A spiral surface and two fibers on it. On the left, bottom view; on the right, top view.*

$$\gamma = \frac{\phi - \phi_0}{\phi_{\max}}. \tag{2.39}$$

The border of ESS with the angle $\phi = \phi_0$ corresponds to the endocardium, and with the angle $\phi = \phi_0 + \phi_{\max}$ corresponds to the epicardium.

The myofibers' equations and fibre direction

The equations are (compare with (2.13) and (2.15))

$$\rho(\Phi) = \frac{Y}{\sin\Phi} \cdot \left(r + l\frac{\Phi}{\pi} \right), \tag{2.40}$$

$$\phi(\Phi) = \phi_{\max}\Phi/\pi, \tag{2.41}$$

$$z(\Phi) = z_{ess}(\rho(\Phi), \phi(\Phi)), \tag{2.42}$$

where different values of the parameter $Y \in (0, 1)$ correspond to different myofibers,

$$\Phi \in [\arcsin Y, \pi - \arcsin Y],$$

$z_{ess}(\rho, \phi)$ is the explicit equation of a spiral surface in the cylindrical CS.

See Fig. 2.11 for an example of a spiral surface and the fibers on its surface.

At each point (γ, ψ, ϕ), $0 \leq \psi < \pi/2$, a fiber orientation vector $\mathbf{v} = (x', y', z')$ is given by formulae:

$$x' = \frac{d\rho}{d\Phi}\cos\phi - \rho\sin\phi\frac{d\phi}{d\Phi}, \tag{2.43}$$

$$y' = -\left(\frac{d\rho}{d\Phi}\sin\phi + \rho\cos\phi\frac{d\phi}{d\Phi}\right), \tag{2.44}$$

$$z' = \frac{\partial z}{\partial \rho}\cdot\frac{d\rho}{d\Phi} + \frac{\partial z}{\partial \phi}\cdot\frac{d\phi}{d\Phi}, \tag{2.45}$$

where ρ is found from Eq. (2.27),

$$\Phi = \pi(1-\gamma),$$

$$\frac{d\rho}{d\Phi} = \varepsilon_c \cdot \left((r_b + \gamma l)\cot(\gamma\pi) - \frac{l}{\pi}\right),$$

$$\frac{d\phi}{d\Phi} = \frac{\phi_{\max}}{\pi},$$

$$\mathcal{F}' = \frac{\cos\psi}{\varepsilon_s},$$

$$\frac{\partial z}{\partial \rho} = \frac{d+\gamma h}{r+\gamma l}\cdot\mathcal{F}',$$

$$\frac{\partial z}{\partial \phi} = \frac{1}{\phi_{\max}}\cdot\left(h\sin\psi + \frac{\mathcal{F}'\varepsilon_c l(d+\gamma h)}{r+\gamma l}\right),$$

$\phi_{\max}$ is a dimensionless parameter affecting fiber twist.

Overall, we can consider the anatomical model as a map from a rectangular domain $\gamma_0 \leq \gamma \leq \gamma_1$; $0 \leq \psi < \pi/2$; $0 \leq \phi < 2\pi$ to the shape of LV with anisotropy explicitly given by Eqs. (2.43)–(2.45).

Fibre angles

To represent fibre orientation and to compare it with anatomical data, Streeter [105] used the following angles: true fibre angle, α; the helix angle, α_1; and the longitudinal angle, α_2 (see figure 2.12 for their definitions). We follow the same approach in this work.

Together with (2.26), (2.25) forms the basis for the LV model. Finally, we need to set proper fibre angles at the epicardial and endocardial surfaces.

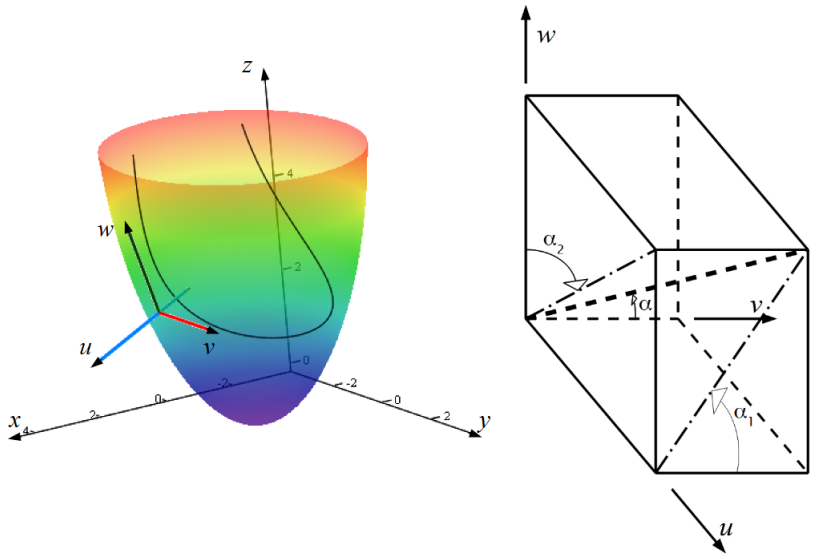

Figure 2.12: *On the left, definition of the local coordinate system. $Oxyz$ is the global Cartesian coordinate system. The blue axis is normal u to the epicardium; the red axis, latitude v; the dark green axis, longitude w. The colourful surface is the epicardium; the colour depends on altitude z. The curve inside is a fibre as a chord image, the curve does not lie on the epicardium. The normal axis intersects the curve at a point. On the right, definition of the true fibre angle, α; the helix angle, α_1; and the longitudinal angle, α_2. The thick, dashed line is a tangent to a myofibre segment constructed at the origin of the coordinates. The dashed-and-dotted lines are projections of the myofibre tangent.*

In the model given by (2.26) and (2.25), angle α depends on point position in the LV wall and changes from $90°$ on the endocardium to approximately $0°$ in the middle of the wall and then to $90°$ on the epicardium. In real hearts, the rotation of fibre is less, and its values at the endocardium and epicardium are about $60°$ and $70°$ ([105] figure 33). To account for that, we apply A. Panfilov's suggestion of using only part of the interval $0 \le \gamma_0 \le \gamma \le \gamma_1 \le 1$. For example, if $\gamma_0 = 0.1 \le \gamma \le 0.75 = \gamma_1$, then the extreme angle values in the equatorial area are $55°$ at

the endocardium and 75° at the epicardium (see figure 2.13 and Results for more details).

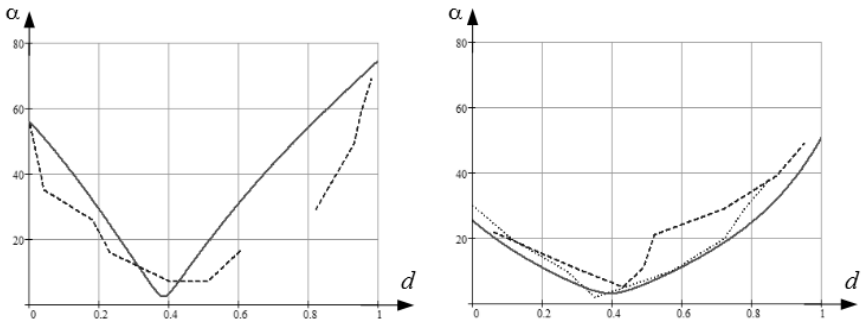

Figure 2.13: *The true fibre angle, α, (in degrees) in the equatorial and bottom areas of the LV. The solid lines correspond to the data from our model, the dashed and dotted ones correspond to the experimental data from [105]. The horizontal axis from endo- (value 0) to epicardium (value 1). The trabecular LV zone is not taken into account.*

As a change in the range of γ changes the anatomy of the heart, we need to rescale it to the normal heart using:

$$r = r^i + \frac{l^i \gamma_0}{\gamma_1 - \gamma_0},$$

$$l = \frac{l^i}{\gamma_1 - \gamma_0},$$

$$d = d^i + \frac{h^i \gamma_0}{\gamma_1 - \gamma_0},$$

$$h = \frac{h^i}{\gamma_1 - \gamma_0},$$

$$\phi_{\max} = \frac{\phi^i_{\max}}{\gamma_1 - \gamma_0}.$$

Here, the index "i" denotes input parameters.

After choosing of γ_0 and γ_1, we completely specify parameters of our model and can use it for generation of anisotropy.

2.3 Geodesic principle for local myofiber direction

As stated above, the following proposition lies in the background of the morphological model we suggested in this work: the transformation of the semicircular planar layer to the spiral surface transfers any fiber initially aligned with a chord of the semicircle to that aligned exactly with the transformational image of this chord. At the same time we checked a hypothesis formulated by Streeter [105] that the muscle fibers should locate along with geodesic lines on the surfaces forming muscle layers of the ventricle wall. Specifically, we found out whether the chord-fiber of the semicircle might shift during the transformation of the latter to the spiral surface and finally adopt a position of geodesic line connecting the images of the chord on the spiral surface. Moreover, this geodesic line has to lie quite near the initial chord image. This should be so, unlike abstract lines the fibers have nonzero thickness, and in aggregate they fill the ventricle wall quite tightly. Therefore, when folding a plane muscular layer into the spiral surface, the chord-fibers materially can't shift significantly relative to the places of the initial chords' convolution images.

Unlike this, the following turned out to be in the model. At the first transformation step (the folding of the semicircle into the cone) chords' images as such remain geodesic lines; in other words, the shift of the geodesic line relative to the chord image is zero at this step. However, at the second step, i.e. after the transformation of the conic surfaces to the curvilinear spiral one, the pattern drastically changed: all geodesic lines connecting endocardiac and epicardiac points of the layer with each other went almost vertically to the apex area, so that all the loops of the chord images (regardless of the chord image position on the spiral surface) degenerate into rather small ones localized closely around the apex (fig. 2.14). As a result, chord images located in the central (relative to the ventricle height) segment of the body of revolution are not represented by the respective geodesic lines, i.e. this segment remains empty of such geodesic lines at all. This means that such geodesic lines are not appropriate to represent the fibers. In other words, the

"geodesic model" of the fiber disposition is incorrect at least for the chosen type of spiral surfaces.

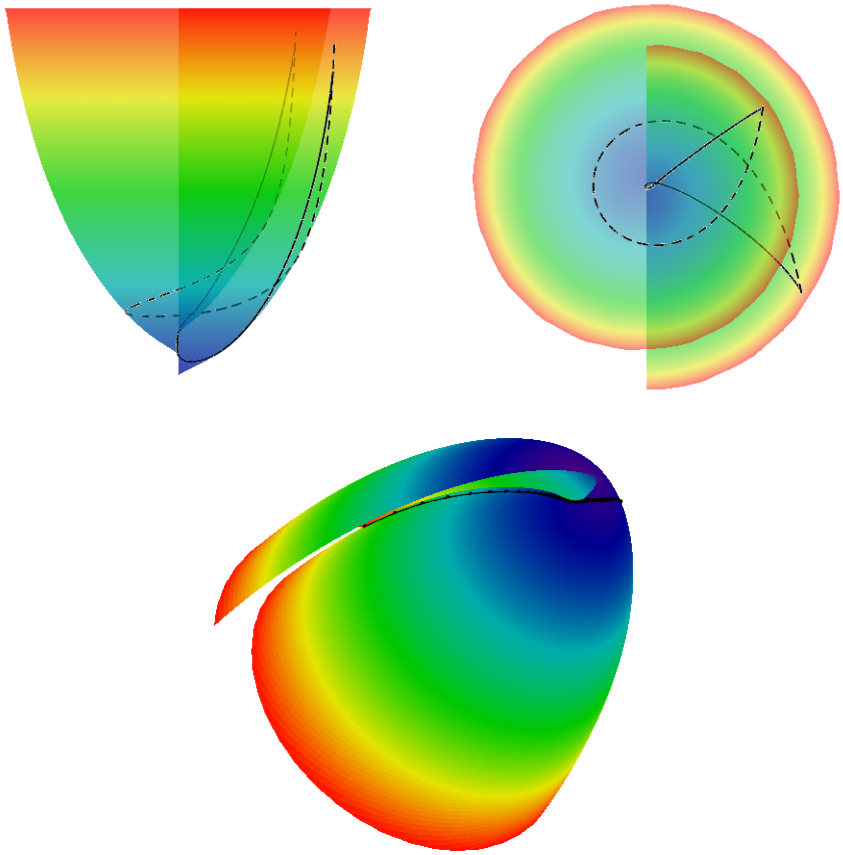

Figure 2.14: *A geodesic line (solid line) and a chord image (dashed line) connecting 2 points. The edge points are situated at the subepi- and subendocardial surfaces near the equator on ESS with torsion angle of* 3π.

Nevertheless, this consideration should not make reject eventually the idea of geodesic arrangement of the muscle fibers in the ventricle. We intend to continue searching a type of spiral surfaces where the geodesic principle might be applicable for the placement of the fibers. It is also possible that another principle of optimization distinct from purely geometric one should be involved in. For instance,

it seems reasonable to look for an appropriate mechano-geometric functional to be optimized. This may be something like the method suggested in the cited above works [8, 16], but should be associated with the spiral surfaces representing myocardial layers.

In the case that the spiral surface has small torsion angle ($< 1.5\pi$), geodesic line, which connects the images of the ends of the chord, does not have a considerable shift in the direction of the vertex. The images of the ends of the chords do not have such shift. However, this case is not of great interest, because in the case, when torsion angle is less than 1.5π, there are neither images of the chords, nor geodesic lines forming a loop with turn of 360° or more.

2.4 Comparison of the theoretical model with experimental data

In this section, we indicate the parameter values used in our study and compare theoretically obtained results with experimental data from [105] and [65].

Verification of the model: comparison with Streeter's data

We used the following parameter values reported in ([105] table 2): external radius of LV at the equator $r^i + l^i = 33$ mm, thickness of LV wall at the equator $l^i = 10$ mm, height of under-equatorial LV part $d^i + h^i = 60$ mm, thickness of LV wall at the apex $h^i = 7$ mm, $\varepsilon = 0.9$; and we set angle of spiral surface torsion $\phi^i_{\max} = 3\pi$ according to ([105] figure 3c).

See Figure 2.15 for the spiral surfaces we made using these parameter values.

We used the parameters of the subepicardial and subendocardial boundaries $\gamma_0 = 0.1$, and $\gamma_1 = 0.75$, which gives $\alpha = 55^\circ$ at the endocardium and $\theta = 75^\circ$ at the epicardium that fits with ([105] figure 44) taking into account the experimental measurement error and data variability.

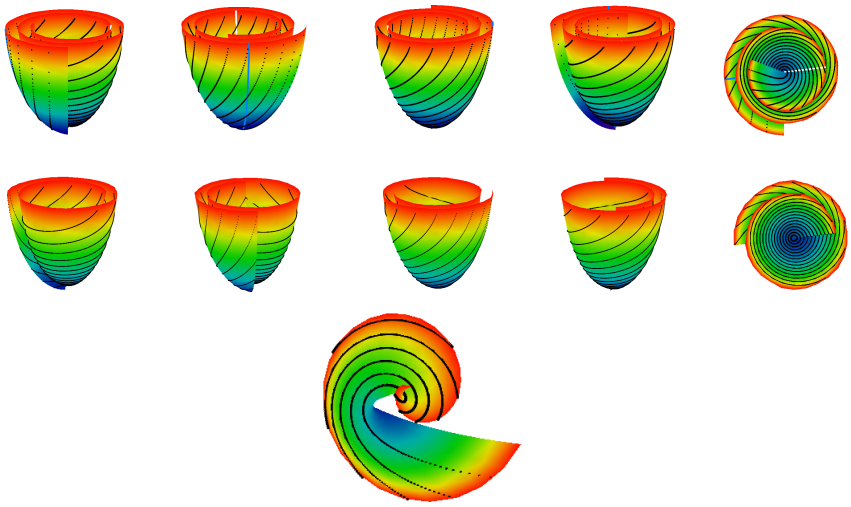

Figure 2.15: *ESS used in the model of convex LV with a thick equator and* γ *restricted to* $[\gamma_0, \gamma_1] = [0.1, 0.75]$ *and chord images (black lines). The first row: four side and one top views, full model with* $\gamma \in [0, 1]$*. The second row: the same, after the* γ *limitation. The bottom figure: area of the apex* $(0 \leq z \leq h)$*, top view.*

We compared three angular characteristics of our myofibres field with experimental data from [105]. The comparison was made in two areas of the LV: the equatorial (58 mm$\leq$ z $\leq$60 mm) and the bottom (18 mm$\leq$ z $\leq$21 mm) parts of the LV. In both regions, angles were compared along a line orthogonal to the epicardium, which is common in anatomical studies.

The results of comparison are shown in figures 2.13, 2.16 and 2.17.

LV top zone

Note that in the LV top zone, the true fibre angle α varies non-monotonically, as in Streeter's data [105]. In particular, α on the endocardium was close to 55°, on the epicardium it was close to 75° and decreased to 5° approximately at the middle of the LV wall, between 35% and 40% of the wall depth (figure 2.13, on the left).

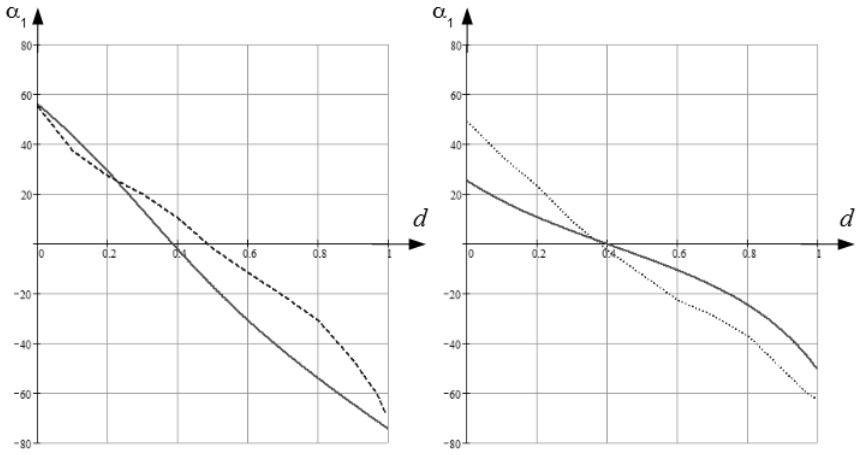

Figure 2.16: *The helix angle, α_1. The axes are the same as in fig. 2.13.*

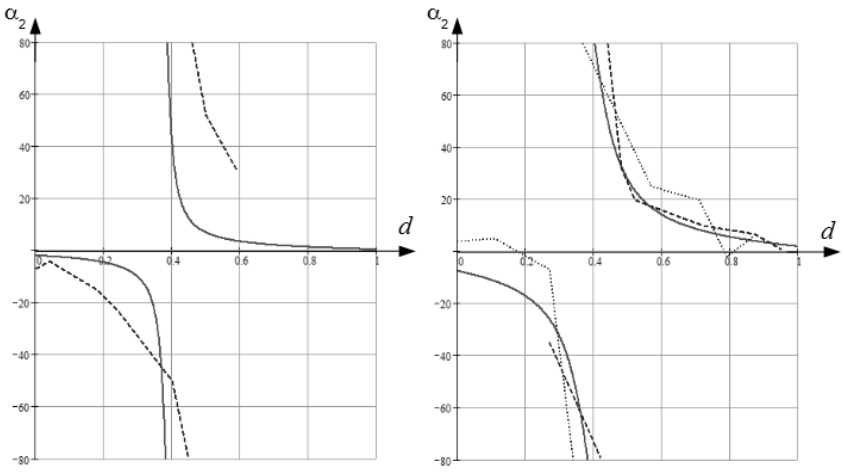

Figure 2.17: *The longitudinal angle, α_2. The axes are the same as in fig. 2.13.*

We see some differences in the slope of curves in our model and in measured data; however, a qualitative correspondence is observed.

Figure 2.16, on the left, shows similar results for the helix angle. We see that going from endocardium to epicardium, the helix angle α_1 decreased monotonically from $+55^\circ$ to -75° and was equal to 0° approximately at the middle of the LV wall, between 35% and 40% of the wall depth. We also see a good agreement of our model with the experimental results from [105].

As we see in figure 2.17, on the left, the longitudinal angle, α_2, going from endocardium to the middle of the LV wall, decreased from 0° to -90°. At the middle of the LV wall, between 35% and 40% of the wall depth, the experimental and modelled angle abruptly changed from -90 to $+90^\circ$, which is an artefact. We found the jump at 43%, while it was 38% in Streeter's data. At the exterior half of the LV wall, the α_2 angle decreased at a decelerating rate to 0°. Here too, we observe good qualitative correspondence of our model with experimental data, although some quantitative differences in the slopes of the dependencies are present.

LV middle zone

The true fibre angle α also reaches a minimum in the mid-wall region, both in our model and in Streeter's data. On the endocardium, it was close to 35°, on the epicardium, it was close to 50° and decreased to 5° approximately at the middle of the LV wall, at 0.4 of the wall depth (figure 2.13, on the right).

Figure 2.16, on the right, displays similar results for the helix angle. We see that going from endocardium to epicardium, the helix angle, α_1, decreased monotonically from $+25^\circ$ to -50° and was equal to 0° approximately at the middle of the LV wall, at 0.4 of the wall depth. We also see a good agreement of our model with the experimental results from [105].

In figure 2.17, on the right, the longitudinal angle, α_2, decreased from -5° to -90° between endocardium and mid-wall. At the middle of the LV wall, between 0.35 and 0.4 of the wall depth, the angle again abruptly changed to $+90^\circ$. On the exterior half of the LV wall, the α_2 angle decreased at a decelerating rate to

$0°$. A good qualitative correspondence with anatomical data is found in the outer two-thirds of the LV wall.

Our model also successfully reproduces the distribution of fibre directions in the thick, radially placed layer of the LV wall, as shown in figure 2.18. Streeter studied the pattern and named it 'Japanese fan' [105, fig. 42c].

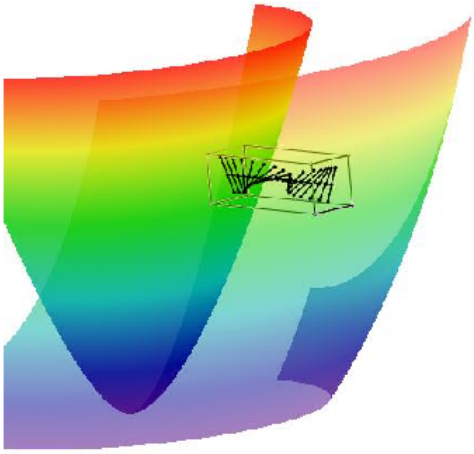

Figure 2.18: *Fibre slope angle variation depending on fibre's position in the thickness of the wall in the LV model. Endo- and epicardial wall surfaces are highlighted. Colour of the border surfaces from the equator to the vertex matches rainbow colours*

Overall we can claim that our model adequately reproduces the direction of myocardial fibres in the human LV.

Comparison with Auckland canine dataset

We also compared our model to the data used in [65]. The comparison was conducted in the following way. We aligned our LV model with the Auckland model along the vertical axis and found that reasonable fit of our anatomy to the Auckland heart model occurs for: $r^i + l^i = 45$ mm, $d^i + h^i = 80$ mm, $h^i = 12$ mm, $l^i = 15$ mm, $\varepsilon = 0.85$, $\phi^i_{\max} = 3\pi$, $\gamma_0 = 0.15$, $\gamma_1 = 0.9$. Subsequently we constructed five meridional half-planes so that they divided the LV free wall region

and the dihedral angle to four equal dihedral angles. We examined only points lying near the five half-planes. We used the same comparison procedure that we described in Section "Verification of the model: comparison with Streeter's data". The fibre orientation was compared at three different "latitudes" (close to apex, in the middle and close to base) along lines orthogonal to the heart surface. We computed the x values (they show the position of a point in the ventricular wall) and the two angles, α and α_1, and plotted their values from the experimental dataset and from the theoretical model. The results obtained are shown in figure 2.19.

We see that the plots of the α angle have characteristic V-shaped forms, both in the model and in four of five meridional sections at all three "latitudes". The model angle is within the limits of the section angles in almost all the positions, except the external one-third of the wall on the left graph. The plots of the α_1 angle show the same pattern: they descend from some positive values to some negative ones, speed of the decrease is higher in the endo- and epicardial area and slightly less in the mid-myocardium.

Note that we show only one line for our model. This is because our model is rotationally symmetric, and all five lines for different rotation angles are the same. The model is an idealization and it represents only some averaged characteristics of LV and neglects possible individual aspects of the LV form.

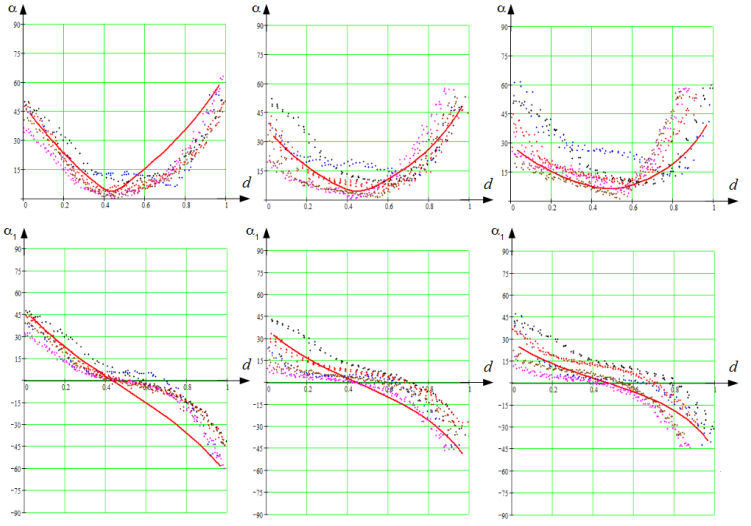

Figure 2.19: *The true fibre angle, α, (the first row) and the helix angle, α_1, (the second row) in the canine LV free wall. The solid, red lines correspond to the data from our model, and the dots correspond to the Auckland canine anatomy data from [65]. The left graphs show the upper area of the LV ($\psi = 30°$ at the epicardium); the centre graphs, the middle area ($\psi = 45°$); and the right graphs, the bottom area ($\psi = 60°$). The abscissa axis reflects the position of a point in the thick layer of the LV wall, 0 corresponds to the endocardium (the trabecular LV zone is not taken into account), 1 corresponds to the epicardium. The colour of the points corresponds to the five different longitudes (ϕ) at the LV free wall.*

2.5 Discussion

In this section, we discuss limitations of our model, experimental methods and models that can be used to verify it, its possible applications and ways of improving it.

In our approach to the modelling of the LV architecture, anisotropy of the heart was derived from some general principles. In our model, the LV is considered as a set of identical spiral surfaces combined with each other by rotation about the vertical axis. The every spiral surface is defined analytically and represents a mapping of half disc. The first step of the transformation is the mapping of the semicircle to a conical surface. In the second step, the conical surface is transformed to a curved spiral surface, representing the quasi-elliptical shape of the LV boundary surface. Finally, every spiral surface is filled with myocardium fibers represented by the transformed images of the chords which were parallel to the diameter in the initial semicircle (see fig. 2.1).

The developed formalism is closely associated with anatomic observations presented by Streeter in his classical work [105]. Moreover, we used experimental data from the same work as well as from [65] for the model verification. In particular, the model proved to reproduce adequately both the looping arrangement of the muscle fibers (see fig. 2.11) and the specific pattern of the fiber relative positions in the transmural direction through the ventricle wall (fig. 2.18). The special features of the fiber arrangement are of great importance for the concordant mechanical performance of the ventricle.

As stated above, the following proposition lies in the background of the morphological model we suggested in this work: the transformation of the semicircular planar layer to the spiral surface transfers any fiber initially aligned with a chord of the semicircle to that aligned exactly with the transformational image of this chord. At the same time we checked a hypothesis formulated by Streeter (ibidem) that the muscle fibers should locate along with geodesic lines on the surfaces forming muscle layers of the ventricle wall. Specifically, we found out whether the

chord-fiber of the semicircle might shift during the transformation of the latter to the spiral surface and finally adopt a position of geodesic line connecting the images of the chord on the spiral surface. Moreover, this geodesic line has to lie quite near the initial chord image. This should be so, unlike abstract lines the fibers have nonzero thickness, and in aggregate they fill the ventricle wall quite tightly. Therefore, when folding a plane muscular layer into the spiral surface, the chord-fibers materially can't shift significantly relative to the places of the initial chords' convolution images.

Nevertheless, this consideration should not make reject eventually the idea of geodesic arrangement of the muscle fibers in the ventricle. We intend to continue searching a type of spiral surfaces where the geodesic principle might be applicable for the placement of the fibers. It is also possible that another principle of optimization distinct from purely geometric one should be involved in. For instance, it seems reasonable to look for an appropriate mechano-geometric functional to be optimized. This may be something like the method suggested in the cited above works [8, 16], but should be associated with the spiral surfaces representing myocardial layers.

Thus, the model described in this article reproduces sufficiently well the path of the myofibers in LV wall. Moreover, it is based on not sophisticated structures and it is described entirely analitically. The possibility of an analytical calculation of many differential-geometric characteristics of used surfaces and curves appreciably facilitates its analysis. The model may be used for calculation of electrophysiological and mechanical activity of myocardium of the human heart left ventricle.

Our model adequately reproduces fiber angles at the LV middle zone, but agreement for the LV top zone is mainly qualitative.

The analytical representation of geometry presented here can be used for the development of new numerical methods to study the electrical and mechanical activity of the heart. As our model provides an analytical mapping of a rectangle in (γ, ψ, ϕ) space into the heart shape, one can formulate a numerical scheme in (γ, ψ, ϕ) space (where the representation of boundary conditions is the most

natural) and account for anisotropy by explicit analytical formulae. Such mapping can also be used to generate various anisotropic properties of the heart and study their effect on the electrical and mechanical heart function.

Limitations

Our model adequately reproduces fibre angles at the LV middle zone, but agreement for the LV top and apex zones is mainly qualitative.

Inaccurate reproduction of fibre direction in the basal and apical zones can be caused by different reasons, one of which can be the idealized axisymmetrical LV form in the model. Real ventricles have essential deflections from the axis symmetry; they are somewhat individual, that is specific for every LV. In this work, we tried to construct an axisymmetrical model that could maximally suit the middle (by height) LV area. The apex and base of a real LV could considerably move away from the axis. In this thesis, we also propose a more realistic non-axisymmetrical extension of the model which will adapt the idealized model to individual peculiarities of real ventricles. It allows us to achieve more accurate imitation of the transmural run of the fibres at the apical and basal zones.

Development and uses of our model

We suggest that analytical representation of the geometry presented here can be used for development of new numerical methods to study electrical and mechanical activity of the heart. As our model provides analytical mapping of a rectangle in (γ, ψ, ϕ) space into the curvilinear heart shape, one can formulate a rectangular numerical scheme in (γ, ψ, ϕ) space (where representation of boundary conditions is simplest) and account for anisotropy by explicit analytical formulae. The model can also be used to generate various anisotropic properties of the heart and modulations of the LV shape (via model parameter variations) and to study their effects on electrical and mechanical heart functions.

3

Modelling of the left ventricle electrophysiological activity

3.1 Introduction

The results described in this chapter have been published in [89].

The modelling of cardiac electrical function is a well-established area of research that began with early models of cardiac cells developed by D. Noble [66].

The importance of modelling in cardiology comes from the widespread prevalence of cardiac disease. For example, sudden cardiac death is the leading cause of death in the industrialized world, accounting for more than 300,000 victims annu-

ally in the US alone [61]. In most cases, sudden cardiac death is a result of cardiac arrhythmias that occur in the ventricles of the human heart [61].

When studying cardiac arrhythmias, it is important to understand that they often occur at the level of the whole organ and in these situations cannot be reproduced in single cells. Therefore, it is very important to model cardiac arrhythmias at the tissue level, preferably using an anatomically accurate representation of the heart. Compared to modeling at the single-cell level, anatomical modelling started much more recently [75, 77]. Using anatomical models, researchers have been able to obtain important results on the 3-D organization of cardiac arrhythmias in animal [70] and human [118] hearts. Moreover, the defibrillation process has been investigated [95], and the effects of mechano-electrical coupling on cardiac propagation have recently been modelled [48,52]. Multi-scale anatomical cardiac modelling is becoming increasingly prominent in medical and pharmaceutical research [67].

To study the effects of anisotropy on wave propagation, one needs to vary the anisotropic properties and to separate the anisotropy effects from other factors. All these questions can be addressed with the development of models that account for the anisotropy of the heart using analytical or numerical tools.

In the previous section, we described an axisymmetric model of the human heart LV. In the model, we represented the LV shape (including positions of cardiac fibres) as analytical functions of special curvilinear coordinates defined on a rectangular domain. Our model allowed the generation of not only a default architecture of anisotropy closest to the reality but also intermediate architectures that can be used to study the effects of any specific element of anisotropy on wave propagation in the heart.

In this chapter, we build on our previous approach in two ways. First, we develop a numeral scheme for the integration of equations for wave propagation in our anatomical model of the LV, which is the best possible way to account for anisotropy. In particular, we develop a model on a rectangular domain and represent anisotropy and the LV shape by means of parameter changes. Second, we vary

the geometry and anisotropy parameters to study how the rotation of the fibre orientation affects wave propagation and show that rotational anisotropy accelerates the spread of electrical excitation in the heart.

3.2 Total fibre angle α as a measure for anisotropy

Overall, we can consider the anatomical model as a map from a rectangular domain $\gamma_0 \le \gamma \le \gamma_1$; $0 \le \psi \le \pi/2$; $0 \le \phi < 2\pi$ to the shape of LV with anisotropy explicitly given by Eqs. (2.43)–(2.45). The total fibre rotation angle $\Delta\alpha_1$ is defined as the difference between the epicardial and endocardial helix angles α_1 measured at the LV basal zone $\psi = \pi/8$ (see [105] for details). It can be varied by changing the values of the parameters γ_0 and γ_1:

$$\alpha_1(\gamma^*, \psi^*) = \widehat{\left(\mathbf{p}, \mathrm{pr}_{\mathbf{n}}\mathbf{v}\right)}\Big|_{\gamma=\gamma^*, \psi=\psi^*, \phi=0,}$$

$$\Delta\alpha_1(\gamma_0, \gamma_1) = \alpha_1(\gamma_1, \pi/8) - \alpha_1(\gamma_0, \pi/8), \tag{3.1}$$

where $\mathbf{p}$ is the tangent vector to the parallel $\gamma = \text{const}$, $\psi = \text{const}$ at the point $\gamma = \gamma^*$, $\psi = \psi^*$, $\phi = 0$ (the geometric model is axisymmetric; therefore the choice of ϕ is arbitrary); $\mathbf{n}$ is the normal vector to the epicardium passing through the same point; $\mathbf{v}$ is the fibre direction vector (it is defined by Eq. (2.43)–(2.45)); pr is the projection operator; and $\widehat{(\mathbf{u}, \mathbf{w})}$ denotes the angle between the vectors $\mathbf{u}$ and $\mathbf{w}$. We have chosen the value $\psi = \pi/8$ because in this case, the total fibre rotation angle changes uniformly enough depending on the values of $\gamma_{0,1}$ we use (see Table 3.2 and section "Parameter values" below). For short, below we will denote $\Delta\alpha_1(\gamma_0, \gamma_1)$ as α without argument. We use it in the present study to investigate the effect of fibre rotation on wave propagation in the heart.

3.3 Electrophysiological model

To describe the excitation of cardiac tissue, we use the detailed ionic model for human ventricular cells from [118,120]. The model uses reaction-diffusion equations

to describe the evolution of the transmembrane potential $u = u(\mathbf{r}, t)$:

$$\frac{\partial u}{\partial t} = \operatorname{div}(\mathbf{D} \operatorname{grad} u) - \frac{I_{ion}}{C_m}, \tag{3.2}$$

$$I_{ion} = I_{Kr}+I_{Ks}+I_{K1}+I_{to}+I_{Na}+I_{bNa}+I_{CaL}+I_{bCa}+I_{NaK}+I_{NaCa}+I_{pCa}+I_{pK}. \tag{3.3}$$

Here, the intracellular processes are captured by $I_{ion} = I_{ion}(\mathbf{r}, t)$, which is the sum of the ionic transmembrane currents; C_m is the capacitance of the cell membrane. The locally varying diffusion matrix $\mathbf{D}$ accounts for myofibre anisotropy. As in [118], the diffusion matrix $\mathbf{D} = \left(D^{ij}\right)$ was computed from the unit vectors in fibre direction $\mathbf{v}$ using formula

$$D^{ij} = D_2\delta_{i,j} + (D_1 - D_2)v_i v_j, \tag{3.4}$$

where D_1 and D_2 are the diffusion coefficients along and across the fibres and $\delta_{i,j}$ is the Kronecker symbol.

3.4 Laplacian in implicit curvilinear coordinates

The Laplacian is an important term in the reaction-diffusion equation as it is responsible for the modelling of electrical wave spreading. It can be written as $\operatorname{div}(\mathbf{D} \operatorname{grad} f)$, where f is the transmembrane potential and $\mathbf{D}$ is an anisotropic local diffusion matrix.

Below, we calculate the Laplacian for anisotropic diffusion in the Cartesian and the special CS.

3.4.1 The Cartesian coordinate system

For an arbitrary diffusion matrix $\mathbf{D} = D^{ij}$

$$\operatorname{div}(\mathbf{D} \operatorname{grad} f) = \sum_{i,j} \frac{\partial D^{ji}}{\partial x_j} \cdot \frac{\partial f}{\partial x_i} + \sum_{i,j} D^{ij} \frac{\partial^2 f}{\partial x_i \, \partial x_j}. \tag{3.5}$$

In consideration of Eq. (3.4), one can write:

$$\operatorname{div}(\mathbf{D} \operatorname{grad} f) = (D_1 - D_2) \cdot \sum_{i,j} \frac{\partial (v_i v_j)}{\partial x_j} \cdot \frac{\partial f}{\partial x_i} + \sum_{i,j} D^{ij} \frac{\partial^2 f}{\partial x_i \, \partial x_j}. \tag{3.6}$$

3.4.2 The curvilinear coordinate system

Here we deduce from Eq. (3.6) the proper form of the Laplacian in the curvilinear coordinates ξ_0, ξ_1, ξ_2. Let us consider v_i and f as functions of ξ_0, ξ_1, ξ_2. We calculate three types of derivatives. First, one has

$$\frac{\partial(v_i v_j)}{\partial x_j} = \frac{\partial v_i}{\partial x_j} \cdot v_j + \frac{\partial v_j}{\partial x_j} \cdot v_i, \tag{3.7}$$

where

$$\frac{\partial v_i}{\partial x_j} = \sum_k \frac{\partial v_i}{\partial \xi_k} \cdot \frac{\partial \xi_k}{\partial x_j}. \tag{3.8}$$

Secondly, we evaluate

$$\frac{\partial f}{\partial x_i} = \sum_j \frac{\partial f}{\partial \xi_j} \cdot \frac{\partial \xi_j}{\partial x_i}; \tag{3.9}$$

and thirdly,

$$\frac{\partial^2 f}{\partial x_i\, \partial x_j} = \sum_k \frac{\partial^2 f}{\partial x_i\, \partial \xi_k} \cdot \frac{\partial \xi_k}{\partial x_j}, \tag{3.10}$$

where

$$\frac{\partial^2 f}{\partial x_i\, \partial \xi_k} = \sum_j \frac{\partial^2 f}{\partial \xi_k\, \partial \xi_j} \cdot \frac{\partial \xi_j}{\partial x_i}. \tag{3.11}$$

The difficulty now lies in the fact that the functions $x_j(\xi_k)$ define the ξ_k only implicitly. To evaluate the necessary derivatives, we need the following matrices:

$$\mathbf{J} = (J_{ij}) = \left(\frac{\partial \xi_i}{\partial x_j}\right), \tag{3.12}$$

$$\mathbf{W} = (W_{ij}) = \left(\frac{\partial v_i}{\partial x_j}\right), \qquad \mathbf{S} = (S_{ij}) = \left(\frac{\partial v_i}{\partial \xi_j}\right), \tag{3.13}$$

$$\mathbf{T}^k = (T^k_{ij}) = \left(\frac{\partial^2 \xi_k}{\partial x_i\, \partial x_j}\right), \qquad \mathbf{H}^k = (H^k_{ij}) = \left(\frac{\partial^2 x_k}{\partial \xi_i\, \partial \xi_j}\right). \tag{3.14}$$

The matrices are linked between themselves with the following relations:

$$\mathbf{W} = \mathbf{S}\mathbf{J}, \tag{3.15}$$

$$T^k_{mp} = -\sum_l J_{kl} (\mathbf{J}^T \mathbf{H}^l \mathbf{J})_{mp}.$$

We substitute (3.7), (3.9), (3.11) to (3.6) and get:

$$\operatorname{div}(\mathbf{D} \operatorname{grad} f) = \sum_k p_k \cdot \frac{\partial f}{\partial \xi_k} + \sum_{k,l} q_{kl} \cdot \frac{\partial^2 f}{\partial \xi_k\, \partial \xi_l},$$

where

$$p_k = D_2 \operatorname{tr} \mathbf{T}^k + (D_1 - D_2) \cdot \left((\mathbf{Jv})_k \cdot \operatorname{tr}(\mathbf{SJ}) + (\mathbf{JSJv})_k + \mathbf{v}^{\mathrm{T}} \mathbf{T}^k \mathbf{v} \right), \quad (3.16)$$

q_{kl} are elements of matrix $\mathbf{Q}$:

$$\mathbf{Q} = \mathbf{JDJ}^{\mathrm{T}}. \quad (3.17)$$

3.5 Boundary conditions

Let $\mathbf{n}$ be a normal vector to one of the LV boundary surfaces. For outer domain boundaries, we use a no-flux condition on the current.

3.5.1 Isotropic case, cylindrical coordinate system

One can write the boundary condition as

$$\frac{\partial f}{\partial n}(\rho, \phi, z) = 0. \quad (3.18)$$

By the definition of directional derivative and since the normal vector to the LV boundary lies in our problem always in the corresponding meridional half-plane,

$$\frac{\partial f}{\partial \rho} n_\rho + \frac{\partial f}{\partial z} n_z = 0, \quad (3.19)$$

where n_ρ and n_z are the normal vector components in the meridional half-plane.

3.5.1.1 The equator

On the equator, $n_\rho = 0$, so (3.19) reduces to

$$\frac{\partial f}{\partial z} = 0. \quad (3.20)$$

3.5.1.2 The epicardium

On the epicardium, $n_\rho = (d + h) \cos \psi$, $n_z = -(r + l)\varepsilon_s$, so one can write (3.19) as

$$\frac{\partial f}{\partial \rho} \cdot (d + h) \cos \psi - \frac{\partial f}{\partial z} \cdot (r + l)\varepsilon_s = 0. \quad (3.21)$$

Everywhere on the epicardium, except the apex,

$$\frac{\partial f}{\partial \rho} = \frac{(r+l)\cdot\varepsilon_s}{(d+h)\cdot\cos\psi}\cdot\frac{\partial f}{\partial z}. \tag{3.22}$$

On the apex, $\cos\psi = 0$, $\varepsilon_s = \varepsilon > 0$, so the boundary condition looks like $\frac{\partial f}{\partial z} = 0$.

3.5.1.3 The endocardium

On the endocardium, $n_\rho = d\cos\psi$, $n_z = -r\varepsilon_s$, so (3.19) can be written as

$$\frac{\partial f}{\partial \rho}\cdot d\cos\psi - \frac{\partial f}{\partial z}\cdot r\varepsilon_s = 0. \tag{3.23}$$

Everywhere on the endocardium, except the apex,

$$\frac{\partial f}{\partial \rho} = \frac{r\varepsilon_s}{d\cos\psi}\cdot\frac{\partial f}{\partial z}. \tag{3.24}$$

On the apex of the endocardium, like the epicardium, the boundary condition is $\frac{\partial f}{\partial z} = 0$.

3.5.2 Isotropic case, special coordinate system

In the special CS, we use $\frac{\partial f}{\partial \gamma}$ and $\frac{\partial f}{\partial \psi}$. Let us take into account that

$$\frac{\partial f}{\partial \rho} = \frac{\partial f}{\partial \gamma}\cdot\frac{\partial \gamma}{\partial \rho} + \frac{\partial f}{\partial \psi}\cdot\frac{\partial \psi}{\partial \rho} \tag{3.25}$$

and

$$\frac{\partial f}{\partial z} = \frac{\partial f}{\partial \gamma}\cdot\frac{\partial \gamma}{\partial z} + \frac{\partial f}{\partial \psi}\cdot\frac{\partial \psi}{\partial z}. \tag{3.26}$$

3.5.2.1 The equator

Formula (3.20) can be rewritten as

$$\frac{\partial f}{\partial \psi} = \frac{(r+\gamma l)(1-\varepsilon)}{l}\cdot\frac{\partial f}{\partial \gamma}. \tag{3.27}$$

3.5.2.2 The epicardium

Formula (3.21) becomes

$$\frac{\partial f}{\partial \gamma} = \frac{l(r+l)\varepsilon_c\varepsilon_s - (d+h)h\sin\psi\cos\psi}{(d+h)^2\cos^2\psi + (r+l)^2\varepsilon_s^2} \cdot \frac{\partial f}{\partial \psi}. \tag{3.28}$$

3.5.2.3 The endocardium

Formula (3.23) yields

$$\frac{\partial f}{\partial \gamma} = \frac{lr\varepsilon_c\varepsilon_s - dh\sin\psi\cos\psi}{d^2\cos^2\psi + r^2\varepsilon_s^2} \cdot \frac{\partial f}{\partial \psi}. \tag{3.29}$$

Note that two last formulae, if $\varepsilon > 0$, cannot have zero values in the denominators and can be directly applied to the LV apex points.

3.5.3 Anisotropic case, special coordinate system

The boundary condition is

$$\mathbf{nD}\,\mathrm{grad}\, f = 0, \tag{3.30}$$

with $\mathbf{n}$, the normal to the LV surface.

3.5.3.1 The epi- and endocardium

Let us write (3.30) in detail:

$$\sum_{i,j} n_i D^{ij} \frac{\partial f}{\partial x_j} = 0;$$

$$\sum_{i,j} \left(n_i D^{ij} \cdot \sum_k \frac{\partial f}{\partial \xi_k} \cdot \frac{\partial \xi_k}{\partial x_j} \right) = 0;$$

$$\sum_k \left(\sum_{i,j} n_i D^{ij} \frac{\partial \xi_k}{\partial x_j} \right) \cdot \frac{\partial f}{\partial \xi_k} = 0;$$

$$\mathbf{n}^{\mathrm{T}}\mathbf{D}\mathbf{J}^{\gamma}\frac{\partial u}{\partial \gamma} + \mathbf{n}^{\mathrm{T}}\mathbf{D}\mathbf{J}^{\psi}\frac{\partial u}{\partial \psi} + \mathbf{n}^{\mathrm{T}}\mathbf{D}\mathbf{J}^{\phi}\frac{\partial u}{\partial \phi} = 0. \tag{3.31}$$

Here, $\mathbf{J}^{\gamma,\psi,\phi}$ are columns of derivatives of these special variables by Cartesian coordinates (see (3.12)):

$$\mathbf{J}^{\gamma} = \begin{pmatrix} \partial\gamma/\partial x \\ \partial\gamma/\partial y \\ \partial\gamma/\partial z \end{pmatrix},$$

and so on.

3.5.3.2 The equator

Let us write (3.30) detailed as the following:

$$n_x(D\,\mathrm{grad}\,f)_x + n_y(D\,\mathrm{grad}\,f)_y + n_z(D\,\mathrm{grad}\,f)_z = 0. \tag{3.32}$$

Vector $\mathbf{n}$ is collinear to the Oz axis, so $n_x = n_y = 0$. The equation (3.32) goes over

$$(D\,\mathrm{grad}\,f)_z = 0.$$

Writing down the matrix product:

$$\sum_j D^{2j}\frac{\partial f}{\partial x_j} = 0,$$

we substitute (3.9) to this equation:

$$\sum_k \left(\sum_j D^{2j}\frac{\partial \xi_k}{\partial x_j}\right)\frac{\partial f}{\partial \xi_k} = 0.$$

Let us express $\frac{\partial f}{\partial \psi}$:

$$\frac{\partial f}{\partial \psi} = -\frac{\left(D^{20}\gamma_x + D^{21}\gamma_y + D^{22}\gamma_z\right)\frac{\partial f}{\partial \gamma} + \left(D^{20}\phi_x + D^{21}\phi_y + D^{22}\phi_z\right)\frac{\partial f}{\partial \phi}}{D^{20}\psi_x + D^{21}\psi_y + D^{22}\psi_z}.$$

We can calculate the derivatives of γ, ϕ, ψ by x, y, z:

$$\gamma_x = \gamma_\rho\rho_x = -\frac{\cos\phi}{l}; \qquad \gamma_y = \gamma_\rho\rho_y = -\frac{\sin\phi}{l}; \qquad \gamma_z = \frac{(r+\gamma l)(1-\varepsilon)}{(d+\gamma h)l};$$

$$\phi_x = -\frac{\sin\phi}{\rho}; \qquad \phi_y = \frac{\cos\phi}{\rho}; \qquad \phi_z = 0;$$

$$\psi_x = \psi_y = 0; \qquad \psi_z = -\frac{1}{d+\gamma h}.$$

So

$$\frac{\partial f}{\partial \psi} = \frac{1}{D^{22} l (r+\gamma l)} \cdot \Big[\left((D^{20} x + D^{21} y) \cdot (d+\gamma h) - D^{22} (r+\gamma l)^2 (1-\varepsilon) \right) \frac{\partial f}{\partial \gamma} + \\ + l(d+\gamma h) \cdot \left(D^{20} \sin\phi - D^{21} \cos\phi \right) \frac{\partial f}{\partial \phi} \Big]. \tag{3.33}$$

3.6 Numerical scheme for the special coordinate system

We developed a numerical procedure that allows us to use the analytical representation of cardiac anatomy and anisotropy described in the previous section. In particular, as our anatomical model is just a map from a rectangular domain $\gamma_0 \le \gamma \le \gamma_1$; $0 \le \psi < \pi/2$; $0 \le \phi < 2\pi$ to the shape of LV, we can formulate our approach in that rectangular domain. The shape of the heart, as well as anisotropy, will then be a curvilinear coordinate system (2.40)–(2.42) defined on that domain. We need to recalculate Eq. (3.2) with no-flux boundary conditions in those coordinates. The computation presented in previous section results in the following expression of the diffusion term:

$$\operatorname{div}(\mathbf{D} \operatorname{grad} u) = \sum_k p_k \cdot \frac{\partial u}{\partial \xi_k} + \sum_{k,l} q_{kl} \cdot \frac{\partial^2 u}{\partial \xi_k \, \partial \xi_l}, \tag{3.34}$$

where $\xi_1 = \gamma, \xi_2 = \psi, \xi_3 = \phi$, and p_k and q_{kl} are coefficients given by the explicit analytical Eqs. (3.16) and (3.17) that depend only on the geometry of the LV and on the diffusion matrix.

For numerical time integration of the model (2.43)–(2.45), (3.2), (3.3), we use the explicit Euler method on a discrete grid in the $(\gamma,\ \psi,\ \phi)$ space. We initially use a uniform grid with the γ-indices of the nodes denoted as $i = 0, 1, \ldots n_\gamma$; the ψ-indices as $j = 0, 1, \ldots n_\psi$; and the ϕ-indices as $k = 0, 1, \ldots n_\phi$.

Although this grid is uniform in the (γ, ψ, ϕ) space, it is essentially non-uniform because distances between the grid points substantially decrease when ψ approaches $\pi/2$, which is similar to the situation at the pole in a polar CS. To account for this problem, we exclude some points from our uniform grid in the following way. We first choose a threshold value of distance $d_{\min}$. Then, at $\gamma = \gamma_1$ (i.e., at the epicardial surface) and any given $\psi = \psi_j$, we calculate the distances between the node at $\phi = 0$: $(\gamma = \gamma_1, \psi = \psi_j, \phi = 0)$ and node $(\gamma = \gamma_1, \psi = \psi_j, \phi = \phi_k)$. We find minimal k satisfying two conditions: (1) the distance to the k-node from the node at $\phi = 0$ is more than the threshold value $d_{\min}$; and (2) k is a divisor of n_ϕ. We denote this number as K_j (as it depends on ψ_j). If ψ is far from $\pi/2$, then $K_j = 1$ and we use all nodes of our uniform (γ_i, ψ_j, ϕ_k) grid. When ψ approaches the value of $\pi/2$, $K_j > 1$ and we drop all nodes between $(\gamma = \gamma_1, \psi = \psi_j, \phi = 0)$ and $(\gamma = \gamma_1, \psi = \psi_j, \phi = K_j)$, then the next node will be $(\gamma = \gamma_1, \psi = \psi_j, \phi = 2K_j)$ etc. Thus, only nodes with the ϕ-indices 0, K_j, $2K_j, \ldots$ will be taken for evaluation of the Laplacian. After each time step, we compute values for all variables of our model in the omitted nodes using linear interpolation. With this approach, we reduce the number of grid elements in the ϕ-direction in the apical region; otherwise, this would have lowered the maximal time step in our explicit integration scheme.

The no-flux boundary condition in our problem is

$$\mathbf{nD}\,\mathrm{grad}\,u = 0, \tag{3.35}$$

where $\mathbf{n}$ is a normal to surface. We rewrite this equation in our special CS and obtain the following expression:

$$c_\gamma \frac{\partial u}{\partial \gamma} + c_\psi \frac{\partial u}{\partial \psi} + c_\phi \frac{\partial u}{\partial \phi} = 0, \tag{3.36}$$

where c_γ, c_ψ, c_ϕ are coefficients given by Eqs. (3.31) and (3.33). In order to satisfy the boundary condition, we add nodes at the domain boundaries in the following way. In the special CS, the domain of integration is a rectangle (with periodic boundary in ϕ), and at $\psi = \pi/2$ we have a pole (i.e., also no boundary). Therefore,

we have only three boundaries, namely at $\gamma = \gamma_0$ (i.e., $i = 0$), $\gamma = \gamma_1$ ($i = n_\gamma$), and $\psi = 0$ ($j = 0$). Layers with $(-1, j, k)$, $(n_\gamma + 1, j, k)$, and $(i, -1, k)$ are added. We then solve equation (3.36) on the three boundary surfaces to find values in the added nodes. Subsequently, we can compute Laplacian at all other nodes in the domain using, if necessary, the values in the additional nodes. Due to this procedure, they will satisfy the boundary conditions.

We have programmed this approach using C in the CodeBlocks IDE, a Mingw compiler, and Windows 7. The OpenMP technology has been used for parallelization, and Paraview and Irfan have been used for visualisation. The formal parameters of our numerical scheme have been given in the methods section above. Such an approach allows us to compute various regimes of wave propagation in a model of LV with good representation of boundary conditions and to study various effects of anisotropy on wave propagation patterns.

3.7 Parameter values and problem to solve

We used the following parameters from [105, Table 2]: the LV equatorial radius $r^e = 23$ mm, the equatorial wall thickness $l^e = 10$ mm, the LV cavity depth $d^e = 53$ mm, the apical wall thickness $h^e = 7$ mm, the conicity-ellipticity parameter $\varepsilon = 0.9$, and the spiral surface torsion angle $\phi^e_{\max} = 3\pi$ [105, Fig. 3c]. The threshold distance between the adjacent nodes $d_{\min}$ was set to 0.3 mm.

Our mesh had a distance of 0.2 to 0.3 mm between the nodes and before the deletion of the nodes described above had $n_\gamma = 40$, $n_\psi = 300, n_\psi = 800$. The diffusion coefficient along the fibres was $D_1 = 0.3$ mm^2/ms. The diffusion coefficient across the fibres D_2 was varied between different experiments depending on whether we modeled isotropy or anisotropy.

For point stimulation, we increased the value of the variable u from the resting potential of -86.2 mV to $u = 0$ mV at the first time step in small regions located at three different sites. In the A series, it was a small epicardial region at the apex;

in the B series, at the centre of LV epicardium; in the C series, at the centre LV endocardium (see Table 3.1).

Table 3.1: *The initial excitation areas*

Series	γ-indices	ψ-indices	ϕ-indices	area
A	$i \geq n_\gamma - 4$	$j \geq n_\psi - 4$	all	apical epicardium
B	$i \geq n_\gamma - 4$	$\lvert j - (n_\psi/2)\rvert \leq 2$	$k \leq 4$	central epicardium
C	$i \leq 4$	$\lvert j - (n_\psi/2)\rvert \leq 2$	$k \leq 4$	central endocardium

We studied the effect of the fibre rotation on the spread of excitation. With this purpose, we generated a series of LV models that differ in the total fibre rotation angle through the myocardial wall. The parameters of the model are listed in Table 3.2. Note that although the values of γ_0 and γ_1 differ between the models, they affect only fibre rotation, and the LV geometry is exactly the same for all models due to the rescaling procedure described in [88, Sec. 1.4]. Also note that the change in fibre rotation results in the change in fibre angle at the epicardial surface (see column "α" of Table 3.2).

The time step was equal to 0.005 ms for the isotropical cases and 0.01 ms for the anisotropical ones.

We considered that a wave came to a node when the potential in the node was more than -80 mV the first time.

3.8 Numerical results

3.8.1 Activation maps

We applied our approach to study the effect of anisotropy on the spread of excitation in the heart. In particular, we initiated a wave at several locations and studied how the wave arrival time depended on the two main features of anisotropy. Our first anisotropy parameter was the ratio of the diffusion coefficients D_1:D_2 along

Table 3.2: **Dependence of the total fibre angle α on the model parameters $\gamma_{0,1}$**

Model	γ_0	γ_1	The helix angle near the base at		The total fibre rotation angle α
			the epicardium	the endocardium	
1	0.3	0.55	$-13°$	$3°$	$16°$
2	0.2	0.7	$-40°$	$29°$	$69°$
3	0.1	0.85	$-69°$	$64°$	$133°$
4	0	1	$-87°$	$87°$	$174°$

and across the fibres. Second, we independently varied the total rotation angle α of fibres through the myocardial wall. We also compared our results with the spread of excitation in an isotropic model of the LV where $D_1 = D_2$.

Fig. 3.1 shows the wave arrival time after stimulation of the small apical epicardial zone A for ratios D_1:D_2 equal to 1:0.111 or 1:0.25 (shown at the top of the figure) and four different rotation angles of the fibres, which are displayed in the left column. We see that in this first example, all the figures are axisymmetrical, which is a consequence of the axisymmetric properties of our model and the initial conditions.

We see that for the low rotation angle (the upper row), the speed of the upward wave propagation for the diffusion coefficient ratio of 1:0.111 is substantially smaller than that for the ratio of 1:0.25. However, if the fibre rotation angle increases (the lower rows), the difference in the speed between the two anisotropy ratios decreases. For the rotation angle of 174° (the lower row), the excitation patterns for both anisotropy ratios become close to each other. Thus, we observe that fibre rotation increases the velocity of the spread of excitation and also decreases the effect of anisotropy.

Let us now consider the case of lateral stimulation for a given ratio of the diffusion coefficients of 1:0.111; the results for epi- and endocardial stimulation are presented in Figs. 3.2 and 3.4. After epicardial stimulation, the wave initially fol-

lows the fibre direction. In Fig. 3.2, we note a displacement of the early activation zones (red) due to the change in fibre direction at the epicardium in our anatomical model (see column 4 of Table 3.2). However, for endocardial stimulation (Fig. 3.4, the first column), the shift of the early activation zone (red) on the epicardium is attenuated by fibre rotation. As in Fig. 3.2, we see that an increase in the rotation angle causes a decrease in the arrival time. In addition, in the second column in Fig. 3.2, we see that in both cases, the excitation patterns have a clear V shape on the surface opposite the stimulation site, which is a mere consequence of the shape of the heart (see [75, 77]).

Figs. 3.3 and 3.5 show the arrival time after lateral stimulation in a case of decreased anisotropy, i.e., for a diffusion coefficient ratio of 1:0.25. The excitation patterns resemble those from Fig. 3.2 and Fig. 3.4 respectively, with similar effects of fibre rotation on the epicardial stimulation and V-shaped patterns. Here, we also observe that an increase in the rotation angle decreases the overall excitation time. We also note a compensating effect of fibre rotation on the degree of anisotropy. The difference between the corresponding panels in Fig. 3.2 and Fig. 3.3 (and also Fig. 3.4 and Fig. 3.5) is more pronounced for a lower fibre rotation rate (rotation angle 16°).

3.8.2 Average speed of excitation

Now let us quantify the effects of rotation and anisotropy on wave propagation. In order to do this, we use the following procedure. We group all points of the heart to bins differing by their "distance" from the stimulation point. We define the distance as the arrival time from the stimulation to a given point. To calculate the distances, we perform simulations in which we initiate a wave at the same locations as in Figs. 3.1–3.5. However, for the isotropic medium, we use a diffusion coefficient of $D_1 = D_2 = 0.3$ mm^2/ms. We generate 40 groups in which points differ in the arrival time by 2 ms. Then we determine the average arrival time for each of these groups for various anisotropic conditions and compare these arrival times to the arrival time in the isotropic model. As in the isotropic model, the velocity of wave

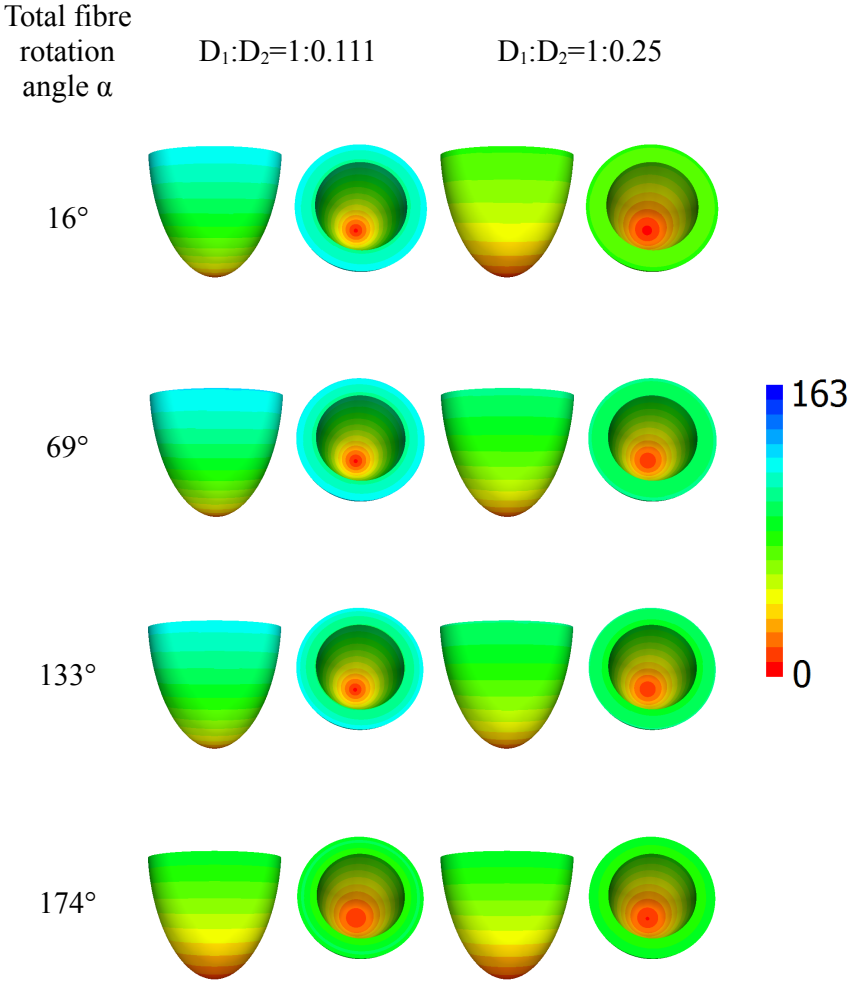

Figure 3.1: *Arrival times, ms, of the waves after point stimulation at the apex for various values of anisotropy and fibre rotation. The values of anisotropy are shown at the top of the figure and of the fibre rotation at the left column. For details see table 3.2. Arrival times are color coded in ms.*

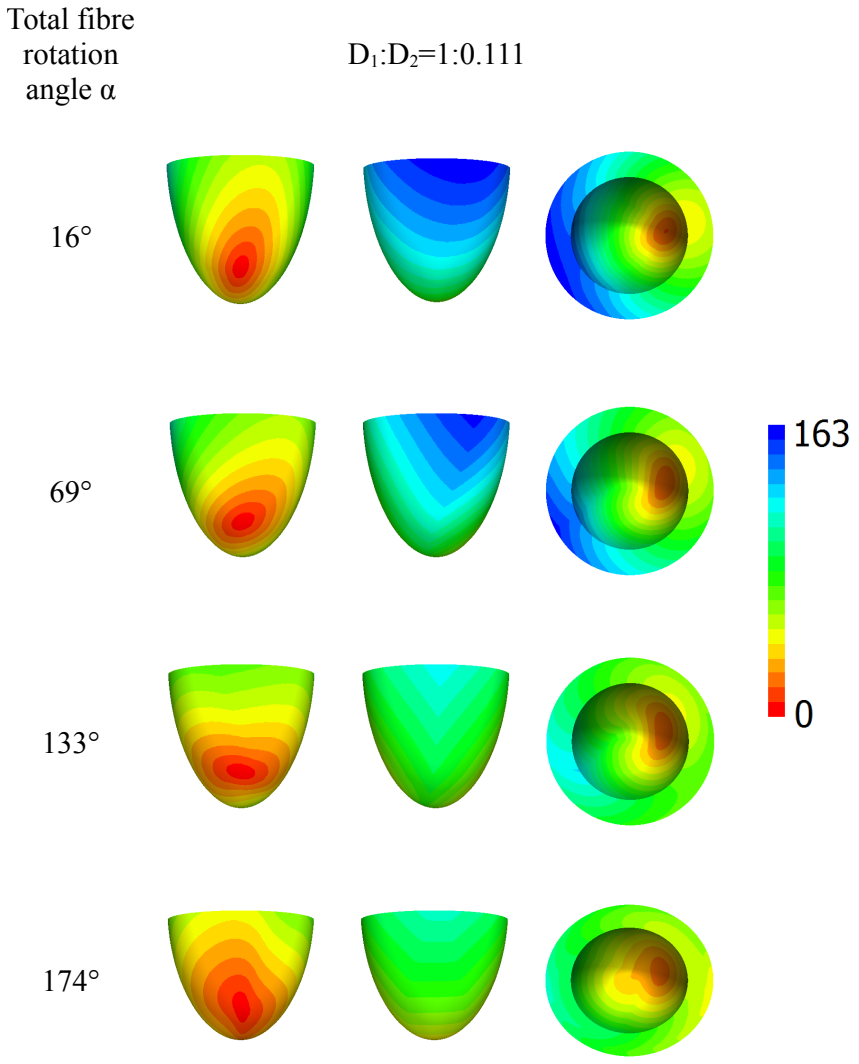

Figure 3.2: *Arrival times, ms, for the waves after point stimulation at the epicardial surface. Big anisotropy. The notations are the same as in Fig. 3.1*

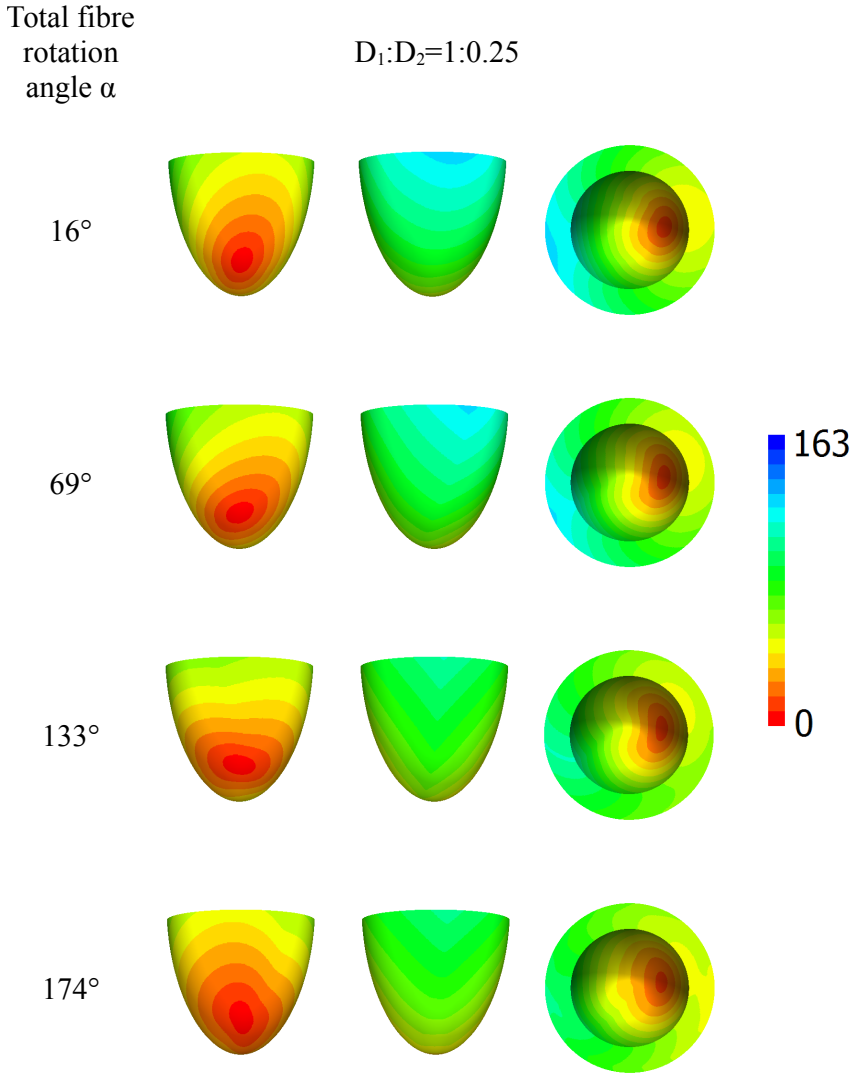

Figure 3.3: *Arrival times, ms, of the waves after point stimulation at the epicardial surface. Little anisotropy. The notations are the same as in Fig. 3.1*

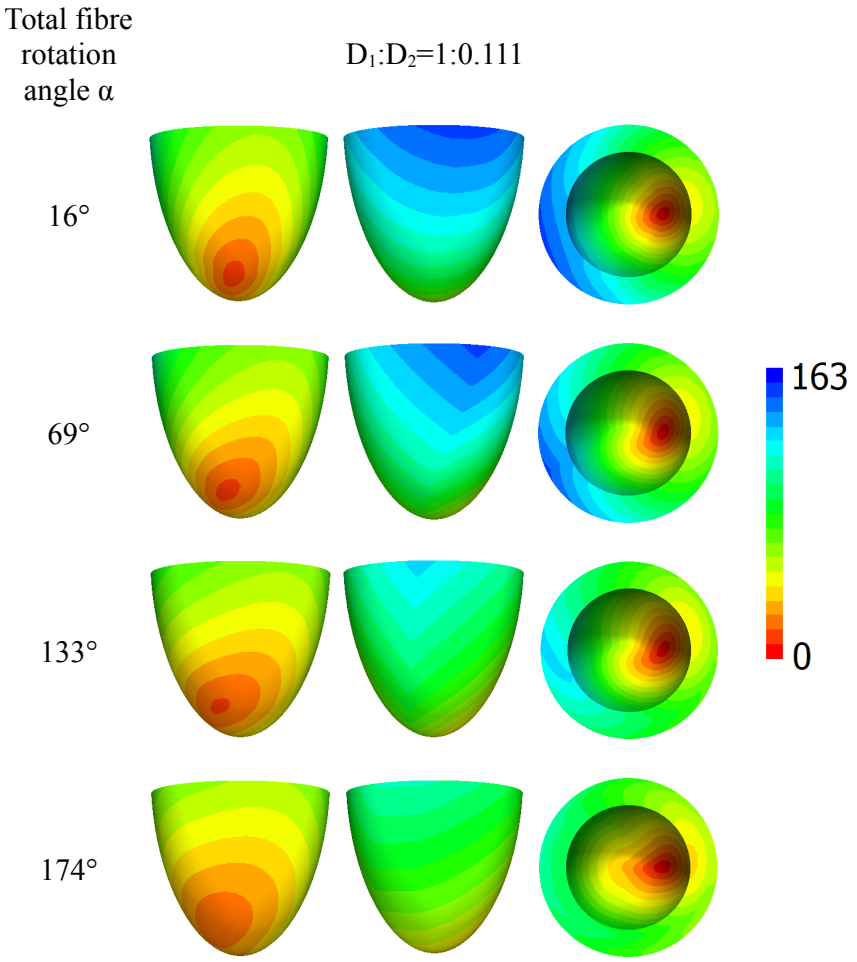

Figure 3.4: *Arrival times, ms, of the waves after point stimulation at the endocardial surface. Big anisotropy. The notations are the same as in Fig. 3.1*

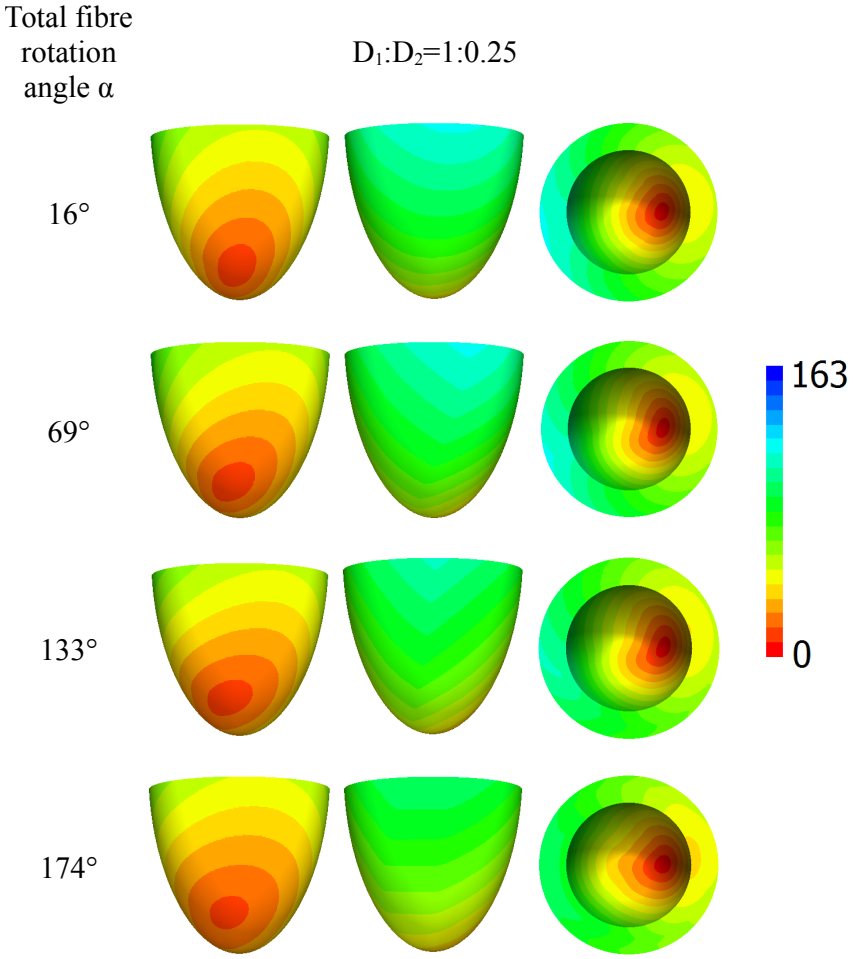

Figure 3.5: *Arrival times, ms, of the waves after point stimulation at the endocardial surface. Little anisotropy. The notations are the same as in Fig. 3.1*

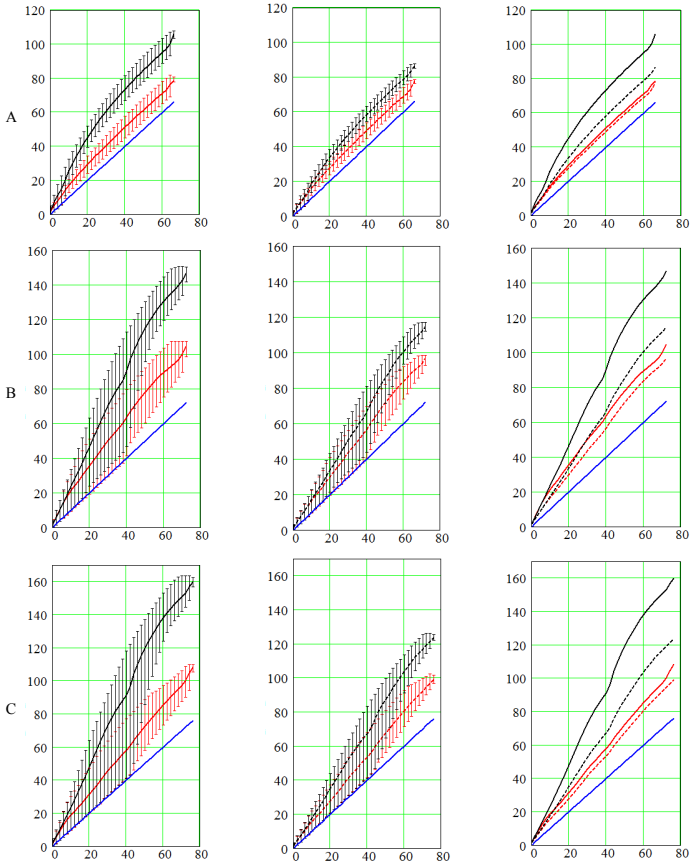

Figure 3.6: *The arrival times (ms) as a function of the distance from the stimulation point for the apical (A), epicardial (B) and endocardial (C) stimulation. The distance on the horizontal axis is measured in ms as the arrival time of the wave in the isotropic model (see text for more details). The red lines represent numerical experiments for total rotation angle* $\alpha = 174^\circ$*; the black lines, for* $\alpha = 16^\circ$*; the blue lines for isotropy. The solid lines correspond to the case* $D_1{:}D_2 = 1{:}0.111$*, while the dashed lines correspond to the case* $D_1{:}D_2 = 1{:}0.25$*. The vertical segments display minimal and maximal arrival times in each group of nodes. The average, min, max arrival times are displayed on the leftmost panels for* $D_1{:}D_2 = 1{:}0.111$*, and in the middle column for* $D_1{:}D_2 = 1{:}0.25$*. The right column compares the average arrival times.*

propagation in all directions is the same, this dependence gives us the dependence of the wave arrival time on the distance from the stimulation point. The results are shown in Fig. 3.6.

In Fig. 3.6, the red lines correspond to $\alpha = 174^\circ$ and the black lines correspond to $\alpha = 16^\circ$ fibre rotation angle in the LV wall. The fact that the red lines are always located below the black lines shows that the increase of the fibre rotation angle results in faster wave propagation.

Also, all solid lines correspond to D_1:$D_2 = 1$:0.111, while dashed lines correspond to D_1:$D_2 = 1$:0.25. If we now compare the solid and dashed lines of the same color (third column in Fig. 3.6), we see that the red lines are closer to each other than the black lines. This indicates that in presence of higher fibre rotation rotation (the red lines) the decrease of D_2 (i.e., solid vs. dashed) has a smaller effect on the arrival time. This once again illustrates that anisotropy is compensated for by the rotation of the fibres.

In addition, we see in Fig. 3.6 that the red lines always have a less steep slope than the corresponding black lines. As going from black to red shows an increase in fibre rotation, we can conclude that the increase in rotation makes propagation faster in all cases.

Scroll wave dynamics

We have also studied scroll wave dynamics for the same values of anisotropy and fibre rotation. We generated a single scroll wave located approximately at the middle between the apex and the base of the ventricle and studied its behavior for different model parameters γ_0, γ_1 and $D_1 : D_2$. We found that anisotropy substantially affects the dynamics of scroll waves. In all cases, the increase in the fibre rotation angle results in a decrease in the period of scroll wave rotation (Fig. 3.7). We see that for $D_1 : D_2 = 1 : 0.25$, when the fibre rotation angle α is increased from 16° to 174°, the period drops significantly, from 277 to 257 ms. For $D_1 : D_2 = 1 : 0.111$, we see similar dependency. In addition, the period for

the same rotation angle for $D_1 : D_2 = 1 : 0.111$ was slightly longer than for $D_1 : D_2 = 1 : 0.25$.

The scroll wave dynamics was also substantially affected by the anisotropy. In all cases, we observed a drift of the filament (Fig. 3.8). The drift always had two components, both in the vertical (ψ) and circumferential (ϕ) directions. The total velocity of drift (Fig. 3.9A) was very small, about 1 mm/s, which is about 0.2 mm per rotation; however, the drift was monotonic and persistent. The value of velocity had no clear relationship with the rotation angle; for $D_1 : D_2 = 1 : 0.25$, we see some tendency for velocity decrease with an increase in fibre rotation, while for $D_1 : D_2 = 1 : 0.111$, the dependency is strongly non-monotonic and it is maximal for the intermediate values of the fibre rotation angle. The drift direction can be seen from the sign of the vertical and horizontal components of the velocity (Figs. 3.9B, C). Here again, the direction is affected by the rotation angle; however, we also did not find any clear tendency for either drift to the apex or base of the heart depending on the rotation angle.

For $D_1 : D_2 = 1 : 0.25$, the initial scroll wave was always stable and did not break down to multiple scroll waves. For $D_1 : D_2 = 1 : 0.111$, we did observe formation of the additional sources of excitation. However, in most cases, they appeared simultaneously at a substantial distance from the initial filament and not as a result of filament buckling and breakup due to rotational anisotropy in the way it was reported in [30]. The onset of new sources had a clear correlation with the fibre rotation angle (Fig. 3.10). We did not observe any instabilities for small and big α (models 1 and 4 in Table 3.2, Figs. 3.10A, D), however, for intermediate and large values of α (Figs. 3.10B, C), we observed new sources, and their number increased with the increase of the fibre rotation angle (compare panels B and C). Note that cases presented in panels B and C correspond to the largest drift velocities of a scroll wave; thus, the onset of secondary filaments may be related to the filament drift.

We have also studied change in filament shape over time. For small values of total fibre angle α, the filament remained transmural, nearly straight, and stable.

This case is shown in Fig. 3.10A. For intermediate α equal to 69° and 133°, the filament not only drifted faster but also deformed to a transmural S or L-shape (Fig. 3.10B). For larger values of α, the filament again had a nearly straight shape (Fig. 3.10D).

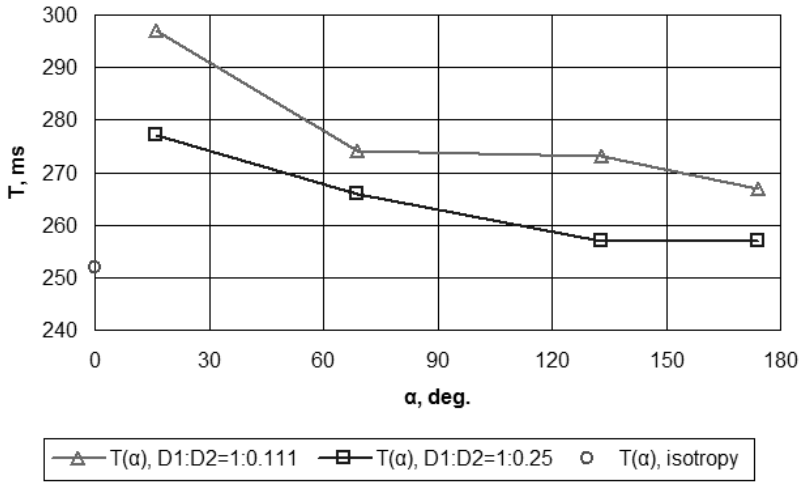

Figure 3.7: *Scroll wave rotation period T, ms, as a function of total fibre rotation angle α, deg.*

3.9 Discussion

We developed an anatomical model of the LV of the human heart using a special CS (γ, ψ, ϕ) which gives an explicit analytical map from a rectangular domain to the heart shape and fibre orientation field. This allowed us to represent the heart's geometry on a rectangular grid and explicitly write expressions for boundary conditions. This approach may be helpful for studies of any phenomena in which boundary effects are of great importance.

One important feature of our model is the possibility to change the properties of anisotropy. The most significant characteristic of LV anisotropy is the rotation

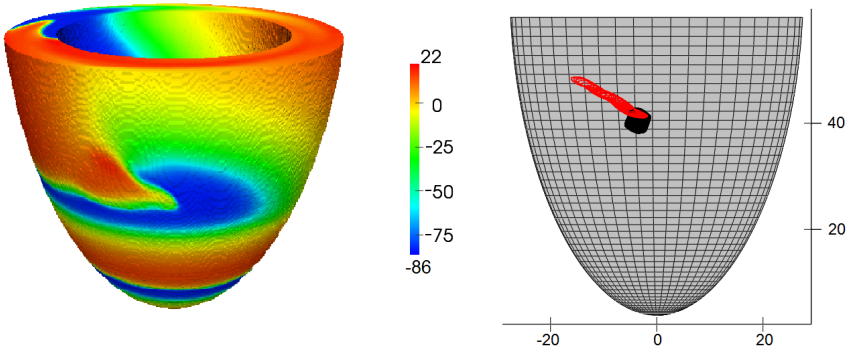

Figure 3.8: *Potential, mV, on the LV surface during scroll wave rotation (left) and tip trajectory for* $D_1 : D_2 = 1 : 0.111$ *(red line) and for* $D_1 : D_2 = 1 : 0.25$ *(black line) (right). The results are shown for model 2 (*$\gamma_0 = 0.2$, $\gamma_1 = 0.7$*, see text and Table 3.2 for details).*

of myocardial fibres through the myocardial wall. We can change the degree of this rotation in a consistent way and study its effect on normal and abnormal wave propagation in the heart. We studied its effect on wave propagation when the initial stimulation area was located at the apex and on the lateral epi- and endocardium of the LV. We found that the rotation of myocardial fibres accelerates the spread of excitation waves in the heart, which was explicitly demonstrated using models with different fibre rotation angles. This acceleration of wave propagation was discussed in [129]; it occurs because the wave can propagate with maximal speed in more directions with a larger rotation angle, which results in an overall faster wave propagation. Note that if the rotation angle is 2π or more, propagation with maximal speed will be possible in any direction, and in the limit of a large medium, the arrival time will be the same as in an isotropic medium with the velocity given by the velocity along the fibre [129]. We were able to demonstrate this in an anatomical setup in which we explicitly changed the rotation of the fibres, while in [129] it was made for a single anisotropy configuration.

Young and Panfilov considered in paper [129] wave propagation for various values of fibre rotation. However, in the simulations the tissue was represented as

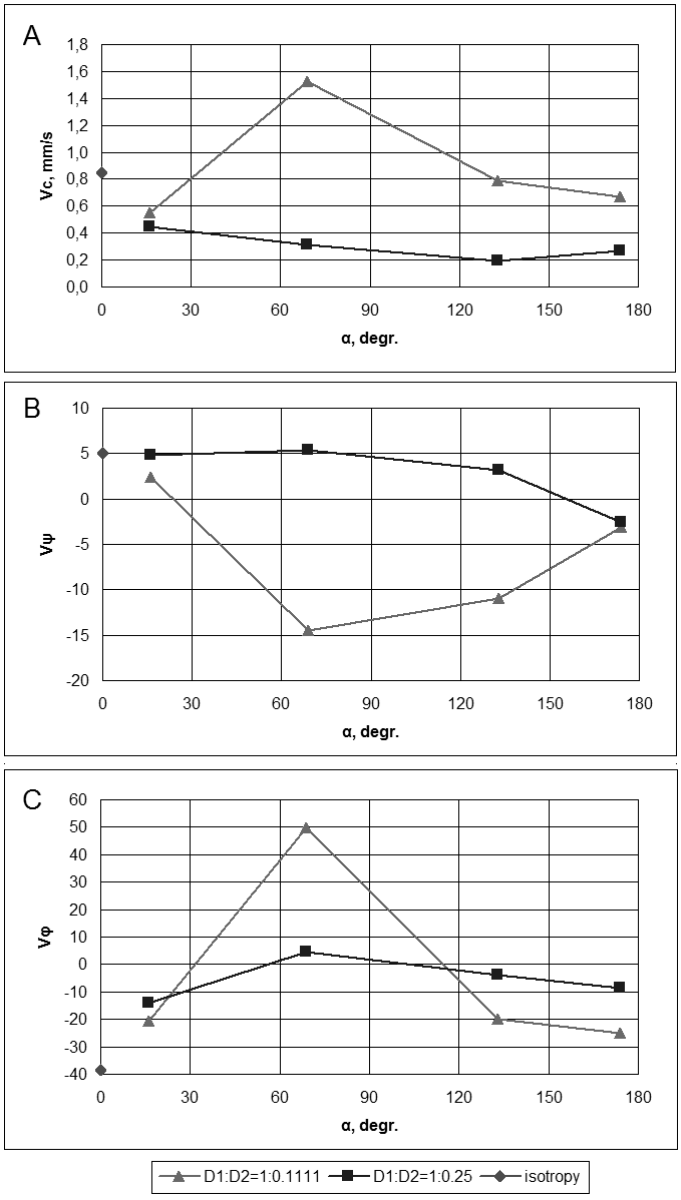

Figure 3.9: *Velocity of scroll wave filament drift for the simulation of 8 s. Average filament velocity V_c, mm/s (A). Velocity components multiplied by 1000, per second: latitudinal component v_ψ (B) and longitudinal component v_ϕ (C).*

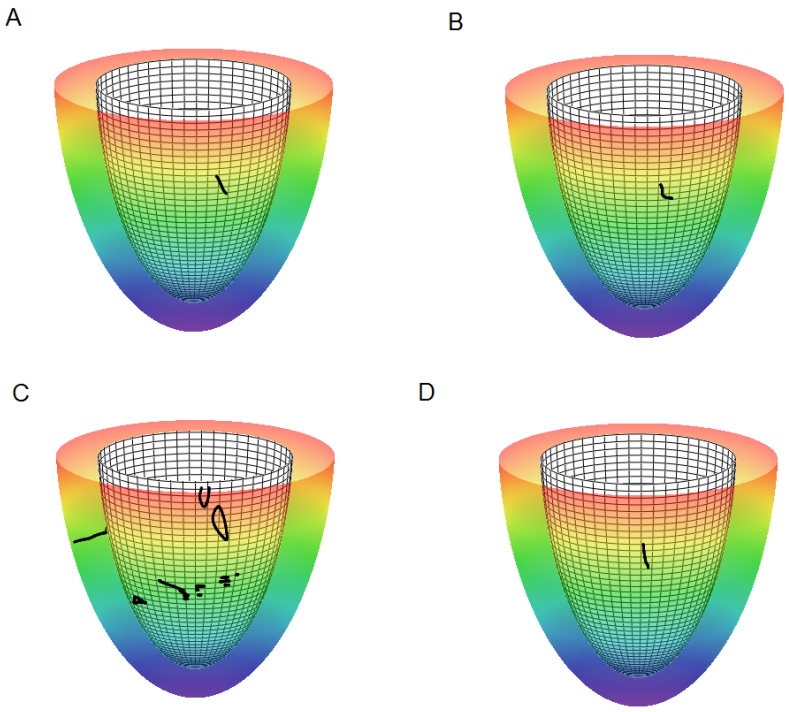

Figure 3.10: *Scroll wave filaments in the LV model. The anisotropy ratio is* $D_1 : D_2 = 1 : 0.111$. *Panels A, B, C, D: models 1, 2, 3, 4 (see Table 3.2), fibre rotation angle in the LV wall increases from panel A to panel D. The epicarduim (semitransparent colored surface; color denotes height from the red base to the purple apex), the endocardium (opaque white meshy surface), and filaments (black lines and dots).*

a simple rectangular 3-D slab in which the fibres were located in the planes parallel to the upper slab surface.

We considered more realistic ventricular architecture and morphology that includes the following features:

1. A more realistic method for the fibre rotation angle around the axes [88], so called “Japanese-fan arrangement” [105]; and

2. A realistic change of the fibre rotation angle values due to the displacement of the transmural axis from the LV apex to the base [88].

As in [129], our model also shows the faster excitation propagation with an increase in the fibre rotation angle and a decrease in the anisotropy.

In addition to studies on the effects of fibre rotation, our model can be used to investigate the possible contribution of the LV geometry to the propagation of the excitation waves. In particular, in certain forms of heart disease (e.g. dilated and hypertrophic cardiomyopathy, eccentric and concentric cardiac hypertrophy, etc. [92, chapter 8]), the shape of the ventricle becomes more spherical and the thickness of the wall also increases. Such changes in geometry can easily be accommodated in our model.

In general, the study of the effects of the LV geometry on excitation seems to be of great importance because many cardiac pathologies tightly correlate with changes in the LV geometrical characteristics. The LV becomes more dilated near the apex and thicker near the base during stress-induced ("Takotsubo") cardiomyopathy, or transient apical ballooning syndrome [92, chapter 8]. Such remodelling of the LV geometry might be mimicked in similar mathematical models via the fitting of the geometric parameters values to account for the LV shape of a particular pathology.

The results of our simulations can potentially be verified by direct measurements of wave propagation on the whole heart preparations, such as [107]. Note, however, that another factor important for overall excitation of the heart is the Purkinje conduction system. In order to compare experiments with our simulations, such measurements should be performed after chemical ablation of the Purkinje system, for example by using Lugol solution [27].

Another potentially interesting application of this approach may be its application in studies on the debrillation of cardiac tissue, in which case tissue texture and boundary conditions are also of key importance [51]. However, a bi-domain representation of cardiac tissue must be used for defibrillation [21, 43, 51], which does not fall under our present scope. Nonetheless, the extension of our approach

for such cases is straightforward. The formulae for the diffusion term (3.34) and for the boundary conditions (3.36) can be directly used for representation of the bi-domain equations in the special CS. Then, the finite difference problem can be formulated in the same way as in our case and can be solved using any existing method (see [126]).

A second set of results in this paper concerns the dynamics of transmural scroll waves. The negative correlation found for the rotation period versus fibre rotation angle α in Fig. 3.7 is different from the observations in [91] made by Qu et al., who observed an increasing period with a faster fibre rotation rate. Note, however, that their simulations used in-plane fibre rotation, while we work with a 3-D ventricular geometry. Both complementary cases can be qualitatively explained on geometrical grounds. In [91], the period was only affected by fibre rotation, which causes negative intrinsic curvature $\mathcal{R}$ of the associated curved space [129]. By its definition, negative geometrical curvature represents a saddle-like space with positive angular deficit. More specifically, in a space with curvature $\mathcal{R}$, the circumference C of a circle (ball) with small radius r amounts to [60]

$$C \approx 2\pi r \left(1 - \frac{\mathcal{R}r^2}{12}\right). \tag{3.37}$$

As the spiral tip in each cross-section needs to travel along a larger closed path of length C before completing a period, negative $\mathcal{R}$ is expected to increase the rotation period. Therefore, the trend found in [91] can be expected if the fibre rotation is the main determinant of the rotation period. In our present model, however, a transmural filament consists of spiral waves' tips in different layers of constant depth γ. These γ-surfaces are sphere-like and therefore have positive $\mathcal{R}$. Thus, under normal excitability, the sphericity of the LV will decrease the rotation period [24, 132]. We conclude that in general, the rotation period of scroll waves in the heart may decrease or increase with increasing fibre rotation angle α, depending on the relative strengths of the competing effects of the fibre rotation rate and the extrinsic curvature (sphericity) of the LV cavity.

Regarding the non-monotonic dependence of filament drift velocity versus total rotation angle, we first note that the creation of secondary filaments in the regime of intermediate α is consistent with the clinical or experimental picture of a "mother rotor" during cardiac arrhythmias [99, 116]. In such a scenario, the primary filament (mother rotor) remains stable and creates secondary sources that further disturb the electrical excitation of the heart, leading to cardiac arrest. In our simulations, we also see a similar situation with a stable mother rotor, which was always sustained until the end of the simulation time, and secondary excitation sources induced at some distance from it.

In this thesis, we studied wave propagation due to point stimulation and scroll waves. Other important wave propagation regimes include various types of scroll waves and turbulent patterns [70, 71, 73, 82]. It was shown that heterogeneity [80, 97] and anisotropy [72, 76, 122] of the tissue are significant factors determining the dynamics of these sources. The effect of heterogeneity on the dynamics of spiral waves was also studied in a series of papers by Shajahan, Sinha and co-authors [62, 102–104]. In particular, in [102] they showed that some changes in the position, size, and shape of a conduction inhomogeneity can transform a single rotating spiral to spiral breakup or vice versa. Since our model provides tools for changing anisotropic properties and allows one to add heterogeneity, these effects can also be studied using our approach.

3.A TNNP model equations

$$\partial V/\partial t = -\frac{I_{ion} + I_{stim}}{C_m} + \frac{1}{\rho_x S_x C_m} V_{xx} + \frac{1}{\rho_y S_y C_m} V_{yy} \tag{3.38}$$

$$I_{ion} = I_{Na} + I_{K1} + I_{to} + I_{Kr} + I_{Ks} + I_{CaL} + I_{NaCa} +$$

$$+ I_{NaK} + I_{pCa} + I_{pK} + I_{bCa} + I_{bNa} \tag{3.39}$$

Reversal potentials

$$E_X = \frac{RT}{zF} log \frac{X_o}{X_i} \quad \text{for} \quad X = Na^+, K^+, Ca^{2+} \tag{3.40}$$

$$E_{Ks} = \frac{RT}{F} log \frac{K_o + p_{KNa} Na_o}{K_i + p_{KNa} Na_i} \tag{3.41}$$

Fast Na^+ current

$$I_{Na} = G_{Na} m^3 hj (V - E_{Na}) \tag{3.42}$$

$$m_\infty = \frac{1}{(1. + e^{(-56.86 - V)/9.03})^2} \tag{3.43}$$

$$\alpha_m = \frac{1}{1. + e^{(-60. - V)/5.}} \tag{3.44}$$

$$\beta_m = \frac{0.1}{1. + e^{(V + 35.)/5.}} + \frac{0.1}{1. + e^{(V - 50.)/200.}} \tag{3.45}$$

$$\tau_m = \alpha_m \beta_m \tag{3.46}$$

$$h_\infty = \frac{1}{(1. + e^{(V + 71.55)/7.43})^2} \tag{3.47}$$

$$\alpha_h = \begin{cases} 0 & \text{if } V \geq -40, \\ 0.057 e^{-(V + 80.)/6.8} & \text{if } V < -40. \end{cases} \tag{3.48}$$

$$\beta_h = \begin{cases} \frac{0.77}{0.13(1. + e^{-(V + 10.66)/11.1})} & \text{if } V \geq -40, \\ 2.7 e^{0.079V} + 3.1 \times 10^5 e^{0.3485V} & \text{if } V < -40. \end{cases} \tag{3.49}$$

$$\tau_h = \frac{1}{\alpha_h + \beta_h} \tag{3.50}$$

$$j_\infty = \frac{1}{(1. + e^{(V + 71.55)/7.43})^2} \tag{3.51}$$

$$\alpha_j = \begin{cases} 0 & \text{if } V \geq -40, \\ \frac{(-2.5428 \times 10^4 e^{0.2444V} - 6.948 \times 10^{-6} e^{-0.04391V})(V + 37.78)}{1. + e^{0.311(V + 79.23)}} & \text{if } V < -40. \end{cases} \tag{3.52}$$

$$\beta_j = \begin{cases} \frac{0.6e^{0.057V}}{1.+e^{-0.1(V+32.)}} & \text{if } V \geq -40, \\ \frac{0.02424e^{-0.01052V}}{1.+e^{-0.1378(V+40.14)}} & \text{if } V < -40. \end{cases} \tag{3.53}$$

$$\tau_j = \frac{1}{\alpha_j + \beta_j} \tag{3.54}$$

L-type Ca^{2+} current

$$I_{CaL} = G_{CaL} df f_{Ca} 4 \frac{VF^2}{RT} \frac{Ca_i e^{2VF/RT} - 0.341 Ca_o}{e^{2VF/RT} - 1} \tag{3.55}$$

$$d_\infty = \frac{1}{1. + e^{(-5.-V)/7.5}} \tag{3.56}$$

$$\alpha_d = \frac{1.4}{1. + e^{(-35-V)/13}} + 0.25 \tag{3.57}$$

$$\beta_d = \frac{1.4}{1. + e^{(vv+5)/5}} \tag{3.58}$$

$$\gamma_d = \frac{1}{1. + e^{(50-vv)/20}} \tag{3.59}$$

$$\tau_d = \alpha_d \beta_d + \gamma_d \tag{3.60}$$

$$f_\infty = \frac{1}{1. + e^{(V+20.)/7.}} \tag{3.61}$$

$$\tau_f = 1125 e^{-(V+27)^2/240} + 80 + \frac{165}{1 + e^{(25-V)/10}} \tag{3.62}$$

$$\alpha_{fca} = \frac{1.}{1. + (Cai/0.000325)^8} \tag{3.63}$$

$$\beta_{fca} = \frac{0.1}{1. + e^{(Cai-0.0005)/0.0001}} \tag{3.64}$$

$$\gamma_{fca} = \frac{0.2}{1. + e^{(Cai-0.00075)/0.0008}} \tag{3.65}$$

$$f_{Ca\infty} = \frac{\alpha_{fca} + \beta_{fca} + \gamma_{fca} + 0.23}{1.46} \tag{3.66}$$

$$\tau_{fCa} = 2 \tag{3.67}$$

$$\dot{f_{Ca}} = k \frac{f_{Ca\infty} - f_{Ca}}{\tau_{fCa}} \tag{3.68}$$

$$k = \begin{cases} 0 & \text{if } f_{Ca\infty} > f_{Ca} \text{ and } V > -60mV, \\ 1 & \text{otherwise.} \end{cases} \tag{3.69}$$

Transient outward current

$$I_{to} = G_{to} r s (V - E_K) \tag{3.70}$$

For all cell types:

$$r_\infty = \frac{1}{1. + e^{(20-V)/6.}} \tag{3.71}$$

$$\tau_r = 9.5 e^{-(V+40)^2/1800} + 0.8 \tag{3.72}$$

For epicardial and M cells:

$$s_\infty = \frac{1}{1. + e^{(V+20)/5}} \tag{3.73}$$

$$\tau_s = 85. e^{-(V+45)^2/320} + \frac{5}{1. + e^{(V-20.)/5.}} + 3 \tag{3.74}$$

For endocardial cells:

$$s_\infty = \frac{1}{1. + e^{(V+28)/5.}} \tag{3.75}$$

$$\tau_s = 1000 e^{-(V+67)^2/1000} + 8 \tag{3.76}$$

Slow delayed rectifier current

$$I_{Ks} = G_{Ks} x_s^2 (V - E_{Ks}) \tag{3.77}$$

$$x_{s\infty} = \frac{1}{1. + e^{(-5.-V)/14.}} \tag{3.78}$$

$$\alpha_{xs} = \frac{1100.}{\sqrt{1. + e^{(-10.-V)/6}}} \tag{3.79}$$

$$\beta_{xs} = \frac{1}{1. + e^{(V-60.)/20.}} \tag{3.80}$$

$$\tau_{xs} = \alpha_{xs} \beta_{xs} \tag{3.81}$$

Rapid delayed rectifier current

$$I_{Kr} = G_{Kr} \sqrt{\frac{K_o}{5.4}} x_{r1} x_{r2} (V - E_K) \tag{3.82}$$

$$x_{r1\infty} = \frac{1}{1. + e^{(-26.-V)/7.}} \tag{3.83}$$

$$\alpha_{xr1} = \frac{450.}{1. + e^{(-45.-V)/10.}} \tag{3.84}$$

$$\beta_{xr1} = \frac{6.}{1. + e^{(V+30.)/11.5}} \tag{3.85}$$

$$\tau_{xr1} = \alpha_{xr1}\beta_{xr1} \tag{3.86}$$

$$x_{r2\infty} = \frac{1}{1. + e^{(V+88.)/24.}} \tag{3.87}$$

$$\alpha_{xr2} = \frac{3.}{1. + e^{(-60.-V)/20.}} \tag{3.88}$$

$$\beta_{xr2} = \frac{1.12}{1. + e^{(V-60.)/20.}} \tag{3.89}$$

$$\tau_{xr2} = \alpha_{xr2}\beta_{xr2} \tag{3.90}$$

Inward rectifier K^+ current

$$I_{K1} = G_{K1}\sqrt{\frac{K_o}{5.4}}x_{K1\infty}(V - E_K), \tag{3.91}$$

$$\alpha_{K1} = \frac{0.1}{1. + e^{0.06(V-E_K-200)}} \tag{3.92}$$

$$\beta_{K1} = \frac{3.e^{0.0002(V-E_K+100)} + e^{0.1(V-E_K-10)}}{1. + e^{-0.5(V-E_K)}} \tag{3.93}$$

$$x_{K1\infty} = \frac{\alpha_{K1}}{\alpha_{K1} + \beta_{K1}} \tag{3.94}$$

Na^+/Ca^{2+} exchanger current

$$I_{NaCa} = k_{NaCa}\frac{e^{\frac{\gamma VF}{RT}}Na_i^3Ca_o - e^{\frac{(\gamma-1)VF}{RT}}Na_o^3Ca_i\alpha}{(K_{mNai}^3 + Na_o^3)(K_{mCa} + Ca_o)(1 + ksate^{\frac{(\gamma-1)VF}{RT}})} \tag{3.95}$$

Na^+/K^+ pump current

$$I_{NaK} = P_{NaK}\frac{K_o}{K_o + K_{mK}} \cdot \frac{Na_i}{Na_i + K_{mNa}} \times$$
$$\times \frac{1}{1 + 0.1245e^{-0.1VF/RT} + 0.0353e^{-VF/RT}} \tag{3.96}$$

I_{pCa} current

$$I_{pCa} = G_{pCa}\frac{Ca_i}{Ca_i + K_{pCa}} \tag{3.97}$$

I_{pK} current

$$I_{pK} = G_{pK}\frac{V - E_K}{1. + e^{(25-V)/5.98}} \tag{3.98}$$

Background currents

$$I_{bNa} = G_{bNa}(V - E_{Na}) \tag{3.99}$$

$$I_{bCa} = G_{bCa}(V - E_{Ca}) \tag{3.100}$$

Calcium dynamics

$$I_{leak} = V_{leak}(Ca_{SR} - Ca_i) \tag{3.101}$$

$$I_{up} = \frac{V_{maxup}}{1 + K_{up}^2/Ca_i^2} \tag{3.102}$$

$$I_{rel} = (a_{rel}\frac{Ca_{SR}^2}{b_{rel}^2 + Ca_{SR}^2} + c_{rel})dg \tag{3.103}$$

$$g_\infty = \begin{cases} \frac{1}{1.+(Cai/0.00035)^6} & \text{if } Ca_i <= 0.00035, \\ \frac{1}{1.+(Cai/0.00035)^{16}} & \text{if } Ca_i > 0.00035. \end{cases} \tag{3.104}$$

$$\tau_g = 2ms \tag{3.105}$$

$$\dot{g} = k\frac{g_\infty - g}{\tau_g} \tag{3.106}$$

$$k = \begin{cases} 0 & \text{if } g_\infty > g \text{ and } V > -60mV, \\ 1 & \text{otherwise.} \end{cases} \tag{3.107}$$

$$Ca_{ibufc} = \frac{Cai \times Buf_c}{Cai + K_{bufc}} \tag{3.108}$$

$$dCa_{itotal}/dt = -\frac{I_{CaL} + I_{bCa} + I_{pCa} - 2I_{NaCa}}{2V_cF} + I_{leak} - I_{up} + I_{rel} \tag{3.109}$$

$$Ca_{srbufsr} = \frac{Ca_{sr} \times Buf_{sr}}{Ca_{sr} + K_{bufsr}} \tag{3.110}$$

$$dCa_{SRtotal}/dt = \frac{V_c}{V_{sr}}(-I_{leak} + I_{up} - I_{rel}) \tag{3.111}$$

Sodium and potassium dynamics

$$dNa_i/dt = -\frac{I_{Na} + I_{bNa} + 3I_{NaK} + 3I_{NaCa}}{V_cF} \tag{3.112}$$

$$dK_i/dt = -\frac{I_{K1} + I_{to} + I_K - 2I_{NaK} + I_{pK} + I_{stim} - I_{ax}}{V_cF} \tag{3.113}$$

4

Studying the drift of scroll waves in an anisotropic LV model

4.1 Introduction

The results described in this chapter were submitted to the Biomed Research International Journal (Hindawi) [90].

Scroll waves are rotating patterns of activity that are found in excitable media of a physical, chemical and biological nature. One of the most important applications is scroll waves occurring in cardiac tissue, as they underlie the onset of dangerous cardiac arrhythmias [38]. It is extremely important to understand the

factors underlying the dynamics of scroll waves in the heart, as they determine the type of cardiac arrhythmia [38]. For example, it has been shown that the drift of scroll waves underlies the onset of polymorphic ventricular tachycardia [38].

Several factors can induce drift of scroll waves in the heart. Among them are the anisotropy of cardiac tissue and the shape of the cardiac wall. It was shown for two-dimensional spiral waves on curved anisotropic surfaces [25] that the combination of shape and anisotropy factors results in a drift at a fixed angle with respect to the gradient of the intrinsic curvature of the surface.

For scroll waves, there are additional purely three-dimensional effects which are also likely to contribute to their dynamics in the heart. In particular, it has been shown that the scroll waves drift if their filaments are curved in space and, moreover, the filament length changes monotonically [13], yielding two distinct regimes [79]. In media with positive filament tension, filament shortens and guarantees the linear stability of the filament shape, whereas in media with negative filament tension, filament length increases [13, 79]. Such dynamics of filaments are very important, as they can potentially lead to the onset of turbulence [4, 13]. Theoretical approaches have also demonstrated that the three-dimensional filament shape is an important determinant of its drift [26, 28, 50]. However, the drift of a scroll wave filament has so far only been studied in simple rectangular geometries. The only studied effect of anisotropy on three-dimensional dynamics is the possible break-up of scroll waves [29, 78].

Recently, we have developed a model of the human heart LV. This model correctly describes the shape and myofibre rotation of the LV [88, 89]. The model is formulated analytically, allowing researchers to modify the LV shape and fibre orientation in a continuous and controlled way. Using it, we can study the effects of shape, anisotropy and the thickness of the cardiac wall on various types of wave dynamics in the heart.

In this chapter, we apply our anatomical LV for the study of scroll wave dynamics. We investigate how scroll wave filament dynamics is affected by the anisotropy ratio, thickness of myocardial wall, LV shape and filament tension. We identify the

attractors of filament motion and discuss the possible mechanisms which can account for the observed phenomena.

4.2 Methods

Reaction kinetics. We used the AP model [2] for cardiac cells and a monodomain description for three-dimensional cardiac tissue:

$$\dot{u} = -ku(u-a)(u-1) - uv + \mathrm{div}(D\,\mathrm{grad}\,u), \tag{4.1}$$

$$\dot{v} = \eta(u)(8u - v), \tag{4.2}$$

where $\eta(u) = 0.1$ if $u > a$ and $\eta(u) = 1$ otherwise. To model anisotropic conduction along the cardiac myofibres, a uniaxially anisotropic diffusion tensor D is included, with Cartesian components $D^{ij}(\vec{r}) = D_a\delta^{ij} + (D_f - D_a)v^i(\vec{r})v^j(\vec{r})$, $i,j = 1,2,3$. Thereby, the diffusion is maximal and equal to D_f along the myofibre direction with unit tangent $\vec{v}$, and equal to $D_a < D_f$ in the transverse direction. At the medium boundaries, no-flux conditions $\vec{n}\cdot D\cdot \mathrm{grad}\,u = 0$ were imposed with the local normal vector $\vec{n}$.

To investigate the effect of filament tension γ_1, the value of the parameter a was varied. Note that γ_1 can be easily measured *in silico* by adding the small convection term $\vec{E}\cdot\mathrm{grad}(u)$ to Eq. (4.1) in two dimensions and measuring the spiral wave drift. For the values of $a = 0.03$ and $a = 0.08$, we respectively found $\gamma_1 = 0.29$ and $\gamma_1 = -0.49$, corresponding to the positive and negative filament tension regimes.

Geometrical model. Our anatomical LV model exhibits axisymmetry and uses a variant of spherical coordinates, where $\phi \in [0, 2\pi]$ indicates longitude and $\psi \in [0, \pi/2]$ is the downward inclination angle (latitude) with respect to the equatorial plane. The cardiac apex lies at $\psi = \pi/2$. The transmural position is parameterized by $\gamma \in [\gamma_{\mathrm{endo}}, \gamma_{\mathrm{epi}}] \subset [0,1]$. Explicitly, the curvilinear coordinates (γ, ψ, ϕ) relate

to the cylindrical coordinates (ρ, φ, z) as [88]:

$$\rho(\gamma, \psi) = (r_b + \gamma l)(\varepsilon \cos\psi + (1-\varepsilon)(1-\sin\psi)), \tag{4.3}$$

$$\varphi = \phi, \tag{4.4}$$

$$z(\gamma, \psi) = (z_b + \gamma h)(1-\sin\psi), \tag{4.5}$$

where r_b is the LV internal (endocardial) radius at the cardiac base, l is the basal ring thickness, z_b is the LV cavity depth and h is the wall thickness at the apex. The dimensionless $\varepsilon \in [0, 1]$ determines the LV sphericity between conical ($\varepsilon = 0$) and ellipsoidal ($\varepsilon = 1$). Further details of the geometry and the construction of myofibre direction can be found in [88, 89].

Parameter sets. Every time unit in our model corresponds to 20 ms, and diffusion coefficients are chosen such that one space unit in our model corresponds to 1 mm. Throughout the simulations, the following geometry parameters were kept constant: longitudinal diffusion $D_f = 12$, full LV height $z_b + h = 60$ mm and equatorial wall thickness $l = 12$ mm. We used two forms of the LV: sphere-like with $\varepsilon = 0.99$, $r_b + l = z_b + h = 60$ mm and the normal form with $\varepsilon = 0.85$, $r_b = 21$ mm.

In different simulations, we varied apical thickness between 6 and 18 mm in steps of 2 mm. The transverse diffusion D_a was chosen from $\{1.33, 4, 12\}$, such that the ratio of longitudinal and transverse wave velocities varied between $3:1$ and $1:1$.

Numerical methods. The mesh used was a rectangular lattice in the coordinates (γ, ψ, ϕ) with the size $N_\gamma \times N_\psi \times N_\phi = 13 \times 94 \times 256$. Time integration was implemented using the Euler method [89] with time step $dt = 1.666 \times 10^{-3}$ ms. Since the mesh is highly non-uniform in Cartesian coordinates, we gradually decreased the number N_ϕ of circumferential grid points when approaching the apex as detailed in [89]. Therefore, the mesh we used had non-constant distances between adjacent nodes. We numerically integrated the system until time $T = 80$ s or longer, until we saw the established dynamics of the filament.

The program was written in C language, with OpenMP parallelization, compiled with GCC. Simulations were performed on two supercomputers under Scientific Linux 6.

During the simulations, the position of the scroll wave tip was recorded by finding the intersections of the iso-surfaces $u = 0.5$, $v = 0.5$ using the method of [29]. In every layer of constant γ, a sliding average of tip position over two rotations yielded the approximate filament position. In our two-dimensional representations, the filament position is averaged over γ to obtain a mean filament position. Visualization of the results was done in Paraview, SharpEye and Matlab.

4.3 Results

We generated heart geometries of two shapes: elliptical ($\varepsilon = 0.85$), based on the measurement of the human heart [105], and spherical ($\varepsilon = 0.99$), which mimics the change of heart shape in the case of eccentric and concentric cardiac hypertrophy (see chapter 8 in [92]). We have also varied the thickness at the apex of the heart and the degree of anisotropy and excitability. We studied how each of these factors affected the dynamics of a scroll wave.

Fig. 4.1 shows typical examples of the dynamics of a scroll wave in our model. The scroll wave was initiated at a central location slightly closer to the apex of the heart (Fig. 4.1a). Depending on the geometry of our model and the anisotropy of cardiac tissue, we observed drift of the scroll wave either towards the base of the heart (Fig. 4.1b) or towards the apical region (Fig. 4.1c). In both cases, the vertical motion stabilizes at some distance from the base (apex) and the scroll wave continues a circumferential rotation.

In the next section, we discuss in detail the type of this motion and its dependency on the model geometry and tissue anisotropy.

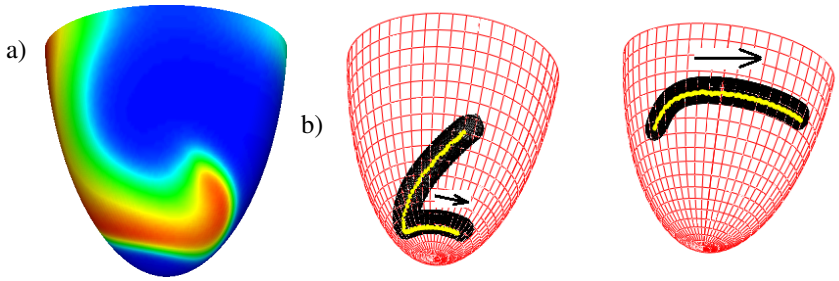

Figure 4.1: *Drift of a scroll wave in an anisotropic model of the human ventricle. a) Initial position of a scroll wave on the epicardial surface after* $t = 1\,s$ *for* $h = 10$, $\varepsilon = 0.85$, $D_a = 2$. *b) Tip trajectories (black) and filament (yellow) on the mid-myocardial surface. The arrows show the drift direction. The left panel shows the drift for the apical thickness* $h = 6\,mm$*; the right panel shows the same for* $h = 18\,mm$*. Simulations for the normal LV shape* ($\varepsilon = 0.85$)*, with anisotropy* $D_a = 4$ *and high excitability* ($a = 0.03$)*.*

4.3.1 Filament attractors and their relation to the geometry and anisotropy

We will characterize the position of the filament by a thickness-averaged (i.e. mean) position and represent it as a point in ψ, ϕ coordinates. Furthermore, since our LV model is axisymmetric, we deal with a system

$$\dot{\psi} = v_\psi(\psi), \qquad \dot{\phi} = v_\phi(\psi). \tag{4.6}$$

Therefore, the zeros of $v_\psi(\psi)$ determine vertical positions ψ_*(latitude) where filaments stabilize. In our simulations, we found that filaments after stabilization of their ψ coordinate exhibit residual circumferential drift, since generally $v_\phi(\psi_*) \neq 0$.

4.3.1.1 Drift for positive filament tension

Fig. 4.2 shows the mean filament position after stabilization for the case of positive filament tension ($a = 0.03$). In all cases, we saw that the filament stabilized at some distance from the apex (or base), after which it continued to drift circumferentially.

The vertical axis of Fig. 4.2 shows the latitude of this attractor, with $\psi = 0$ corresponding to the base of the heart and $\psi = \pi/2 \approx 1.57$, to the base of the heart. We performed simulations for a heart of a spherical shape (panel a) and normal LV form (panel b) for two initial conditions. The apical thickness h is shown on the horizontal axis. The basal thickness is always 12 mm; thus, when $h < 12$ mm, the base is thicker than the apex, and when $h > 12$ mm, the apex is thicker than the base.

General theoretical considerations predict that in the case of positive filament tension, which we have for $a = 0.03$, the filament tends to approach the region with the smallest wall thickness [13, 79].

From Fig. 4.2, we indeed see that for almost all parameter values, the filaments tend to approach the region of smaller thickness: when $h < 12$ mm, it moves towards the apex, and if $h > 12$ mm, it drifts towards the base. However, in all cases, the filament does not approach the thinnest region and stops at some distance from it. We also see a large transition zone around $h = 12$ mm. Here, the filament stops at a substantial distance from the region with the minimal thickness.

Fig. 4.2 also shows the dependency of the final position of the filament on the initial position of the scroll: the red lines show results for a scroll initially located close to the apex and blue lines for a scroll initially located close to the base. We see that in most of the cases, the final position of the scroll wave does not depend on the initial conditions; however, for $h = 16$ or 18 mm and $D = 1.33$, we have a substantial change of the position: in those cases, if the scroll is initiated close to the apex, it approaches the apex, independently on its thickness, and this result holds for both a spherical and normal shape of the LV. We performed additional studies for this case and found that scroll waves initially located at latitude $\psi < 0.7$ were drifting to the base, and for $\psi > 0.9$, they were drifting to the apex (not shown).

Now, let us try to separate the effects of different components of filament dynamics. First, we characterize the effect of the shape of the ventricle on the final position of the filament. If we compare the final position of the filament for both

geometries, we find that in a spherical shape, the filament is closer to the region of smaller thickness: for example, for $h = 16$ mm for all anisotropy ratios, the filament for a spherical LV shape is located closer to the base than for a normal shape ($\psi = 0.35$ vs. $\psi = 0.4$), and for $h = 6$ mm, the filament for the spherical LV shape is located closer to the apex than for a normal shape ($\psi = 1.45$ vs. $\psi = 1.2$). We also see that the transition from the apical to basal location was more gradual for the normal shape than for the spherical shape.

Secondly, let us consider the effect of anisotropy. We see that for both shapes and all anisotropy ratios, an increase in the anisotropy ratio results in shifts of the filament towards the apex. Once again, the effect is more substantial for a normal shape, especially for 8 mm$\leq h \leq 12$ mm. For a spherical shape, we also see a shift of the position to the apex, but the effect here is minimal. Thus, anisotropy in our case tends to move the filament towards the apex.

Next, we characterize the trajectory of a scroll wave after approaching the attractor. In all cases, the scroll wave stabilizes at some latitude $\psi = \psi_*$ and then performs a rotational motion around the axisymmetric LV. Fig. 4.3 shows the velocity of this motion for a spherical (Fig. 4.3 a) and normal shape (Fig. 4.3 b) with negative velocity accounting for a counterclockwise direction. Note that in all simulations, the rotation of scroll wave itself was always counterclockwise (as shown in Fig. 4.1), and if the rotation direction of the scroll were changed, all velocities shown in Fig. 4.3 would also change their signs. We see that for a thick apex $h > 14$ mm (i.e. when the scroll approaches the base of the heart) in both cases, the rotation is counterclockwise and its velocity increases with the increase in the anisotropy. For a thin apex $h < 8$ mm (i.e. when the scroll approaches the apex of the heart), the velocity is slower and it exhibits a more complex dependency on the anisotropy. For the normal shape, we see that in the isotropic case, the scroll wave rotates clockwise around the LV. When the anisotropy increases, the velocity of motion decreases and becomes negative for strong anisotropy; that is, the drift motion of a spiral wave around the LV changes to counterclockwise. For the spherical

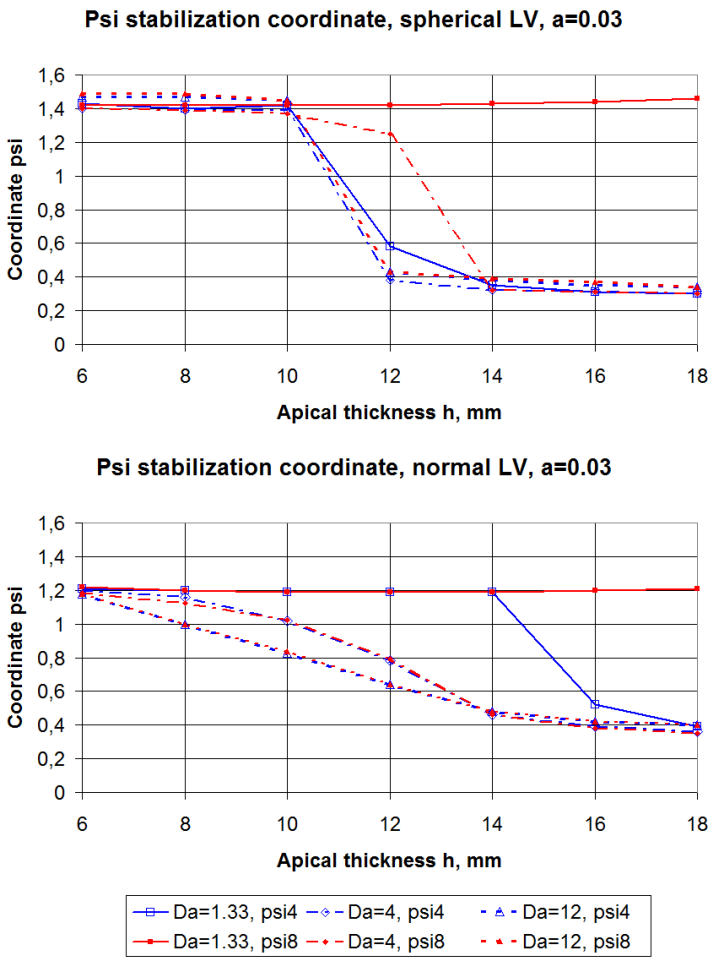

Figure 4.2: *Final position ψ_* of the filament for the spherical and normal LV shape in the case of positive filament tension ($a = 0.03$). The blue line shows the results of simulations for initial scroll location at the centre of the LV and the red line for the initial location close to the apex. The X-axis shows the apical thickness h, the Y-axis is the ψ coordinate. The LV base has $\psi = 0$, the apex has $\psi = \pi/2$. Different lines styles correspond to different anisotropy ratios.*

shape in most of the cases, rotation is always clockwise and the dependency on the anisotropy is much smaller.

4.3.1.2 Drift for negative filament tension

Fig. 4.4 shows the mean filament position after stabilization for the case of negative filament tension ($a = 0.08$). General theoretical considerations predict that in the case of negative filament tension, the length of the filament grows and it may lead to the onset of a spatio-temporal chaos [4, 13].

From Fig. 4.4, we see that we almost never obtain a break-up of the scrolls for these parameter values, and in most cases, the filament stabilizes either at the apex or base. Let us consider first the results for the spherical geometry. We see that the filament drifts to the regions with the thicker wall, and the situation here is somewhat opposite from that for Fig. 4.2. Indeed, for the apical thickness $h > 14\,\text{mm}$, the scroll for most of the cases approaches the apex, and for $h > 8\,\text{mm}$, it most often approaches the base. However, we note a substantial dependency on the initial conditions. If the initial position of the scroll wave is close to the apex (red lines), they are more likely to drift to the apex. If, however, the initial scroll wave is closer to the base (blue lines), the filament may drift to the base even if the base is thinner (see e.g. the case $h = 14, D_a = 12$, blue line).

Secondly, for the normal shape, we see almost no dependency on the LV thickness. For most parameter values, the scroll wave approaches the apex. However, for $D_a = 12$ (blue line), it stays at the base for all values of h. It is also difficult to find a clear dependency of the attractor location on the shape of the ventricle. Overall, in most of the cases shown in Fig. 4.4, the scroll wave tends to approach the apex. However, in few cases, as for example $h = 18, D_a = 12$, we observe that in the spherical geometry, the filaments tend to move towards the apex, while for the normal geometry, it approaches the base (blue line). As we have never seen the opposite situation, we can conclude that for a spherical shape, there is a slight preference for the scroll wave to move to the apex compared to the normal shape.

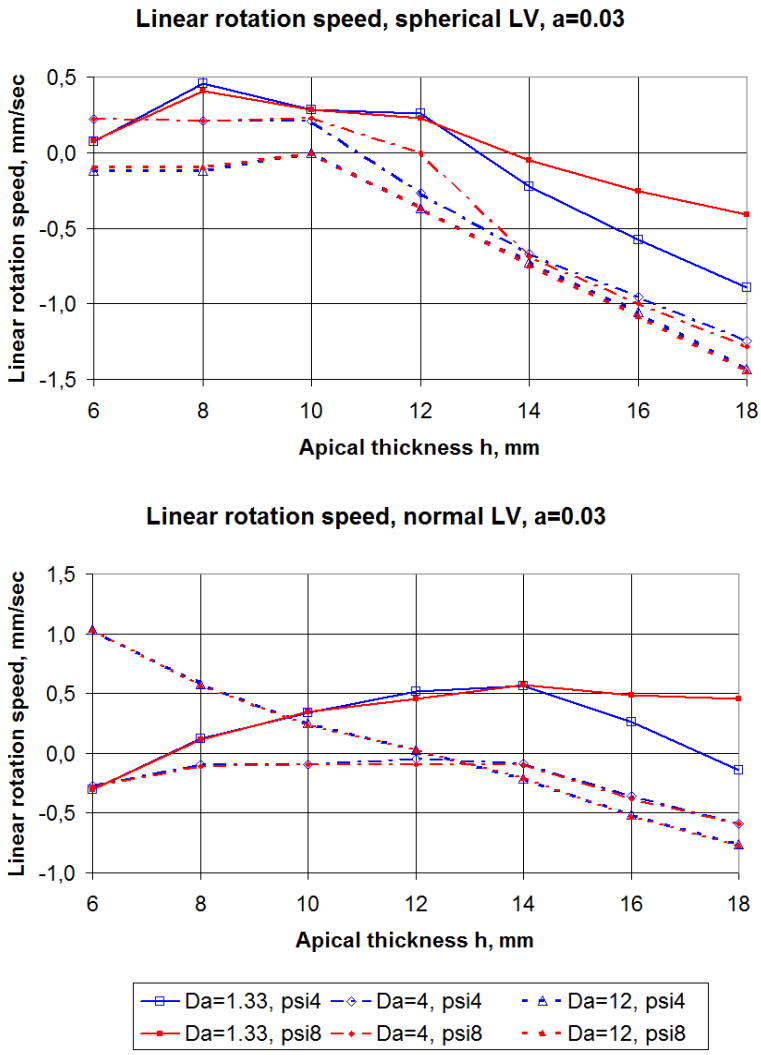

Figure 4.3: *Residual circumferential speed of the drifting filament after stabilization at the attractors $\psi = \psi_*$ shown in Fig. 4.2 for the cases of the spherical (top) and the normal LV shape (bottom). The X-axis is the apical thickness h, the Y-axis is the speed, mm/sec. Different lines correspond to different anisotropy ratios.*

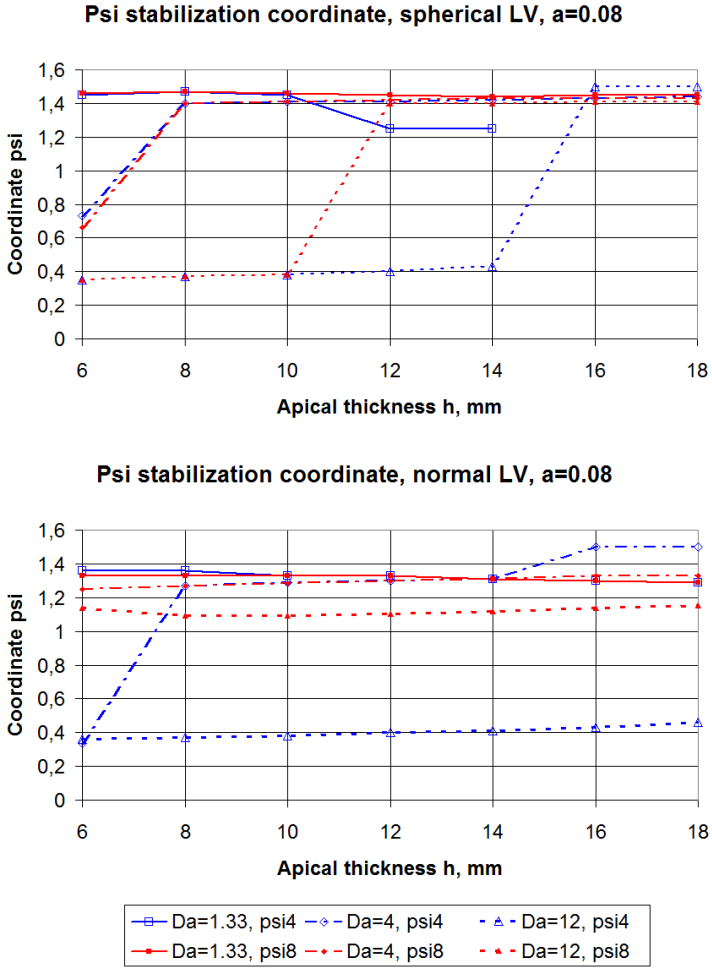

Figure 4.4: *Final position ψ_* of the filament for the spherical LV shape (a) and normal LV shape (b) in the case of negative filament tension ($a = 0.08$). The blue line shows the results of simulations for initial scroll location at the centre of the LV and the red line for the initial location close to the apex. The X-axis shows the apical thickness h, and the Y-axis is the ψ coordinate. The LV base has $\psi = 0$, and the apex has $\psi = \pi/2$. The different line styles correspond to different anisotropy ratios.*

We, however, observe a clear effect of anisotropy. In all cases, an increase in the anisotropy ratio resulted in a shift of the attractor to the apex. Thus, as for the positive filament tension, increased anisotropy tends to push the filament towards the apex.

The velocities of a scroll wave after approaching the attractor for negative filament tension shown in Fig. 4.5 substantially differ from the case of the positive tension. We see that velocities here are 50-100 time smaller; that is, the circumferential motion of the filament is almost absent. In most cases, the direction of this motion is counterclockwise.

We have also observed filament break-up for large anisotropy ratio and large apical thickness; that is, $D_a = 1.33$ and $h = 16$ or 18 mm. (For these parameters, data are absent in Fig. 4.4a.) A typical excitation pattern is shown in Fig. 4.6. We see a break-up pattern, which in this case comprises 4-8 wavelets on the surface of the LV. In some cases, the break-up was transient.

4.3.2 Mechanisms of filament dynamics

To understand the mechanisms of the observed phenomena, we performed a series of two-dimensional simulations in which we studied the drift of a spiral wave on a two-dimensional surface for the following cases: (a) a paraboloidal surface $z = (x^2+y^2)/120$ mm close to the endocardial shape of the normal model without anisotropy, (b) a two-dimensional square resembling the anisotropy of the mid-wall endocardium, and (c) the paraboloidal surface of case (a) with the anisotropy of case (b). The results of these simulations are shown in Fig. 4.7. We see that for the case of $a = 0.03$, the spiral is attracted to the apex for all three situations, and its characteristic velocity of motion at a distance $\rho = 45$ mm from the cardiac apex for the isotropic paraboloid is $v_\rho = -1$ mm/s, $\rho v_\varphi = -1$ mm/s and $v_\rho = -0.3$ mm/s, and $\rho v_\varphi = -0.2$ mm/s for an anisotropic plane with circumferential fibres.

For $a = 0.08$, both surface shape and anisotropy repel the spiral from the apex, and its characteristic velocity of motion at $\rho = 70$ mm for the isotropic paraboloid

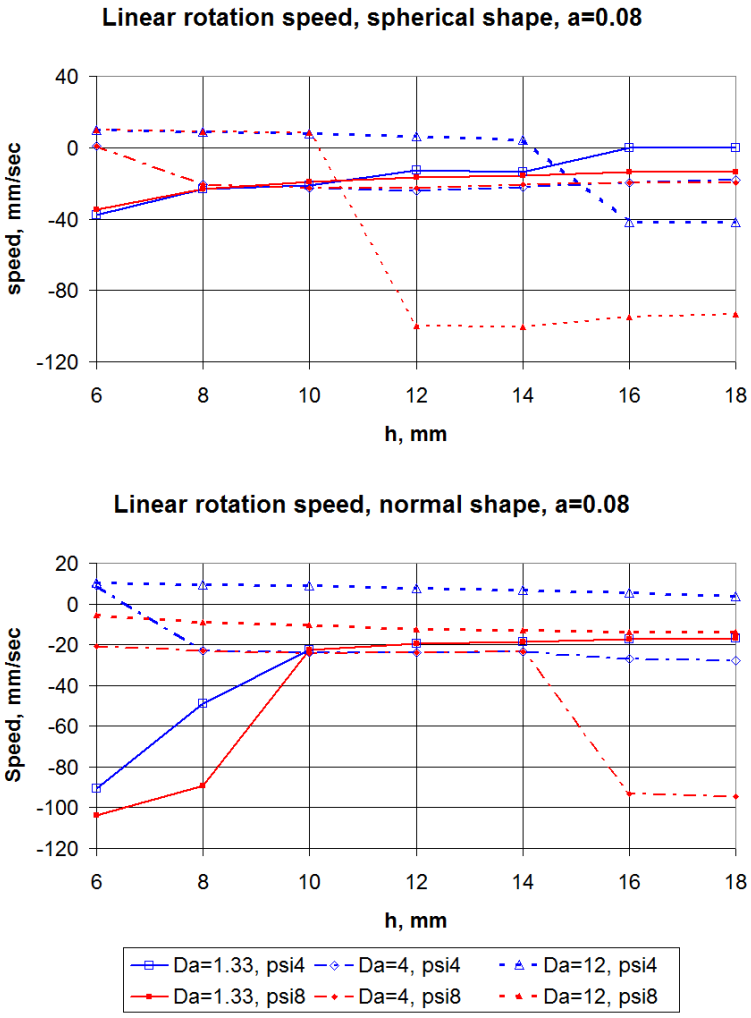

Figure 4.5: *Residual circumferential speed of the drifting filament after stabilization at the attractors $\psi = \psi_*$ (see Fig. 4.4) for the cases of the spherical (top) and the normal LV shape (bottom). The X-axis is the apical thickness h, and the Y-axis is the speed, mm/sec. Different lines correspond to different anisotropy ratios.*

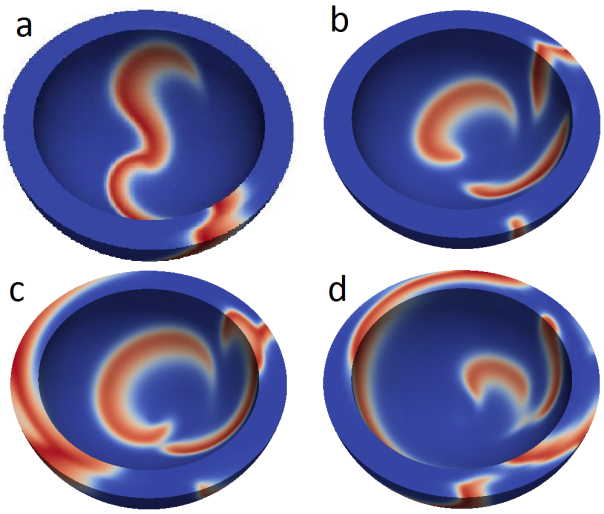

Figure 4.6: *Break-up of a scroll wave due to negative filament tension. Simulations are for* $h = 18\,mm$, $\varepsilon = 0.99$, $D_a = 1.33$, *and* $a = 0.08$. *Snapshots times are (a) 100 ms, (b) 1800 ms, (c) 1880 ms, (d) 1940 ms.*

is $v_\rho = 2$ mm/s, and $\rho v_\varphi = -4$ mm/s and $v_\rho = 2$ mm/s, $\rho v_\varphi = -3$ mm/s for an anisotropic plane with circumferential fibres. Let us consider how these results can be used to explain the observed filament dynamics.

The drift of the filaments studied in the previous section is a combination of three factors which can potentially contribute to the filament dynamics: the thickness of the medium, the anisotropy and the shape of the LV.

First, we consider the effect of wall thickness. From [13], it is known that filaments with positive tension γ_1 ($a = 0.03$ in our case) tend to decrease their length. In such a case, the filaments are expected to stabilize in a region where a local minimum of wall thickness is reached. To compute wall thickness for the given parameters of the shape, we took $10N_\psi = 940$ points on the epicardial and endocardial surfaces. For each ψ_1 value on the endocardium, we found the closest point on the epicardium, occurring at latitude ψ_2. The Euclidean distance between these two points was then logged as the wall thickness at latitude $\psi = (\psi_1 + \psi_2)/2$.

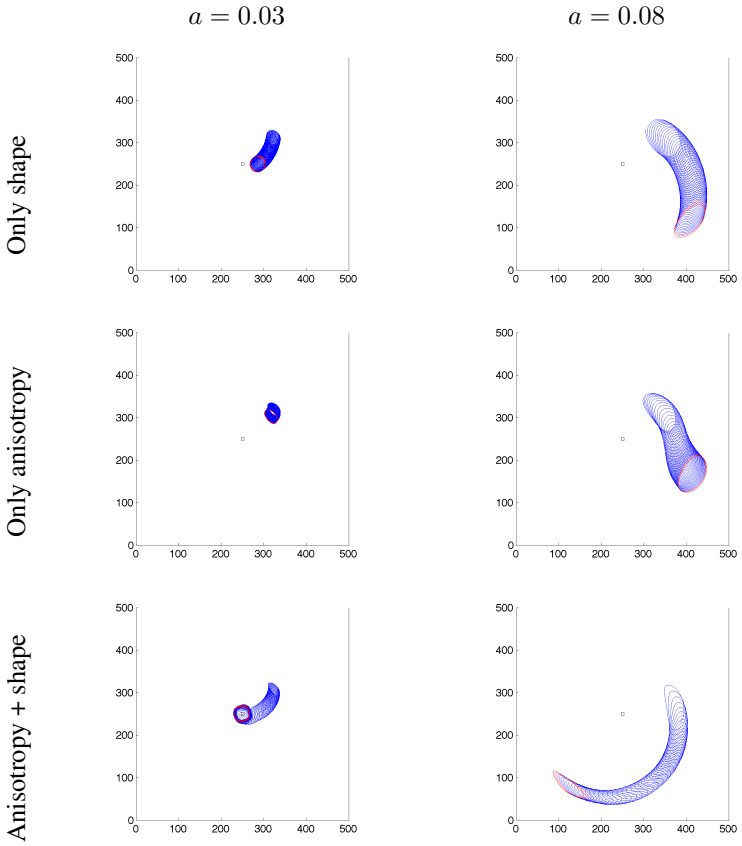

Figure 4.7: *Spiral wave drift on two-dimensional surfaces of different shape and anisotropy. Simulations in the Aliev–Panfilov model with parameter* $a = 0.03$ *(left column) and* $a = 0.08$ *(right column). Top row represents the results for the paraboloidal shape* $z = (x^2 + y^2)/120\,mm$*. The middle row shows drift on an anisotropic plane with circumferential fibres:* $\vec{e_f} = \vec{e_\varphi}$*,* $D_f = 12, D_a = 4$*. The bottom row combines circumferential fibres with paraboloid shape. Simulations run on a domain of size* $200\,mm$ *for* $30\,s$*. The red line indicates tip positions close to the end of the simulation. Numerical methods are described in [25].*

Fig. 4.8 shows the resulting wall thickness as a function of latitude ψ, together with the stable loci $\psi = \psi_*$ of filaments for different anisotropy ratios.

For the spherical LV model ($\varepsilon = 0.99$, panel a), wall thickness is monotonous and exhibits a minimum at the apex when $h < 12\,\text{mm}$ and at the base when $h > 12\,\text{mm}$. In the isotropic case, the final filament state comes close to these expected values. For the normal LV shape ($\varepsilon = 0.85$), however, wall thickness exhibits a local minimum in the mid-wall region when $h > 6\,\text{mm}$. Therefore, if the filament moves to the position with minimal length, it is expected to equilibrate at moderate values of latitude ψ. The numerical results in Fig. 4.8b and 4.4b confirm this view, since we observe that when h is increased, the stable filament position gradually changes from basal to apical.

a) b)

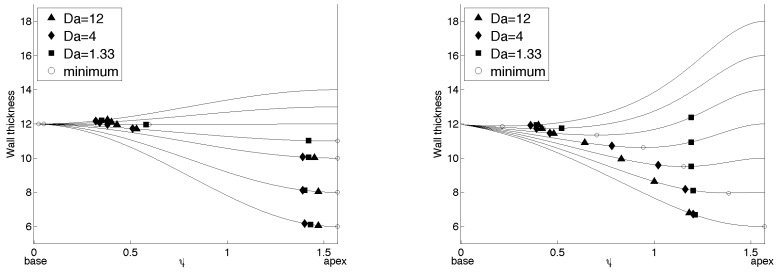

Figure 4.8: *Stable filament positions ψ_* in the case of positive filament tension ($a = 0.03$) compared to LV wall thickness, for spherical LV shape (panel a) and normal LV shape (panel b). Results are shown for one initial condition; different symbols indicate different anisotropy ratios. Open circles denote loci of minimal wall thickness.*

Next, we turn to the effect of LV shape and anisotropy. It was previously shown [25] that on two-dimensional surfaces (i.e. thin layers with constant thickness), spiral waves drift according to the gradient of the Ricci curvature, which encompasses both anisotropy and shape. With finite thickness, it can be hypothesized that scroll waves behave like a spiral wave in each layer of constant depth

and are therefore sensitive to the anisotropy and curvature in these layers. From our two-dimensional observations in Fig. 4.7, we know that for $a = 0.03$, positive curvature attracts spiral waves. Moreover, when circumferential fibres are present in the LV wall, they effectively reduce the circumference of the LV at a fixed latitude ψ if distance is measured according to the arrival time of the excitation waves [127, 130]. Therefore, increasing the anisotropy ratio of circumferential fibres makes a spherical or ellipsoidal shape effectively more elongated. Since such a shape has the increased Ricci curvature close to the apex, it has an attracting effect on spiral waves for $a = 0.03$, based on our two-dimensional observations in Fig. 4.7. In conclusion, we expect that circumferential fibres around the apex will push the spiral towards the apex. In Fig. 4.8b, we see that for an increasing anisotropy ratio, the equilibrium position for filaments indeed shifts closer to the apex.

Now let us consider the case of the negative filament tension. The absence of a break-up for the negative filament tension can be explained by the dependency of this effect on the thickness of the tissue. In [3], it was shown that if the thickness of cardiac tissue is small, the break-up of a scroll wave due to negative filament tension disappears. This phenomenon was further studied in [23], where it was shown that filament rigidity increases the effective filament tension in thin media. Although the study [3] uses a different model for cardiac tissue (i.e. the LuoRudy-1 ionic model), it shows that the critical thickness for the onset of instability there is around 1 cm. In our case, we see a break-up only in the case of a spherical LV shape and when its maximal thickness is above 14 mm. Given the big differences between the models used in our simulations, this value can be considered reasonably close to that obtained in that study [3].

When the break-up is absent, we observe a drift of transmural filaments. However, in most of the cases, its final position is at the cardiac apex, and for stronger anisotropy, this tendency to go to the apex becomes stronger. Those results are opposite to the results of our two-dimensional simulations, which indicate that in this case, both geometry and anisotropy repel two-dimensional spiral waves from

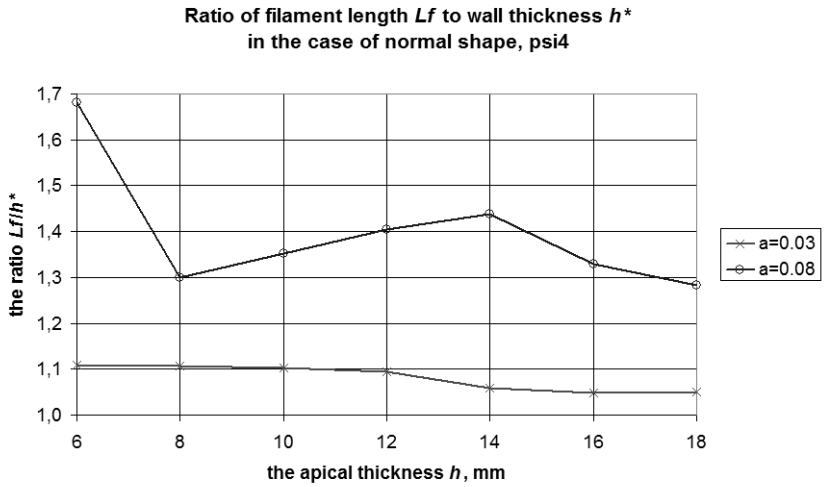

Figure 4.9: *Ratio of filament length L_f and LV wall thickness $h*$ at the attractor $\psi = \psi_*$ for the normal LV shape. Simulations for positive ($a = 0.03$, red line) and negative ($a = 0.08$, blue line) filament tension are shown.*

the apex. This discrepancy can be understood by the observation that for moderate wall thickness and negative filament tension, filaments will 'buckle' and deform into an S-shape, after which they undergo precession [23]. We noted in our simulations that for $a = 0.08$, the (Euclidean) length of the filament is always bigger than the wall thickness (see Fig. 4.9), and a visual inspection of the end-state shows that the resulting filament is buckled (see Fig. 4.10). During one rotation period (depicted in Fig. 4.10b), the vector connecting the filament endpoints at epicardial and endocardial boundaries also performs a full rotation, albeit in the opposite sense. Therefore, the precession of buckling is phase-locked to scroll wave rotation. This, however, does not explain the tendency of filaments towards the apex. Another factor may be the full three-dimensional anisotropy effects, which deserve further study.

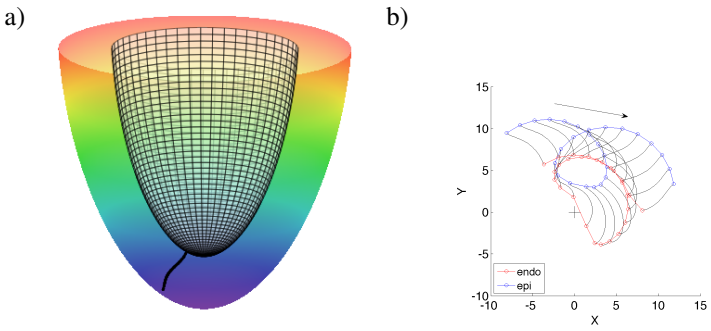

Figure 4.10: *Buckled filament state after 60 s for* $h = 12\,mm$, $\varepsilon = 0.85$, *and* $D_a = 4$. *a) Three-dimensional view of the buckled filament. b) Top view of the endocardial and epicardial tip trajectories between 62.16 s and 62.84 sec (3108 and 3142 time units of the AP model). The arrow indicates drift direction, and the cross marks the cardiac apex.*

4.4 Discussion

In this chapter, we have presented results on the drift of scroll wave filaments in an anatomical model of human ventricles and have studied the effect of shape, thickness and anisotropy of the ventricle on the drift pattern. We found that the results are substantially affected by the filament tension of the scroll wave.

In the case of the positive filament tension, one of the main determinants of the drift was the thickness of the myocardial wall and the filament tended to drift to the region of minimal thickness. However, in all cases, it never arrived to the point of minimal thickness and rotated at some small distance from it.

Another important determinant of filament drift was the anisotropy of the tissue. Its main effect in our simulations was the attraction of the scroll wave to the apex. The LV shape had a small effect on the results in terms of the direction of the drift. However, it affected the location of the attractor, especially when the gradient in the thickness was not large.

As cardiac tissue has a high excitability in normal conditions, one would expect that in normal conditions, the filament would be located close to the region of minimal thickness with a slight preference towards the apex, due to anisotropy

effects. This information might be important for identifying sources of arrhythmias in the heart, with applications in the planning of successive clinical intervention.

We have also studied the case of negative filament tension. In that case, filaments generally behave chaotically, and this normally results in the break-up of scroll waves [4, 13]. In our case, we find that such a break-up can only occur in a small parameter range. In most other cases, the filament was drifting to a stable attractor, and its location was close to the region of maximal thickness in a few cases. However, we observed that scroll waves were much more likely to approach the apex of the ventricle than its base. We again found that the anisotropy of the heart substantially affects the motion by attracting the scroll to the apex; this effect cannot be explained by simple two-dimensional simulations and theory. The LV shape also had a small affect on the scroll wave motion, but for the normal shape, we saw more motion to the apex than for a spherical shape. Thus, in this case, we can say that the elliptic shape induced some attraction force towards the apex of the heart.

The mechanisms underlying the observed phenomena in the regime of positive filament tension can be partially explained by the existing theories of filament dynamics. As such filaments strive to minimize their length, they move to regions of minimal wall thickness. However, we found in our simulations that even in the isotropic case, the filaments did not exactly reach that minimum. Possible disturbing factors are filament twist, curvature of the endocardial and epicardial boundaries, and discretization effects. In two-dimensional simulations, it was seen that spiral waves in the high excitability regime are attracted to regions of positive curvature, such as the cardiac apex, in contrast to a previous study in Barkley's model [25]. Since positive curvature is amplified by the anisotropy of circumferential myofibres, we understand that an increased anisotropy ratio pushes the filaments closer to the cardiac apex.

In the regime of negative tension, the wall thickness proved in most cases to be insufficient for the development of a full three-dimensional break-up. Instead, we identified buckled filaments which also equilibrate at a given latitude, due to the

axial symmetry of our LV model. A further theoretical consideration of the effects of shape and anisotropy on scroll wave dynamics would be non-trivial. Possible ways to approach this problem are to consider shapes with a small thickness and to use averaging methods as in [14]. For thick shapes, one can use the equations of filament dynamics in a general anisotropic medium derived in [123]. However, incorporating the effect of curved domain boundaries on the filament and reconciling those with bulk motion remains a difficult task.

We performed our simulations using the AP model, which provides a simplified description of cardiac tissue. Two-variable models allow researchers to easily obtain various regimes of filament tension, and they are much more efficient for large-scale numerical simulations. Therefore, two-variable models of cardiac tissue are widely used in studies of two-dimensional and three-dimensional dynamics of spiral waves in the heart (see e.g. [74]). The next logical step would be to extend these simulations to an ionic model for human cardiac tissue [36, 69, 108, 109] and to find out how the present results are affected.

We have studied only filaments extending from the epicardial to the endocardial surface. It would also be interesting to study the dynamics of the intramural filaments. Such filaments can occur during the normal excitation of cardiac tissue and may have a complex shape and therefore complex dynamics [1].

In this chapter, we have studied the motion of scroll waves in a homogeneous model of cardiac tissue. It was shown that the heterogeneity of cardiac tissue substantially affects the motion of vortices and their dynamics [81, 96]. The presence of heterogeneity can shift the locations of found attractors and can also result in the onset of new vortices [81]. It would be interesting to study the effect of the transmural heterogeneity and apex base heterogeneity [7, 19] on the results obtained in this chapter. In addition, the presence of the Purkinje network and pectinate muscles may also affect filament dynamics and should be studied in the future.

5

Non-axisymmetrical model of the left ventricle shape and anisotropy

5.1 Introduction

The results described in this chapter have been published in [87].

In chapter 2, an axisymmetrical model of the truncated LV (only below the equator) was described. Here we generalize that model. The real LVs of different species can have both an axisymmetrical and substantially nonsymmetrical form.

For example, canine LVs can for convenience be divided into two parts, prominent free wall and interventricular septum (IVS), which significantly juts into the upper part of LV cavity. We construct a non-axisymmetrical model of the LV. In our model, both anatomy and fibre direction field are defined analytically. We calculate fibre slope angles in a local coordinate system and compare them with in vitro experimental data on human and canine hearts.

5.2 Construction of the generalized LV model

In order to define the LV form, we use a special coordinate system (γ, ψ, ϕ), where the variable $\gamma \in [\gamma_0, \gamma_1] \subseteq [0, 1]$ corresponds with position of a point in the LV wall layer, $\gamma = \gamma_0$ is the endocardium, $\gamma = \gamma_1$ is the epicardium, $\psi \in [0, \pi/2]$ is analog of latitude, $\psi = 0$ is the upper plane part of the LV model (fibrous ring and valve zone), $\psi = \pi/2$ is the LV apex, and $\phi \in [0, 2\pi)$ is analog of longitude.

We can transform the special coordinates into cylindrical ones (ρ, ϕ, z) using the formulae (Fig. 5.1):

$$\begin{aligned}\rho(\psi, \gamma, \phi) = \rho_{inmer}(\psi,\ r_0(\phi) + (\gamma - 1)d_0(\phi),\ r_e(\phi) + (\gamma - 1)d_e(\phi),\\ l_0(\phi) + \gamma(l_1(\phi) - l_0(\phi)),\ p(\phi)),\end{aligned} \tag{5.1}$$

$$z(\psi, \gamma) = Z - (Z + h(\gamma - 1)) \sin\psi + \Delta z, \tag{5.2}$$

$$\rho_{inmer}(\psi, r_0, r_e, l, p) = \begin{cases} r_e - (r_e - r_0) \cdot \left(1 - \frac{\psi}{l}\right)^p, & \text{if } \psi < l, \\ r_e \cdot \left[1 - \left(\frac{\psi - l}{\pi/2 - l}\right)^p\right], & \text{otherwise,} \end{cases} \tag{5.3}$$

where $\rho_{inmer}(\psi, r_0, r_e, l, p)$ is coordinate ρ of a point with coordinate ψ in the LV wall, if the LV base has coordinates $\rho = r_0$, $\psi = 0$, the equator has coordinates $\rho = r_e$, $\psi = 0$; $p(\phi) > 1$; $r_{0,e}(\phi)$ is the LV epicardial radius at the base, equator; $d_{0,e}(\phi)$ is the LV epicardial wall thickness at the base, equator; $l_{0,1}(\phi)$ is the latitude ψ of equator at the endocardium, epicardium; Z is the LV height; h is the LV wall thickness at the apex; index i means input parameter,

$$r_0 = r_0^i + \frac{d_0^i(1 - \gamma_1)}{\gamma_1 - \gamma_0},$$

$$d_0 = \frac{d_0^i}{\gamma_1 - \gamma_0},$$

$$r_e = r_e^i + \frac{d_e^i(1-\gamma_1)}{\gamma_1 - \gamma_0},$$

$$d_e = \frac{d_e^i}{\gamma_1 - \gamma_0},$$

$$l_0 = \frac{\gamma_1 l_0^i - \gamma_0 l_1^i}{\gamma_1 - \gamma_0},$$

$$l_1 = \frac{l_1^i(1-\gamma_0) + l_0^i(\gamma_1 - 1)}{\gamma_1 - \gamma_0},$$

$$h = \frac{h^i}{\gamma_1 - \gamma_0},$$

$$\Delta z = \frac{h^i(\gamma_1 - 1)}{\gamma_1 - \gamma_0},$$

$$Z = Z^i - \Delta z.$$

5.2.1 Spiral surfaces

The model LV myocardium consists of fibres that lie on spiral surfaces (SS). An SS has the following equation in the special coordinates:

$$\phi(\gamma, \phi_0, \phi_{\max}) = \phi_0 + \gamma\phi_{\max}, \tag{5.4}$$

where $\phi_{\max}$ is the SS twist angle (the same for all SS),

$$\phi_{\max} = \frac{\phi_{\max}^i}{\gamma_1 - \gamma_0},$$

and different SSs have different values of $\phi_0 \in [0, 2\pi)$.

An SS equation in the cylindrical coordinates (see (5.1), (5.2)):

$$\rho_{sp}(\psi, \phi, \phi_0) = \rho\left(\psi, \frac{\phi - \phi_0}{\phi_{\max}}, \phi\right), \tag{5.5}$$

$$z_{sp}(\psi, \phi, \phi_0) = z\left(\psi, \frac{\phi - \phi_0}{\phi_{\max}}\right). \tag{5.6}$$

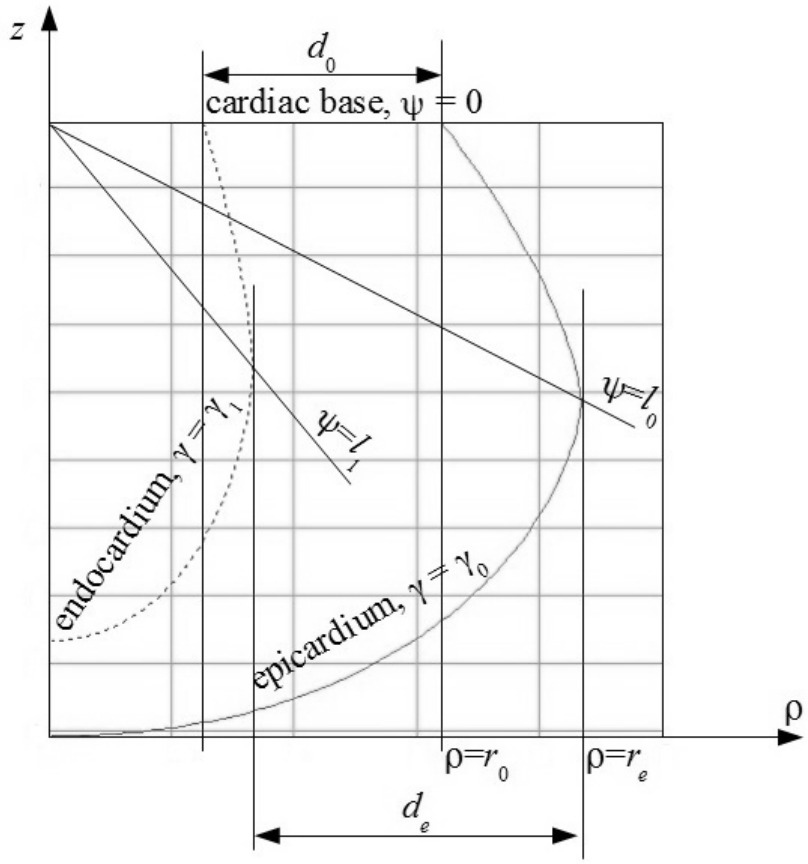

Figure 5.1: *A meridional section of the model*

5.2.2 Filling a spiral surface by fibres

Following J. Pettigrew's theoretical hypothesis [84] and its practical realization [88], we modelled myocardial fibres as images of chords $Y = \text{const}$, $Y \in [0, 1)$ of semicircumference $\mathrm{P} = 1$, $\Phi \in [0, \pi]$ (the chords are parallel to the diameter) on the SS (Fig. 2.1). Each chord was parameterized by the polar angle $\Phi \in [\Phi_0, \Phi_1]$, where $\Phi_0 = \arcsin Y$ and $\Phi_1 = \pi - \arcsin Y$. Mapping of a

chord point (P, Φ) to a SS point is defined by the formulae (Fig. 5.2):

$$\gamma(\Phi) = \Phi/\pi,$$
$$\psi(\mathrm{P}) = (1 - \mathrm{P}) \cdot \frac{\pi}{2}.$$

For example, the image of the semicircle diameter is a fibre that begins on the epicardium, desends to the apex $(\Phi = \pi/2)$, then ascends and ends on the endocardium. Images of shorter chords are situated closer to the LV top and have lesser length.

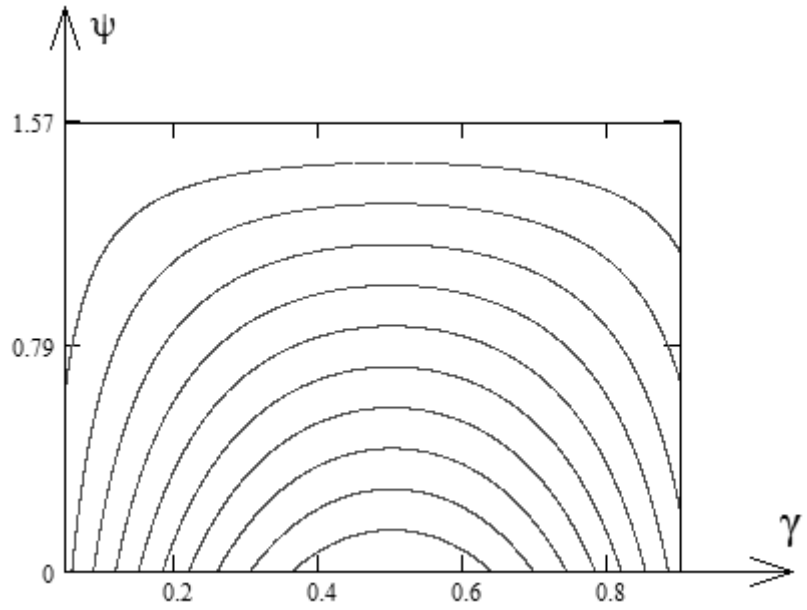

Figure 5.2: *Images of the semicircle chords in* (γ, ψ) *coordinates*

5.2.3 Calculation of the fibre direction in a point

Let us consider a point that has cylindrical coordinates (ρ, ϕ, z). To calculate a fibre direction vector in this point, the following is needed:

1. Use formulae (5.1)–(5.3) to numerically find the special coordinates γ and ψ of the point. This problem can be reduced to solving one algebraic equation with one unknown quantity γ, as this needs to express $\psi(\gamma, z)$ in the formula (5.2) and substitute this expression in (5.1) and (5.3).

2. Find Cartesian coordinates of the point $(x = \rho\cos\phi,\, y = \rho\sin\phi,\, z)$.

3. Differentiate (numerically or analytically) the function $\rho(\psi, \gamma, \phi)$ in all arguments and obtain three partial derivatives ρ_ψ, ρ_γ, ρ_ϕ.

4. The non-normalized vector of fibre direction is:

$$x = \frac{\sin(\pi\gamma)}{\pi - 2\psi} \cdot (y\phi_{\max} - (\rho_\gamma + \rho_\phi\phi_{\max}) \cdot \cos\phi) - \cos\psi \cdot \rho_\psi \cdot \frac{\pi}{2} \cdot \cos(\pi\gamma),$$

$$y = \frac{\sin(\pi\gamma)}{2\psi - \pi} \cdot (x\phi_{\max} + (\rho_\gamma + \rho_\phi\phi_{\max}) \cdot \sin\phi) - \sin\psi \cdot \rho_\psi \cdot \frac{\pi}{2} \cdot \cos(\pi\gamma),$$

$$z = \frac{h}{\pi - 2\psi} \cdot \sin(\pi\gamma)\sin\psi + (Z - h\gamma)\cos\psi \cdot \frac{\pi}{2} \cdot \cos(\pi\gamma).$$

5.2.4 The LV form fitting

We fitted a model LV form to one real LV of a dog and of a human based on DT-MRI data, which are freely accessible online at

`http://gforge.icm.jhu.edu/gf/project/`
`dtmri_data_sets/docman/`

First, we found the LV axis Oz, then we sectioned the LV by $N = 20$ (for canine heart) or $N = 24$ (for human heart) meridional half-planes $\phi_i = 2\pi i/N$, $i = 0, 1 \ldots N - 1$, passing this axis, and we manually found the needed parameter values, $r_0, r_e, d_0, d_e, l_0, l_1, p$ in each section. After that, we found functions $r_0(\phi)$, $r_e(\phi)$, $d_0(\phi)$, $d_e(\phi)$, $l_0(\phi)$, $l_1(\phi)$ and $p(\phi)$ by means of linear interpolation.

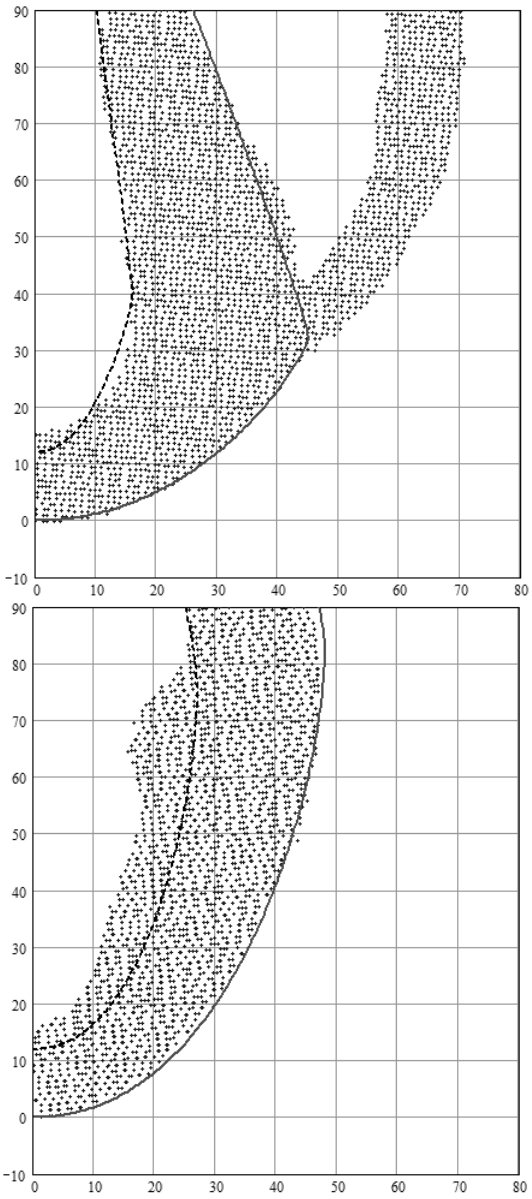

Figure 5.3: *Vertical (meridional) sections of the IVS (on the left) and LV free wall (on the right) of a canine heart. The points are DT-MRI data, the solid line is the model epicardium, the dashed line is the model endocardium. On the left panel: LV cavity is to the left and the RV cavity and free wall are to the right of the IVS.*

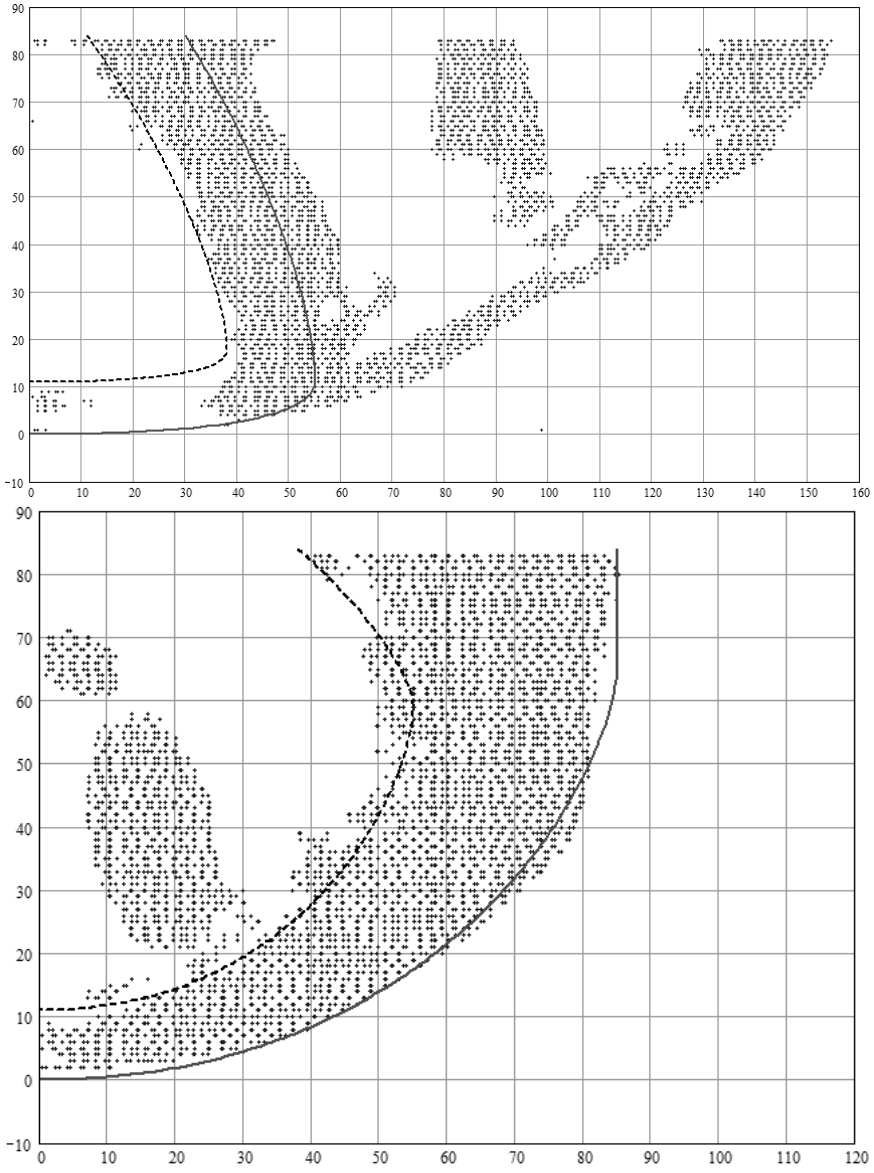

Figure 5.4: *Vertical (meridional) sections of the IVS (on top) and LV free wall (below) of a human heart. The points are DT-MRI data, the solid line is the model epicardium and the dashed line is the model endocardium. On top of the panel, there are papillar muscle in the RV cavity (vertical one,* $\rho = 80 \ldots 100$ *mm) and a RV free wall (inclined).*

5.3 Methods for the model and experiment comparison

We compared the theoretical model and experimental data by comparing the fibre slope angles that intersect normals to an epicardium meridional section. These methods were described in [105] and it has the following steps.

To compare angles along a normal, one needs to specify a point A on the epicardium. Let its special coordinates be $\gamma = \gamma_1$, $\psi = \psi_A$ and $\phi = \phi_A$. Let us consider a corresponding meridional section $\phi = \phi_A$ of the model, semiplane Π. Let us construct a normal to the epicardial section by this semiplane and find its intersection with the endocardium or the base, a point B. On the segment AB, we set k unidistant points, including its ends, so that $A = A_1, A_2, \ldots, A_k = B$. The position of a point A_i on the segment AB is defined by the variable

$$t_i = \frac{A_i B}{AB}$$

(for the endocardium $t = 0$, for the epicardium $t = 1$). Through every point $A_i(\gamma_i, \psi_i, \phi_A)$ we have to draw an SS. Problem of finding such an SS reduces to solving a system of two algebraic equations with two unknown quantities ψ and ϕ_0:

$$\begin{cases} \rho_{sp}(\psi, \phi^*, \phi_0) = \rho^*, \\ z_{sp}(\psi, \phi^*, \phi_0) = z^*, \end{cases}$$

where (ρ^*, ϕ^*, z^*) are cylindical coordinates of point A_i. This problem is equivalent to conversion of cylindrical coordinates into special ones, i.e. solving system

$$\begin{cases} \rho(\psi, \gamma, \phi^*) = \rho^*, \\ z(\psi, \gamma) = z^* \end{cases}$$

by ψ and γ. One can express ψ from the second equation of this system:

$$\psi(z_i, \gamma) = \arcsin\left(\frac{Z - z^* + \Delta z}{Z + h(\gamma - 1)}\right)$$

and substitute this expression to the first equation. Then the problem reduces to solving one nonlinear equation

$$\rho(\psi(z^*, \gamma), \gamma, \phi^*) = \rho^*$$

with one unknown quantity γ on segment $[\gamma_0, \gamma_1]$, which can easily be done, for example, by the method of tangents.

Strictly speaking, there can be no points from the tomogram exactly on semiplane Π; therefore, we selected points lying no further than $\Delta = 1$ mm from the straight line AB and inside the dihedral angle $|\phi - \phi^*| \leq \Delta_\phi = 0.1 = 5.7°$.

In his work [105], Streeter proposed specifying fibre direction using a local coordinate system (u, v, w) and two angles, "true fibre angle" α and "helix angle" α_1 (these angles are sufficient for specifying a fibre direction in a point). The axis u is a normal to the epicardium pointed from the LV; w is a meridian, i.e. an epicardial tangent lying in a meridional semiplane and pointed upwards; v is a parallel, i.e. vector $w \times u$. Angle $\alpha \in [0, \pi/2]$ is an angle between a fibre and a parallel, and angle $\alpha_1 \in [-\pi/2, \pi/2]$ is an angle between fibre projection on the plane uv and a parallel.

We compared two these angular characteristics of the fibre direction field with experimental data. The comparison was conducted along epicardial normals in two meridians (one meridian lies in the LV free wall, another one lies in the IVS) in upper, middle and lower parts of the LV wall.

5.4 Results of comparison with canine heart data

The following parameter values were used: LV height $Z^i = 90$ mm, LV wall thickness at the apex $h^i = 12$ mm, SS effective twisting angle $\phi^i_{\max} = 3\pi$, subepicardial scaling parameter $\gamma_0 = 0.05$, subendocardial scaling parameter $\gamma_1 = 0.98$.

In Fig. 5.5, we show an SS made using these parameter values, with chord images on it.

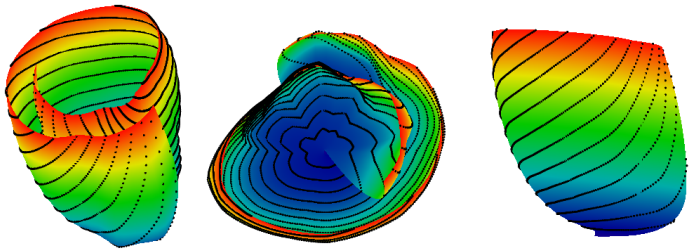

Figure 5.5: *An SS used in the human LV model, with chord images on it. On the left, side and top view; at the middle, top view; on the right, side and slightly bottom view.*

The comparison was conducted in different LV zones: upper (epicardial normal was constructed in a point with coordinate $\psi = 5°$), middle ($\psi = 35°$) and lower one ($\psi = 65°$).

In Figs 5.6–5.11 we display heart areas where we compared fibre slope angles and graphs of these angles from the experimental data (points) and from the model (solid lines). Let us analyse each figure in more detail.

At the upper part of the LV free wall (see Fig. 5.6), we see qualitative and good quantitative data agreement: angle α is maximal at the endocardium, decreases approximately to $10°$ at the middle of the wall, then increases and has its local maximum at the epicardium. In panel *D*, if we move from the endocardium to the epicardium, helix angle α_1 almost linearly decreases from big positive values to great in magnitude negative values and equals zero at the middle of the wall.

Similar behaviour of the angles can be observed at the middle (by height) part of the LV free wall (see Fig. 5.7). In comparison with the previous figure, both in the exrepiment and in the model, we notice that angle α graphs have a form close to a V-shape at the basal area and close to U-shape at the middle area. Angle α_1 graph in Fig. 5.6 seems to be a straight line, and, in Fig. 5.7, it is somewhat similar to an overturned cubic parabola (i.e. at the middle of the wall the angle's decrease becomes slower; at the external and internal parts of the wall, it becomes faster).

At the apical zone (see Fig. 5.8), the quantitative data agreement worsens, but the qualitative agreement remains. Notice that angle α_1 graphs in the model and in the experiment have come even closer to an overturned cubic parabola.

Let us now consider the IVS and compare the fibre angles along three epicardial normals.

At the basal (see Fig. 5.9), middle (see Fig. 5.10) and lower (see Fig. 5.11) zones, only a qualitative data agreement can be observed. As at the free wall, the true fibre angle α is maximal at the endocardium, then it drops reaching its minimum at the middle of free wall and rises to have its maximum at the epicardium. Notice that in experiment and in the model, the endocardial value of this angle is greater than its epicardial value at the middle and – especially – at the lower IVS part.

The helix angle α_1 decreaces monotonically at the IVS and at the LV free wall from approximately 80° on the endocardium to -60° on the epicardium.

5.5 Results of a comparison with human heart data

We followed the method used to compare angles in the canine heart.

The following parameter values (common for all meridians) were used: LV height $Z^i = 84$ mm, LV wall thickness at the apex $h^i = 11$ mm, SS effective twisting angle $\phi^i_{\max} = 2\pi$, subepicardial scaling parameter $\gamma_0 = 0.05$, subendocardial scaling parameter $\gamma_1 = 0.98$.

Graphs of dependency of angles α, α_1 on a point position on normal to the epicardium are shown in Figs. 5.12–5.17. Let us analyse the results obtained.

At the upper and middle LV areas (e.g., Figs. 5.12 and 5.13, *A*), one can see that the vertical axis goes not through the centre of horizontal LV sections, but is situated closer to the IVS. The axis position is set there because the axis must go through the apical LV area, and the LV apex projection to its basal plane is not situated at the centre of the base. If one moves the axis to the base centre, then the

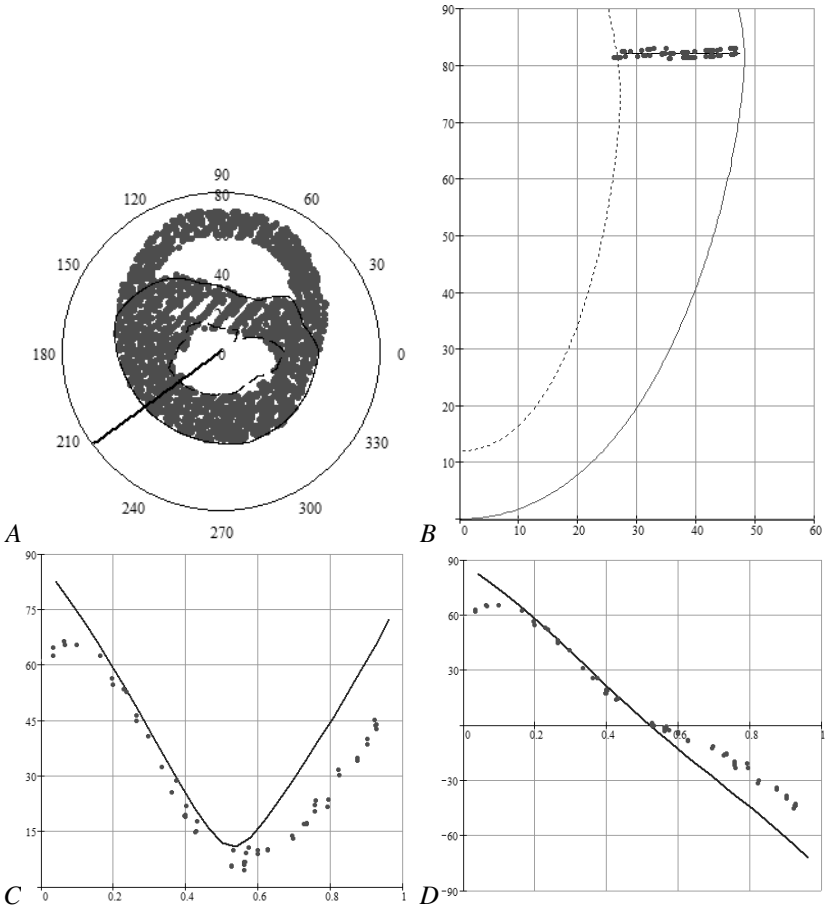

Figure 5.6: *The fibre angles in the model and in the experimental data. The LV free wall, basal area ($\psi = 5°$), canine heart. A is a horizontal LV section. The points are myocardial points from a DT-MRI scan, the straight line is a normal to the epicardium, the solid (dashed) curve is the model epicardium (endocardium). B is a meridional LV section. The solid (dashed) curve is the model epicardium (endocardium) and the points are myocardial points from a DT-MRI scan. C, D shows the angles α, α_1. The X axis displays point position in the wall depth; 0 corresponds to the endocardium, 1 corresponds to the epicardium.*

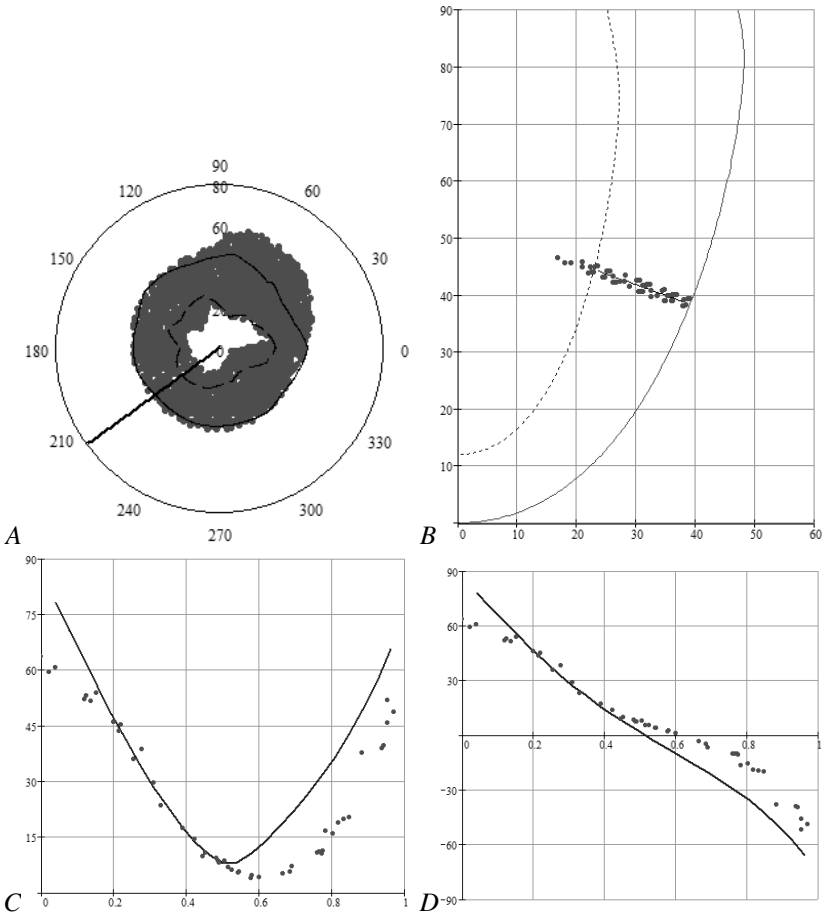

Figure 5.7: *Fibre angles in the model and in the experimental data. The LV free wall, middle height area ($\psi = 35°$), canine heart. The conventional signs are the same as in Fig. 5.6.*

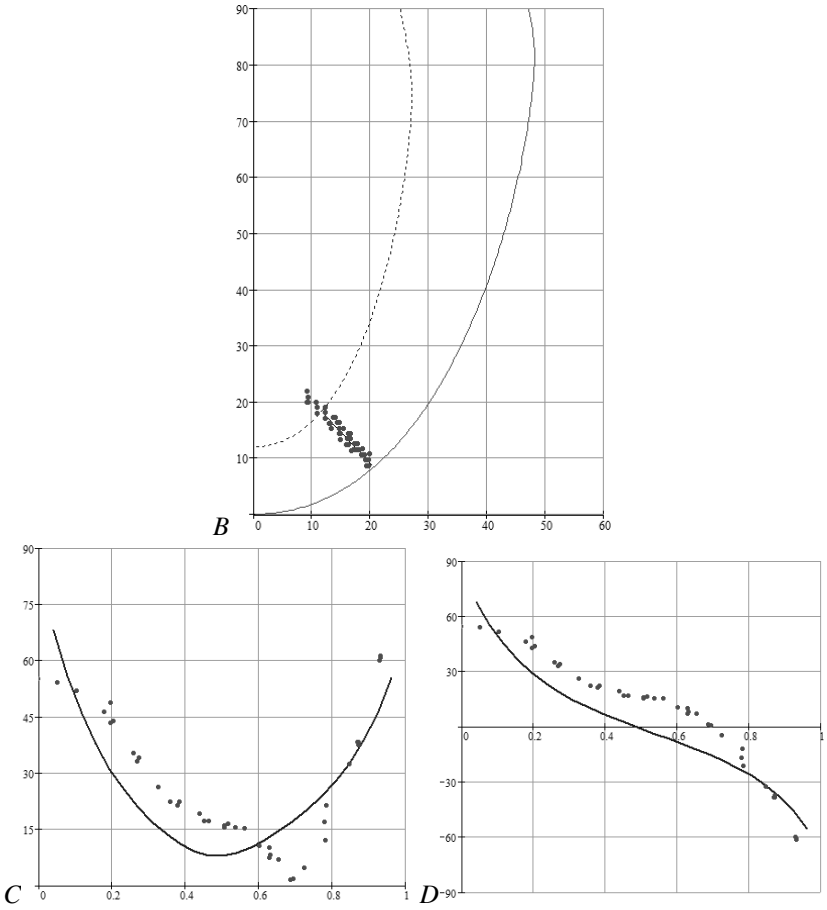

Figure 5.8: *Fibre angles in the model and in the experimental data. The LV free wall, apical area ($\psi = 65°$), canine heart. The conventional signs are the same as in Fig. 5.6.*

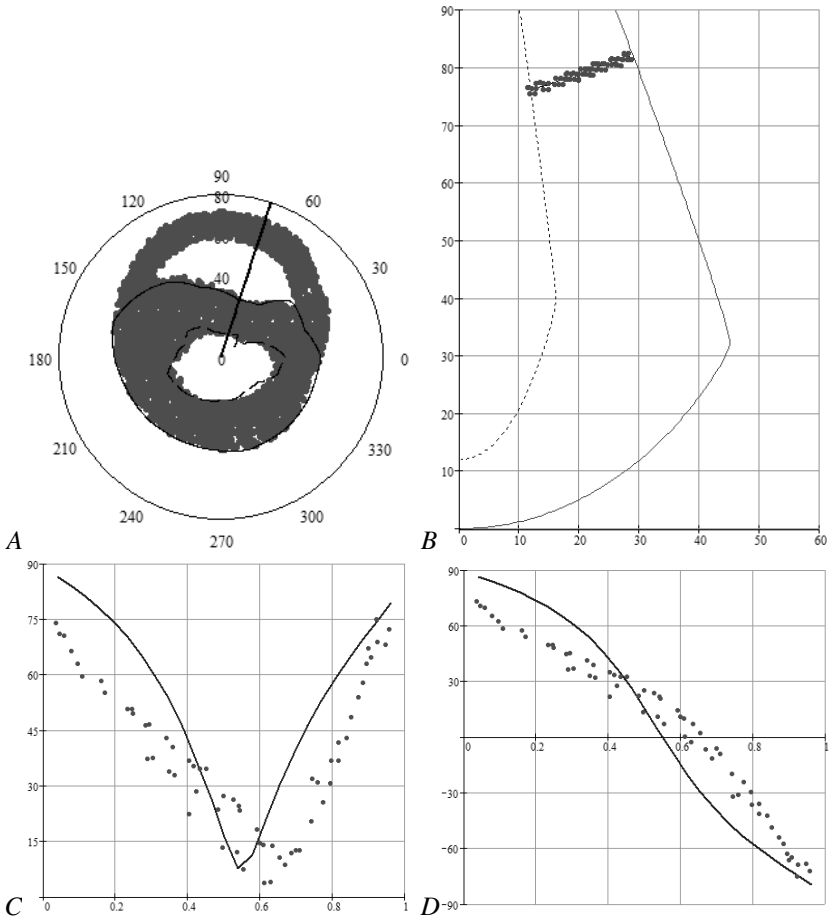

Figure 5.9: *The fibre angles in the model and in the experimental data. The IVS, basal area ($\psi = 5^\circ$), canine heart. The conventional signs are the same as in Fig. 5.6.*

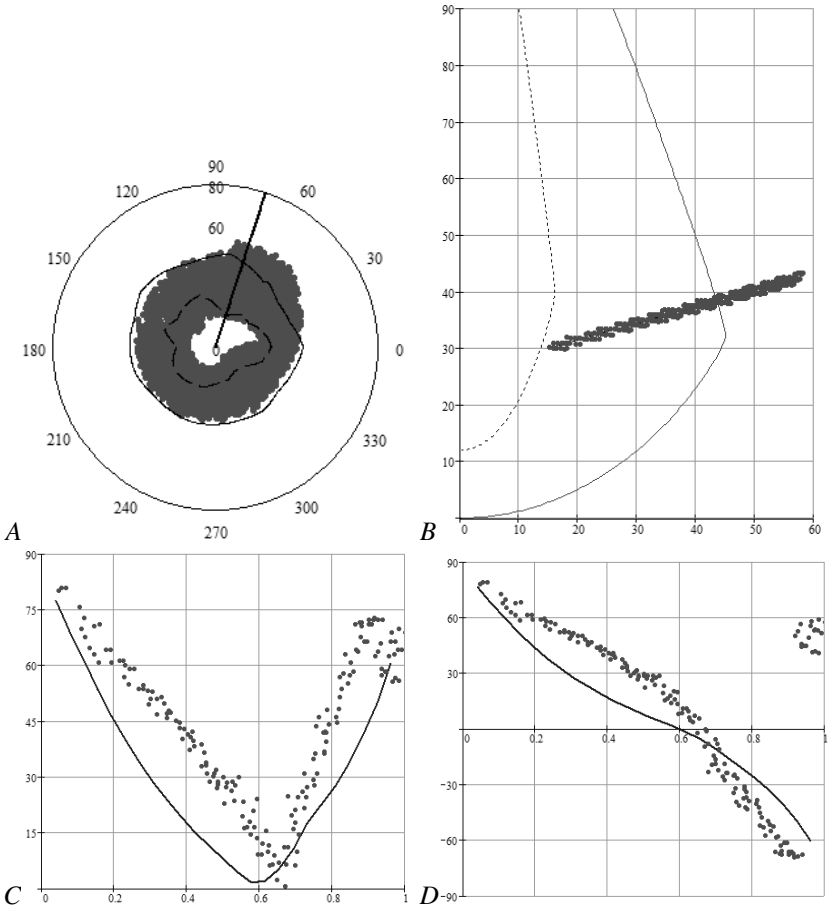

Figure 5.10: *The fibre angles in the model and in the experimental data. The IVS, middle height area ($\psi = 35^\circ$), canine heart. The conventional signs are the same as in Fig. 5.6.*

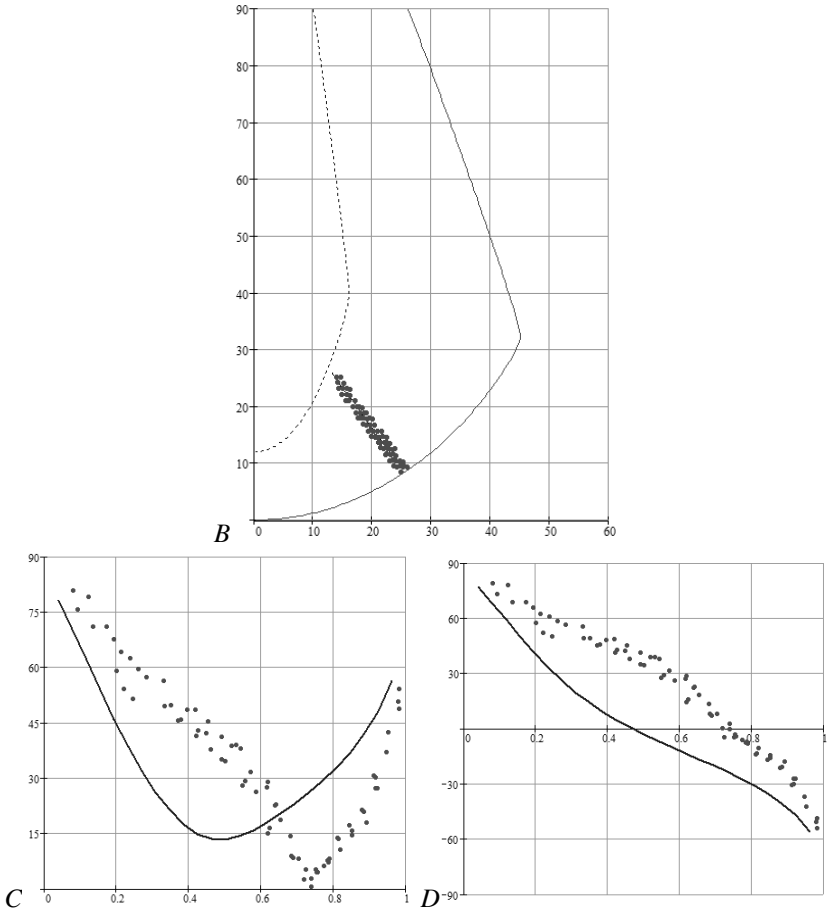

Figure 5.11: *The fibre angles in the model and in the experimental data. The IVS, apical area ($\psi = 35^\circ$), canine heart. The conventional signs are the same as in Fig. 5.6.*

apex is far from the axis in one of the meridional sections; therefore, we cannot fit the LV wall shape by this model.

Let us consider the fibre slope angles in one of the LV free wall meridians.

In the upper LV part (see Fig. 5.12), the true fibre angle α (panel *C*) in the model rather accurately reproduces the DT-MRI data. It descends from 90° on the endocardium to approximately 25° at the middle of the wall, then it grows and reaches 70° on the epicardium. The helix angle (panel *D*) in the model is also rather close to the experimental data.

The middle part of the free wall (by height) (see Fig. 5.13) shows an essentially large dispersion of the both angles values. At the same time, their conduct is mostly the same, as in the basal zone and the model can reproduse it both qualitatively and quantitatively.

One can make practically the same statement about the angles at the lower part of LV free wall (see Fig. 5.14). Let us notice only that in the subepicardial wall part does the angle α increase considerably more dramatically than usual; the angle α_1 increases, and a great variation of its values can be seen.

In the upper part of IVS (see Fig. 5.15), the angles that we discussed are very wide in the model and in the experimental data.

In the middle and lower IVS parts (see Figs. 5.16 and 5.17), the model reproduces the angles reasonably accurately.

If one considers the fibres in the radial direction, our model (like the model from [88]) imitates the distinctive arrangement of fibres in the ventricular wall (see [88], Fig. 14). This arrangement was called the “Japanese fan” by Streeter (see [105], Fig. 42, *C*).

We can conclude that our model adequately reproduces the fibre directions in the LV.

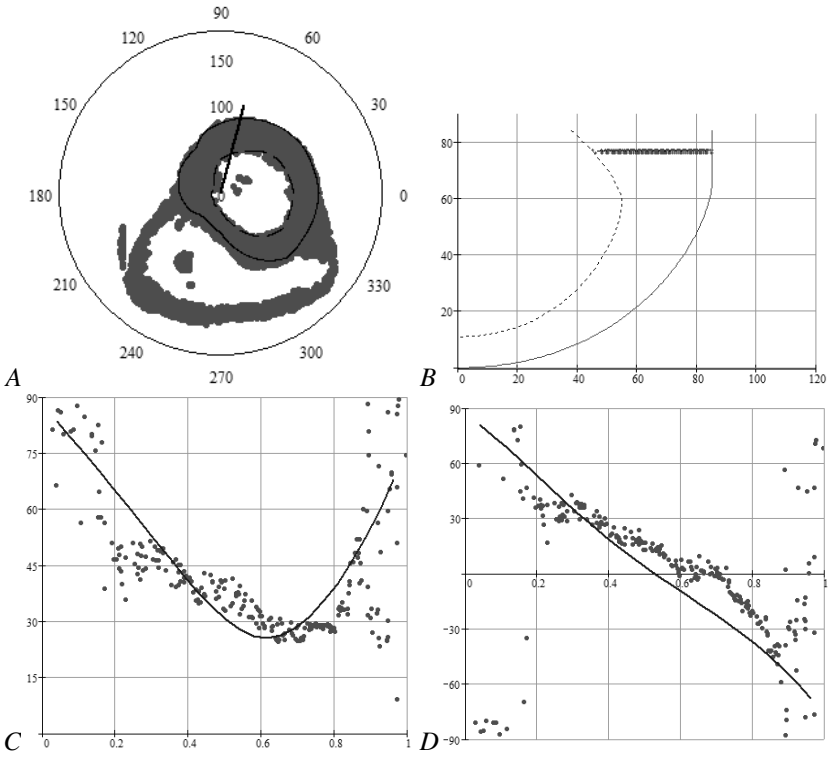

Figure 5.12: *Fibre angles in the model and in the experimental data. The LV free wall, basal area ($\psi = 5^\circ$), human heart. The conventional signs are the same as in Fig. 5.6.*

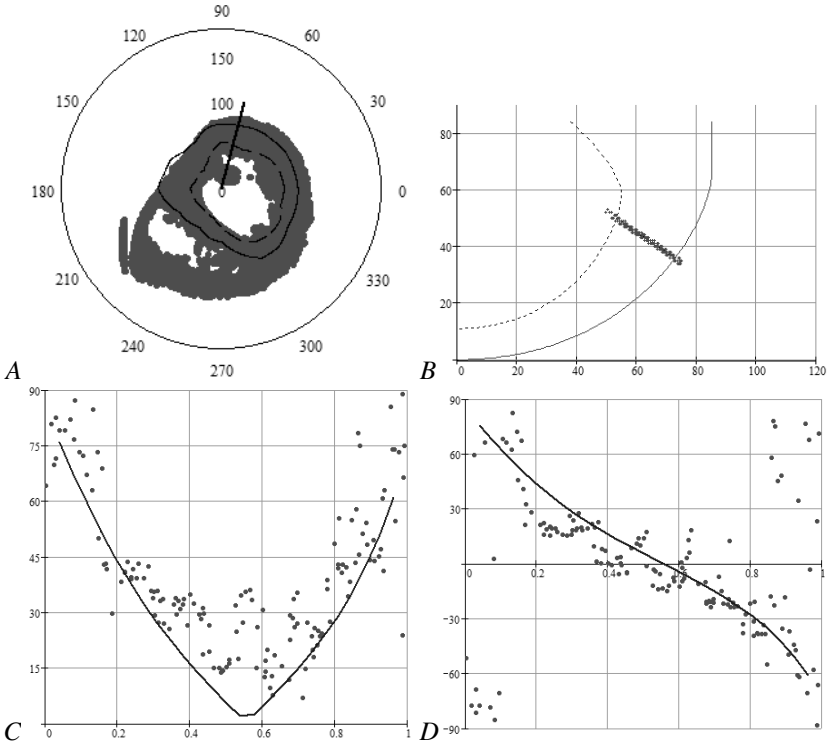

Figure 5.13: *Fibre angles in the model and in the experimental data. The LV free wall, middle area ($\psi = 35°$), human heart. The conventional signs are the same as in Fig. 5.6.*

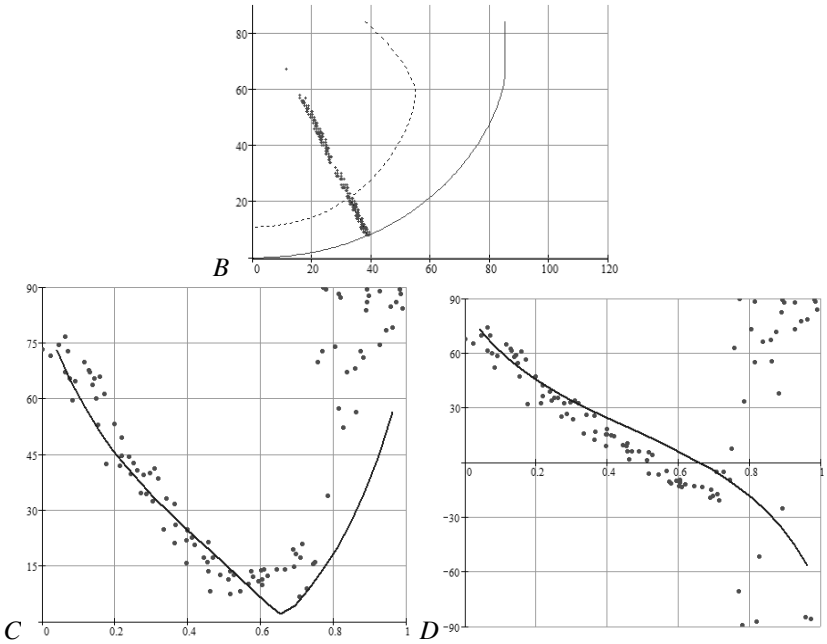

Figure 5.14: *Fibre angles in the model and in the experimental data. The LV free wall, apical area ($\psi = 65°$), human heart. The conventional signs are the same as in Fig. 5.6.*

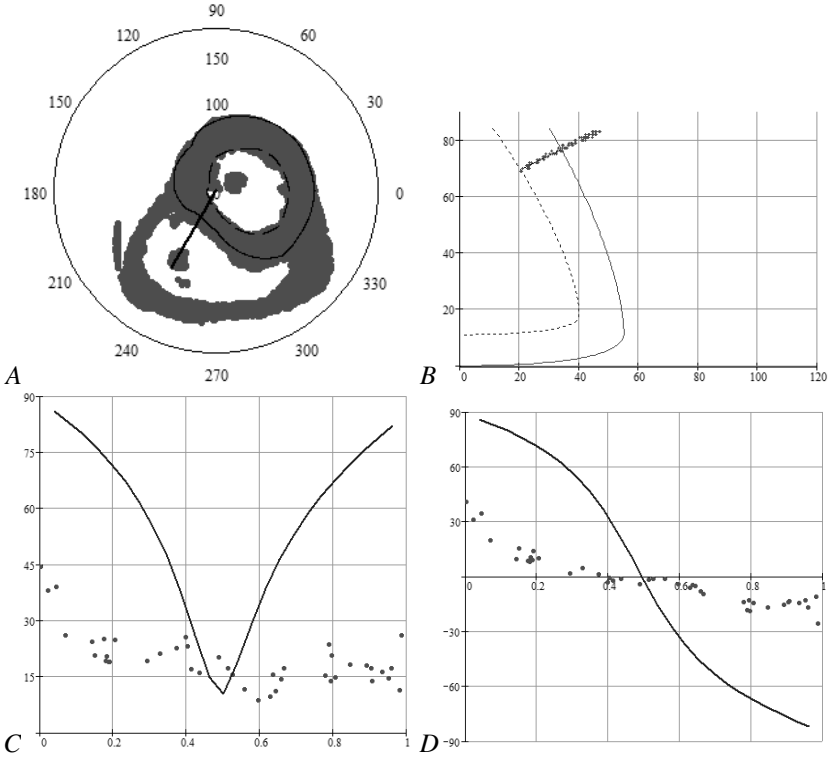

Figure 5.15: *Fibre angles in the model and in the experimental data. The IVS, basal area ($\psi = 5^\circ$), human heart. The conventional signs are the same as in Fig. 5.6.*

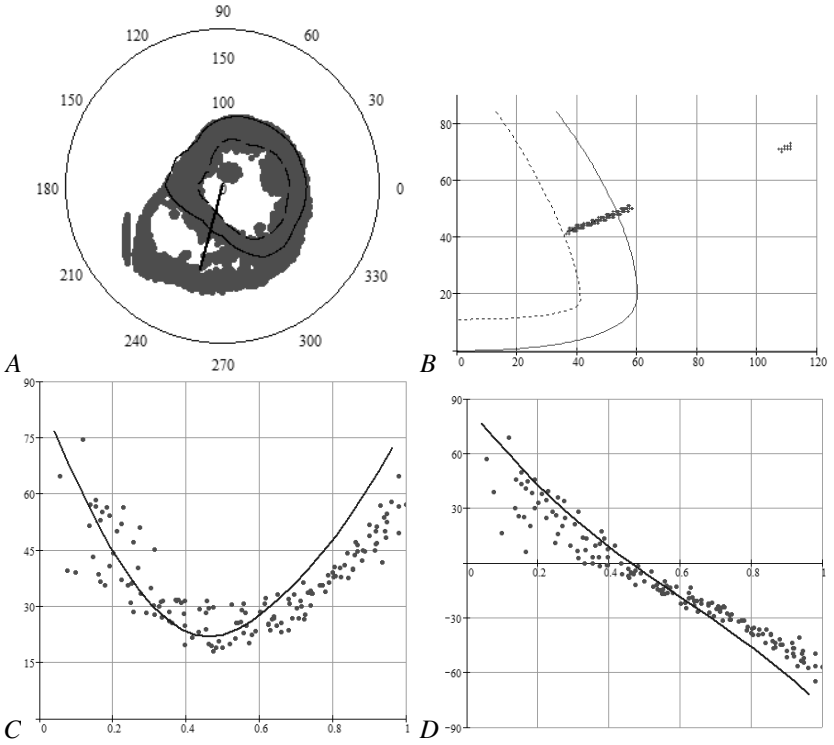

Figure 5.16: *Fibre angles in the model and in the experimental data. The IVS, middle area ($\psi = 25°$), human heart. The conventional signs are the same as in Fig. 5.6.*

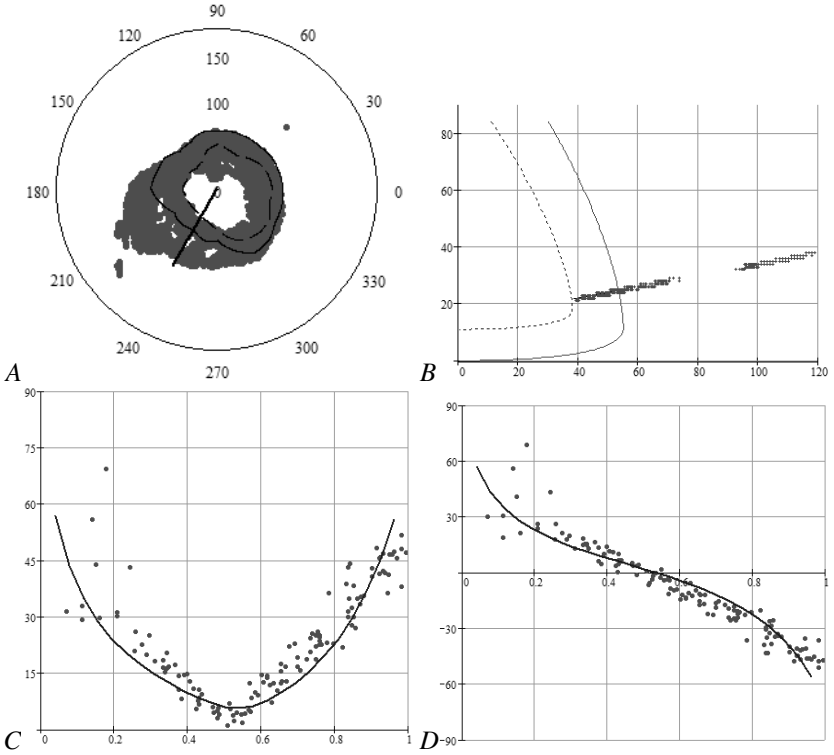

Figure 5.17: *Fibre angles in the model and in the experimental data. The IVS, apical area ($\psi = 45°$), human heart. The conventional signs are the same as in Fig. 5.6.*

5.6 Discussion

This section deals with limitations, ways of verification, usage and further development of the model constructed.

Limitations

The model adequately reproduces the fibre angles in the upper and middle zones of the LV free wall and in the middle and lower zones of the IVS of human heart (the angles are modelled slightly less accurately in the canine heart). Nevertheless, the data agreement in the apical zone of free wall is only qualitative; in the IVS upper part of human heart, the model yields results that differ totally from the experimental data.

The inaccurate reproduction of the fibre direction angles in the apical LV zone can be explained using Torrent-Guasp's "unique muscular band" approach. According to this theory (e.g., [53, 114]), the left and right ventricle myocardium forms a single long wrapped muscular band. The LV and IVS together take roughly 75% of the band lenght, and the right ventlicle takes 25% (called the "right segment"). It is particularly important that the upper part (approximately two thirds) of LV free wall is formed from one band area ("left segment"), and the lower one (about one third) is formed from another area ("descendent segment") that is not adjacent to the first one. The model reproduces the wrapping of the left segment (exterior upper part of the LV free wall) well, but not the folding of the descendent and ascendent segments. In the descendent segment, the model can reproduce well the fibre directions in the area that is close to the left segment (internal upper part of the LV free wall), its lower middle area (internal lower part of the LV free wall and IVS) and the upper part which is close to the ascendent segment (the mid-myocardial LV free wall zone). In the ascendent segment, there are two relatively small areas where the tomography data are not reproduced well; one adjoins the aorta, another abuts the apex. The rest of ascendent segment corresponds to the external part of LV free wall and IVS; the fibre run is reproduced well here.

Experimental methods that can be used to verify our model

Currently, there are several experimental methods that can measure fibre orientation in the heart. One of them is the diffusion tensor imaging (DTI) technique. In this approach, a researcher finds the diffusion matrix of water molecules in the heart. The main directions of diffusion are determined by the structure of the tissue [41, 42, 57, 121], and by calculating the eigenvectors of the matrix corresponding to the largest eigenvalue, the fibre direction can be found. Diffusion tensor magnetic resonance imaging (DT-MRI) measurements can be done with spatial resolutions up to 200 μm [33]. Another advanced technique is the micro computerized tomography (Micro-CT) imaging. Micro-CT measurements can be done with spatial resolutions up to 36–70 μm [9], and both these methods produce high-quality data that can be used in computer models.

Direct measurement of anisotropy also can be conducted via tedious histological studies of fibre direction in 3-D [65, 105]. In this method, the researcher makes a series of parallel sections of the heart. In each section, angles of fibre slope are measured, which gives a full picture of the fibre directions in the heart. Recently, Smaill et al. developed a combined high-resolution serial imaging microscopy technique [117]. In this method, after heart fixation, they perform cross-section and make successive, high-resolution images of the heart. Then, using computer processing, the data are collected to form an overall 3-D dataset.

In [49], the myofibres in the foetal human heart are investigated using quantitative polarized light microscopy. The hearts are embedded in a transparent resin, polymerized and then sectioned. Afterward, the elevation and azimuth angles are measured by means of polarized light (see [49] for details).

Comparison with other models

Experimental data on the fibre orientation obtained as described above may be in different ways used for construction of anatomical computational models:

- either as a discrete dataset in finite element models [40, 125, 131];

- or for the verification of rule-based models, i.e. the models formed on the base of some constitutive rule [10, 15, 46, 101].

One of the most recent rule-based methods is a Laplace–Dirichlet algorithm [10], which takes a noisy DTI-derived fibre orientation field as input data and yields, firstly, the transmural and apicobasal directions for the entire myocardium and, secondly, a smooth and continuous fibre orientation field. Another approach was used by Peskin, who derived fibre orientation field from the principles of mechanical equilibrium [83]. One more anatomic model based on a principle of the mechanical activity of the heart was a model by Chadwick, who considered a cylindrical LV and specified the helix angle linearly depending on point position in the LV wall [20]. Beyar et al. shaped LV into a spheroid and also used linear dependence of the helix angle on the distance between any point in the ventricle wall and the endocardium [12]. An interesting example of the theoretical approach was developed by Arts et al. in 1992 [16]. They constructed a model of an ellipsoidal LV, complicated the law of helix angle change to a piecewise quadratic one and quantified orientation of the muscle fibres via the helix fibre angle distribution, which was found upon application of the mechanical adaptative principle suggested by Arts et al. in 1982 [8].

In this work we present our rule-based model focused on the LV morphology including simulation of the ventricle shape and fibre orientation in its wall. The developed formalism is substantially associated with both ventricle band concept of cardiac architecture given by Torrent-Guasp [111] and anatomic observations presented by Streeter in his classical work [105]. In our approach to the modelling of the LV architecture, anisotropy of the heart was derived from some general principles. In our model, the LV is considered a set of identical spiral surfaces combined with each other by rotation about the vertical axis. Every spiral surface is defined analytically and represents a mapping of a half disc. The first step of the transformation is the mapping of the semicircle to a conical surface. In the second step, the conical surface is transformed to a curved spiral surface, representing the quasi-elliptical shape of the LV boundary surface. Finally, every spiral surface is

filled with myocardial fibres, represented by the transformed images of the chords that were parallel to the diameter in the initial semicircle (see figure 2.1).

Our model is not the only wrapping-based myocardium model. Sinha et al. proposed in [103] a model of one myocardial layer which had a rectangular form and was wrapped around a (truncated) cone. They used this very simple model to study termination of re-entrant waves rotating around obstacles in cases of isotropy and anisotropy but without any linkage to the real fibre pattern in the heart ventricles.

We used experimental data from the above cited work by Streeter [105], as well as from other more recent works [65] for the model verification. In particular, the model proved to reproduce adequately both the looping arrangement of the muscle fibres and the specific 3-D pattern of the relative positions of the fibres in the transmural direction through the ventricle wall.

These accurate reproductions allow us to consider the model a touchstone in validating the ventricle band concept of cardiac architecture originated by Torrent-Guasp, because the model, based on this concept, yields an adequate fibre field as a consequence of the postulates.

It seems reasonable to compare our model with another rule-based model that assigns fibre orientation locally, particularly with the very interesting and promising model by Bayer et al., mentioned earlier in this section [10]. For this comparison, only the reproduced fibre orientation in various parts of the LV of the two models can be used. The Bayer model is based on DT-MRI data of anisotropy in two ventricles of a canine heart. The average angle divergence between the model and the DT-MRI fibre directions is 23°; that is there is not a complete quantitative matching of the real experimental and reproduced data, but there is reasonable concordance. Specifically, Bayer's model quantitatively reproduces fibre anisotropy in the basal and apical LV zones better than our model (see [10] figure 3). In the section describing the limitations of our model, we point to this quantitative inaccuracy in our model and propose some ways to eliminate it. At the same time, our model better reproduces the experimental data in the middle LV zone; namely, we obtain the specific s-like plot of the angle α_1 in the transmural direction (see

figure 2.19, the bottom right panel). In Bayer's model, this dependency is linear by definition. Moreover, if we follow the cited paper by Bayer et al. [10, Eq. (1), (2)], all plots for angle α_1 presented in figure 2.16 reveal independence of the angle from both the latitude and the longitude of the intramural position within the wall. Bayer and co-authors suggest that their model can be easily improved to take the non-linearity of angle α_1 into account. But, it also is necessary to make the anisotropy latitudinally and longitudinally independent, and it is not easy to do so. Our model reproduces such a dependence (see figures 2.13–2.19), which is proper for real hearts, and does it quite fairly for the middle zone of the LV.

One more simplification of Bayer's model concerns transmural rotation of the fibres' directions, named 'Japanese fan' by Streeter ([105] figure 42c). In that model, the rotation is defined in one plane only, that is, around only one axis, settled transmurally. This plane lies tangentially to the surface determined by the condition $d = \text{const}$, where d is a term specified in the cited paper by Bayer et al. [10] and presents there the occurrence depth of particular locus within the wall; for example, $d = 0$ on the endocardium and $d = 1$ on the epicardium. Moreover, if we assess results obtained in Bayer's model by means of the angle α_3 defined by Streeter [105] and determine transmural direction of the fibre orientation, it will prove to be constantly 0, which is a substantial simplification. This feature does not allow mapping the 3-D pattern of the relative positions of the fibres in the transmural direction through the ventricular wall.

In contrast, in our model the 3-D pattern is taken into consideration (see figures 2.13–2.19, and note that in the middle LV zone these angles are reproduced quite well).

Thus, we believe that both models have their own virtues and their own limitations. Additional development of the models would be useful to surmount the limitations.

Further development and usage of the model

The analytical description of the cardiac geometry can be used in developing new numerical methods for the study of electrophysiological and mechanical activity of the LV. The model is an analytical map of a rectangle in space (γ, ψ, ϕ) to a curvilinear LV; therefore, one can make a rectangular numerical scheme in the coordinates (γ, ψ, ϕ) (where the boundary conditions can be written in the simpliest manner), and we can consider anisotropy by using explicit analytical formulae. The model can also be utilized for the generation of different anisotropical properties of the heart, for alteration of the LV shape (by change of the model parameters) and for studying their influence on the cardiac electrical and mechanical function.

6

Conclusion and future work

In this thesis, we have constructed the analytical description of the cardiac anatomy based on the spiral surfaces concept. The model can be used for verification of the Torrent-Guasp band concept and for the various numerical simulations to study the effects of anisotropy on the cardiac excitation and mechanical function. Our model shows a good qualitative agreement between the simulated fibre orientation field and the experimental data on the LV anisotropy.

The analytical representation of the geometry presented here was used for the development of new numerical methods to study the electrical activity of the heart. As our model provides an analytical mapping of a rectangle in (γ, ψ, ϕ) space into the heart shape, we formulated a numerical scheme in (γ, ψ, ϕ) space (where the

representation of the boundary conditions is the most natural) and accounted for anisotropy by the explicit analytical formulae. Such mapping was also used to generate the various anisotropic properties of the heart and to study their effect on the electrical heart function.

The electrophysiological experiments from the third and fourth chapters showed how shape, fibre angles and anisotropy of the ventricle affect the propagation of "usual" and the scroll waves. We proved that the rotation of the fibres in the cardiac wall increases the propagation of the waves and attenuates the anisotropy of the tissue. The behaviour of the scroll waves and their filaments depend on the different factors of the medium in a complex way.

In the chapter 5, we proposed the non-symmetrical anatomical LV model. This model was fitted to a human and a canine left ventricle (data were obtained from the DT-MRI) and compared it with the DT-MRI data on the fibre directions. A good qualitative and – in some LV wall areas – a quantitative agreement between the model and the experimental data is demonstrated. The model can be used both for the band hypothesis verification and for the various numerical experiments studying the anisotropy influence on the electrical excitation spread and simulating cardiac mechanical function.

Overall, we did a first step in analytical cardiac computational anatomy and physiology. However, many important questions still need to be addressed in the subsequent research.

First, note that the fibres in our model end on the basal plane of the left ventricle. However, the experimental data show that the fibres make a loop and do not end on the fibrous ring. They continue upwards as curves on a torus and descend to the apical region. It is interesting that we see the same pattern in the apical region of the heart. There, the descending fibres make a narrow hole in the apex. This hole is filled by the fibrous tissue and, therefore, is not excitable. Moreover, as a connective tissue, it has different passive mechanical properties in comparison with the working myocardium. Therefore, including two special regions in this model with a toroidal pattern of fibres can improve its capabilities to reproduce

the cardiac properties related with the spiral waves and the mechanical pumping function.

Second, in the thesis, we compared only the fibre directions with the experimental data, but we have not compared the sheet normals, yet. As both the model and the modern experimental devices provide data on the myocardial layers, such a comparison should be conducted, as it is important for the simulations of the orthotropic mechanical properties of the myocardium.

The main function of the heart is its pumping work, and the electrical activity only initiates the mechanical contraction. Therefore, a clear direction for future research is to use our anatomical model for the simulation of the mechanical activity of the heart. This work has already been started. The first results (not yet published) show that the ventricle can contract effectively, and its ejection fraction can be as much as normal, about 65%. Moreover, due to the oblique directions of the fibres, it displays a specific torsion, which is responsible for reaching the high ejection fraction without a big contraction of the fibres.

There are many different cell-level models and much experimental data on the hearts of different animals, such as a mouse, rat, guinea pig, dog and rabbit. Our anatomical model can be fitted to their hearts as well. After adding a cell-level model, it will be possible to simulate the electrophysiological activity of not only human hearts, but also animal hearts. This may allow a researcher to study those basic physiological properties of the hearts that are commonly used in experimental research.

The studies of the scroll waves and the filaments dynamics, discussed in the third and fourth chapters, are important as those waves are signs of dangerous cardiac arrhythmias. Using our model, we can also implement various therapeutic approaches to remove these scrolls and to stop the arrhythmias. We can study, for example, a process of overdrive pacing of the cardiac arrhythmias. To do this, we can put electrodes to our model and force them with a high frequency. Using that, we can find the conditions for the best strategies of removing these sources of arrhythmias from the heart. This might be useful in clinical practice.

In the present work, we consider the left ventricle only. The LV performs the main mechanical function by pumping arterial blood to the aorta. The heart also contains the right ventricle, which obtains venous blood from the right atrium and pumps blood to the pulmonary trunk. From the papers of Torrent-Guasp, we see that the two ventricles are parts of one myocardial band. Therefore, it is a natural question whether a model of only the left ventricle could be generalised to a biventricular model. We proposed a method to construct the anatomical models: the spiral surfaces method. Can the same approach be used to describe the right ventricle? We already tried to do this by presenting the right ventricle cavity as a gap in the cardiac wall. Unfortunately, the comparison with the experimental data showed inadequate fibre angles, which makes us conclude that the right ventricle should be modelled in a different way. A promising means to do this is to model folding a myocardial band with the fibres to a complex figure.

One more interesting hypothesis concerning the fibres on the myocardial sheets is that they follow the geodesic lines on the sheets. Our model provides non-geodesic lines on the spiral surfaces. It would be interesting to try to construct some (maybe axisymmetrical on the first step) set of surfaces and their geodesic lines, so that the orientation of normals to surfaces and tangents to fibres might be close to experimental data.

References

[1] K.I. Agladze, V.I. Krinsky, A.V. Panfilov, H. Linde, and Kuhnert L. Three-dimensional vortex with a spiral filament in a chemically active medium. Physica D: Nonlinear Phenomena, 39 (1):38–42, 1989.

[2] RR Aliev and AV Panfilov. A simple two-variable model of cardiac excitation. Chaos, Solitons and Fractals, 7(3):293–301, 1996.

[3] S. Alonso and A.V. Panfilov. Negative filament tension in the luo-rudy model of cardiac tissue. Chaos, 17:015102, 2007.

[4] S. Alonso, F. Sagues, and A.S. Mikhailov. Taming winfree turbulence of scroll waves in excitable media. Science, 299:1722–1725, 2003.

[5] R H Anderson, M Swerup, D Sanchez-Quintana, M Loukas, and P P Lunkenheimer. Three-dimensional arrangement of the myocytes in the ventricular walls. Clinical Anatomy, 22:64–76, 2009.

[6] RH Anderson, M Smerup, D Sanchez-Quintana, M Loukas, and PP Lunkenheimer. How are the myocytes aggregated so as to make up the ventricular mass? Semin Thorac Cardiovasc Surg Pediatr Card Surg Annu., pages 76–86, 2007.

[7] Charles Antzelevitch and Jeffrey Fish. Electrical heterogeneity within the ventricular wall. Basic Research in Cardiology, 96(6):517–527, 2001.

[8] T Arts, PC Veenstra, and RS Reneman. Epicardial deformation and left ventricular wall mechanics during ejection in the dog. Am J Physiol, 243(Heart Circ. Physiol. 12):H379–H390, 1982.

[9] O.V. Aslanidi, T. Nikolaidou, Jichao Zhao, B.H. Smaill, S.H. Gilbert, A.V. Holden, T. Lowe, P.J. Withers, R.S. Stephenson, J.C. Jarvis, J.C. Hancox, M.R. Boyett, and Henggui Zhang. Application of micro-computed tomography with iodine staining to cardiac imaging, segmentation, and computational model development. Medical Imaging, IEEE Transactions on, 32(1):8–17, 2013.

[10] JD Bayer, RC Blake, G Plank, and NA Trayanova. A novel rule-based algorithm for assigning myocardial fiber orientation to computational heart models. Ann Biomed Eng., 2012.

[11] A Benninghoff. Die architektur des herzmuskels. eine vergleichend anatomische und vergleichend funktionelle betrachtung. Morph Jahrb., 67:262–317, 1931.

[12] R Beyar and S Sideman. A computer study of the left ventricular performance based on fiber structure, sarcomere dynamics, and transmural electrical propagation velocity. Circ Res, 55:358–375, 1984.

[13] V.N. Biktashev, A.V. Holden, and H. Zhang. Tension of organizing filaments of scroll waves. Phil. Trans. R. Soc. Lond. A, 347:611–630, 1994.

[14] I.V. Biktasheva, H. Dierckx, and V.N. Biktashev. Drift of scroll waves in thin layers caused by thickness features. Physical Review Letters, page submitted., 2014.

[15] Martin J. Bishop, Gernot Plank, Rebecca A. B. Burton, Jurgen E. Schneider, David J. Gavaghan, Vicente Grau, and Peter Kohl. Development of an anatomically detailed mri-derived rabbit ventricular model and assessment of its impact on simulations of electrophysiological function. Am J Physiol Heart Circ Physiol., 298(2):H699–H718, 2010.

[16] PHM Bovendeerd, T Arts, JM Huyghe, DH Van Campen, and RS Reneman. Dependence of local left ventricular wall mechanics on myocardial fiber orientation: a model study. J Biomechanics, 25(10):1129–1140, 1992.

[17] GD Buckberg, LW Myron, M Ballester, R Beyar, D Burkhoff, HC Coghlan, M Doyle, ND Epstein, M Gharib, RE Ideker, NB Ingels, MM LeWinter, AD McCulloch, GM Pohost, LJ Reinlib, DJ Sahn, G Sopko, FG Spinale, HM Spotnitz, F Torrent-Guasp, and EP Shapiro. Left ventricular form and function : Scientific priorities and strategic planning for development of new views of disease. Circulation, 110(14):e333–336, 2004.

[18] Gerald D. Buckberg. Architecture must document functional evidence to explain the living rhythm. European Journal of Cardio-Thoracic Surgery, 27(2):202–209, 2005.

[19] Francis L Burton and Stuart M Cobbe. Dispersion of ventricular repolarization and refractory period. Cardiovascular Research, 50(1):10–23, 2001.

[20] RS Chadwick. Mechanics of the left ventricle. Biophysical Journal, 39:279–288, 1982.

[21] R.H. Clayton, O. Bernus, E.M. Cherry, H. Dierckx, F.H. Fenton, L. Mirabella, A.V. Panfilov, F.B. Sachse, G. Seemann, and H. Zhang. Models of cardiac tissue electrophysiology: Progress, challenges and open questions. Progress in Biophysics and Molecular Biology, 104(13):22–48, 2011.

[22] AF Corno, MJF Kocica, and F Torrent-Guasp. The helical ventricular myocardial band of torrent-guasp: potential implications in congenital heart defects. Eur J Cardiothorac Surg., 29 (Supplement 1):S61–S68, 2006.

[23] H. Dierckx, O. Selsil, H. Verschelde, and V.N. Biktashev. Buckling of scroll waves. Phys Rev Lett, 109:174102, 2012.

[24] Hans Dierckx, Evelien Brisard, Henri Verschelde, and Alexander V. Panfilov. Drift laws for spiral waves on curved anisotropic surfaces. Phys. Rev. E, 88:012908, Jul 2013.

[25] Hans Dierckx, Evelien Brisard, Henri Verschelde, and Alexander V. Panfilov. Drift laws for spiral waves on curved anisotropic surfaces. Physical Review E, 88(1):012908, 2013.

[26] Hans Dierckx and Henri Verschelde. Effective dynamics of twisted and curved scroll waves using virtual filaments. Phys. Rev. E, 88:062907, Dec 2013.

[27] DJ Dosdall, PB Tabereaux, JJ Kim, GP Walcott, JM Rogers, CR Killingsworth, J Huang, PG Robertson, WM Smith, and RE Ideker. Chemical ablation of the purkinje system causes early termination and activation rate slowing of long-duration ventricular fibrillation in dogs. Am J Physiol Heart Circ Physiol., 295(2):H883–9, 2008.

[28] B. Echebarria, V. Hakim, and H. Henry. Nonequilibrium ribbon model of twisted scroll waves. Phys. Rev. Lett., 96:098301, 2006.

[29] F.H. Fenton and A. Karma. Vortex dynamics in three-dimensional continuous myocardium with fiber rotation: filament instability and fibrillation. Chaos, 8:20–47, 1998.

[30] Flavio Fenton and Alain Karma. Vortex dynamics in three-dimensional continuous myocardium with fiber rotation: Filament instability and fibrillation. Chaos: An Interdisciplinary Journal of Nonlinear Science, 8(1):20–47, 1998.

[31] CC Fox and GM Hutchins. The architecture of the human ventricular myocardium. Hopkins Med J, 130:289–299, 1972.

[32] AF Frangi, D Rueckert, JA Schnabel, and WJ Niessen. Automatic construction of multiple-object three-dimensional statistical shape models: applica-

tion to cardiac modeling. IEEE Transact on Med Imag, 21(9):1151–1166, 2002.

[33] S.H. Gilbert, G.B. Sands, I.J. LeGrice, B.H. Smaill, O. Bernus, and M.L. Trew. A framework for myoarchitecture analysis of high resolution cardiac mri and comparison with diffusion tensor mri. In Engineering in Medicine and Biology Society (EMBC), 2012 Annual International Conference of the IEEE, pages 4063–4066, 2012.

[34] Stephen H. Gilbert, Alan P. Benson, Pan Li, and Arun V. Holden. Regional localisation of left ventricular sheet structure: integration with current models of cardiac fibre, sheet and band structure. European Journal of Cardio-Thoracic Surgery, 32(2):231–249, 2007.

[35] E Grandi, FS Pasqualini, and DM Bers. A novel computational model of the human ventricular action potential and ca transient. Journal of Molecular and Cellular Cardiology, 48(1):112–121, 2010. Special Issue: Ion Channels.

[36] Eleonora Grandi, Francesco S. Pasqualini, and Donald M. Bers. A novel computational model of the human ventricular action potential and ca transient. Journal of Molecular and Cellular Cardiology, 48(1):112 – 121, 2010. Special Issue: Ion Channels.

[37] RP Grant. Notes on the muscular architecture of the left ventricle. Circulation, 32:301–308, 1965.

[38] R.A. Gray, J. Jalife, A. Panfilov, W.T. Baxter, C. Cabo, and A.M. Pertsov. Non-stationary vortex-like reentrant activity as a mechanism of polymorphic ventricular tachycardia in the isolated rabbit heart. Circulation, 91:2454–2469, 1995.

[39] JL Greenstein and RL Winslow. Integrative systems models of cardiac excitation-contraction coupling. Circ Res, 108:70–84, 2011.

[40] V Gurev, T Lee, J Constantino, H Arevalo, and NA Trayanova. Models of cardiac electromechanics based on individual hearts imaging data: Image-based electromechanical models of the heart. Biomech Model Mechanobiol, 10:295–306, 2011.

[41] P Helm, MF Beg, MI Miller, and RL Winslow. Measuring and mapping cardiac fiber and laminar architecture using diffusion tensor mr imaging. Ann N Y Acad Sci., 1047:296–307, 2005.

[42] PA Helm, HJ Tseng, L Younes, ER McVeigh, and RL Winslow. Ex vivo 3d diffusion tensor imaging and quantification of cardiac laminar structure. Magnetic Resonance in Medicine, 54:850–859, 2005.

[43] CS Henriquez. Simulating the electrical behavior of cardiac tissue using the bidomain model. Crit Rev Biomed Eng, 21(1):1–77, 1993.

[44] W Hort. Makroskopische und mikrometrische untersuchungen am myokard verschieden stark gefllter linker kammern. Virchows Arch Pathol Anat, 333:523–564, 1960.

[45] W Hort. Quantitative morphology and structural dynamics of the myocardium. Methods Achiev Exp Pathol, 5:3–21, 1971.

[46] R Hren. A Realistic Model of the Human Ventricular Myocardium: Application to the Study of Ectopic Activation. PhD thesis, Halifax, Nova Scotia, Canada: Dalhousie University, 1996.

[47] PJ Hunter, AD McCulloch, and HE Ter Keurs. Modelling the mechanical properties of cardiac muscle. Prog Biophys Mol Biol, 69:289–331, 1998.

[48] X Jie, V Gurev, and N Trayanova. Mechanisms of mechanically induced spontaneous arrhythmias in acute regional ischemia. Circ.Res., 106:185–192, 2010.

[49] PS Jouk, Y Usson, G Michalowicz, and L Grossi. Three-dimensional cartography of the pattern of the myofibres in the second trimester fetal human heart. Anat Embryol (Berl)., 202(2):103–118, 2000.

[50] J.P. Keener. The dynamics of three-dimensional scroll waves in excitable media. Physica D, 31:269–276, 1988.

[51] JP Keener and AV Panfilov. A biophysical model for defibrillation of cardiac tissue. Biophys. J., 71:1335–1345, 1996.

[52] RH Keldermann, MP Nash, H Gelderblom, VY Wang, and AV Panfilov. Electromechanical wavebreak in a model of the human left ventricle. Am J Physiol., 299(1):H134–H143, 2010.

[53] Mladen J. Kocica, Antonio F. Corno, Vesna Lackovic, and Vladimir I. Kanjuh. The helical ventricular myocardial band of torrent-guasp. Seminars in Thoracic and Cardiovascular Surgery: Pediatric Cardiac Surgery Annual, 10(1):52–60, 2007.

[54] L Krehl. Beitrge zur kenntnis der fllung und entleerung des herzens. Abh Math-Phys Kl Saechs Akad Wiss, 17:341–362, 1891.

[55] IJ LeGrice, BH Smaill, LZ Chai, SG Edgar, JB Gavin, and PJ Hunter. Laminar structure of the heart: ventricular myocyte arrangement and connective tissue architecture in the dog. Am J Physiol, 269(2):H571–582, 1995.

[56] M Lev and CS Simkins. Architecture of the human ventricular myocardium. technique for study using a modification of the mall–maccallum method. Lab Invest., 5:396–409, 1956.

[57] PP Lunkenheimer, K Redmann, and et al. Three-dimensional architecture of the left ventricular myocardium. The Anatomical Record Part A, 288:565–578, 2006.

[58] PP Lunkenheimer, K Redmann, H Scheld, K-H Dietl, C Cryer, K-D Richter, J Merker, and W Whimster. The heart muscle's putative "secondary structure". functional implications of a band-like anisotropy. Technol Health Care, 5:53–64, 1997.

[59] FP Mall. On the muscular architecture of the ventricles of the human heart. Am J Anat., 11:211–266, 1911.

[60] C.W. Misner, K.S. Thorne, and J.A. Wheeler. Gravitation. W.H. Freeman and Co., 1973.

[61] RJ Myerburg, KM Kessler, JrA Interian, P Fernandez, S Kimura, PL Kozlovskis, T Furukawa, AL Bassett, and A Castellanos. Cardiac Electrophysiology: From Cell to Bedside, chapter Clinical and experimental pathophysiology of sudden cardiac death, pages 666–678. Philadelphia: Saunders, 1 edition, 1990.

[62] Alok Ranjan Nayak, T. K. Shajahan, A. V. Panfilov, and Rahul Pandit. Spiral-wave dynamics in a mathematical model of human ventricular tissue with myocytes and fibroblasts. Physiol Rev, 8:e72950, 2013.

[63] D Nickerson, N Smith, and P Hunter. New developments in a strongly coupled cardiac electromechanical model. Europace, 7:118–127, 2005.

[64] SA Niederer, PJ Hunter, and NP Smith. A quantitative analysis of cardiac myocyte relaxation: a simulation study. Biophys J., 90(5):1697–1722, 2006.

[65] PMF Nielsen, IJ LeGrice, BH Smaill, and PJ Hunter. Mathematical model of the geometry and fibrous structure of the heart. Am. J. Physiol., 260:H1365–H1378, 1991.

[66] D Noble. A modification of the hodgkin–huxley equation applicable to purkinje fiber action and pacemaker potential. J. Physiol., 160:317–352, 1962.

[67] D Noble. Systems biology and the heart. Science, 295:1678–1682, 2002.

[68] T O'Hara, L Virag, A Varro, and Y Rudy. Simulation of the undiseased human cardiac ventricular action potential: Model formulation and experimental validation. PLoS Comput Biol, 7(5):e1002061, 5 2011.

[69] Thomas O'Hara, Lszl Virg, Andrs Varr, and Yoram Rudy. Simulation of the undiseased human cardiac ventricular action potential: Model formulation and experimental validation. PLoS Comput Biol, 7(5):e1002061, 05 2011.

[70] AV Panfilov. Three-dimensional organization of electrical turbulence in the heart. Phys. Rev. E, 59:R6251–R6254, 1999.

[71] AV Panfilov and AV Holden. Self-generation of turbulent vortices in a 2-dimensional model of cardiac tissue. Physics Letters A, 151:23–26, 1990.

[72] AV Panfilov and AV Holden. Vortices in a system of two coupled excitable fibers. Physics Letters A, 147:463–466, 1990.

[73] AV Panfilov and AV Holden. Computer simulation of re-entry sources in myocardium in two and three dimensions. J. Theor. Biol., 161:271–285, 1993.

[74] A.V. Panfilov and A.V. Holden. Computer simulation of re-entry sources in myocardium in two and three dimensions. J. Theor. Biol., 161:271–285, 1993.

[75] AV Panfilov and AV Holden, editors. Computational Biology of the Heart. Wiley, Chichester, 1997.

[76] AV Panfilov and JP Keener. Generation of re-entry in anisotropic myocardium. J Cardiovasc Electrophysiol., 4(4):412–421, 1993.

[77] AV Panfilov and JP Keener. Re-entry in an anatomical model of the heart. Chaos, Solitons and Fractals, 5:681–689, 1995.

[78] A.V. Panfilov and J.P. Keener. Re-entry in three−dimensional myocardium with rotational anisotropy. Physica D, 84:545–552, 1995.

[79] A.V. Panfilov and A.N. Rudenko. Two regimes of the scroll ring drift in the three dimensional active media. Physica D, 28:215–218, 1987.

[80] AV Panfilov and BN Vasiev. Vortex initiation in a heterogeneous excitable medium. Physica D: Nonlinear Phenomena, 49(1–2):107–13, 1991.

[81] A.V. Panfilov and B.N. Vasiev. Vortex initiation in a heterogeneous excitable medium. Physica D, 49:107–113, 1991.

[82] AV Panfilov and AT Winfree. Dynamical simulations of twisted scroll rings in three-dimensional excitable media. Physica D, 17:323–30, 1985.

[83] CS Peskin. Fiber architecture of the left ventricular wall: An asymptotic analysis. Communications on Pure and Applied Mathematics, 42(1):79–113, 1989.

[84] J Pettigrew. On the arrangement of the muscular fibers of the ventricular portion of the heart of the mammal. Proc. Roy. Soc., London, 10:433–440, 1860.

[85] JM Peyrat, M Sermesant, X Pennec, H Delingette, C Xu, E McVeigh, and N Ayac. Towards a statistical atlas of cardiac fiber structure. LNCS, 4190:297–304, 2006.

[86] JM Peyrat, M Sermesant, X Pennec, H Delingette, C Xu, ER McVeigh, and N Ayache. A computational framework for the statistical analysis of cardiac diffusion tensors: application to a small database of canine hearts. IEEE Transact on Med Imag, 26(11):1500–1514, 2007.

[87] SF Pravdin. Non-axisymmetric mathematical model of the cardiac left ventricle anatomy. Russian Journal of Biomechanics, 17(4):75–94, 2013.

[88] SF Pravdin, VI Berdyshev, AV Panfilov, LB Katsnelson, O Solovyova, and VS Markhasin. Mathematical model of the anatomy and fibre orientation field of the left ventricle of the heart. Biomedical Engineering Online, 54(12):1–21, 2013.

[89] SF Pravdin, H Dierckx, LB Katsnelson, O Solovyova, VS Markhasin, and AV Panfilov. Electrical wave propagation in an anisotropic model of the left ventricle based on analytical description of cardiac architecture. PLOS One, 9(5):e93617, 2014. doi:10.1371/journal.pone.0093617.

[90] SF Pravdin, H Dierckx, VS Markhasin, and AV Panfilov. Drift of scroll wave filaments in an anisotropic model of the left ventricle of the human heart. Biomed Research International Journal (Hindawi), 2015. submitted on 28.11.2014.

[91] Zhilin Qu, Jong Kil, Fagen Xie, Alan Garfinkel, and James N. Weiss. Scroll wave dynamics in a three-dimensional cardiac tissue model: Roles of restitution, thickness, and fiber rotation. Biophysical Journal, 78(6):2761–2775, 2000.

[92] Punit Ramrakha and Jonathan Hill, editors. Oxford Handbook of Cardiology. Oxford University Press, 2nd edition, 2012.

[93] JJ Rice and PP de Tombe. Approaches to modeling crossbridges and calcium-dependent activation in cardiac muscle. Prog Biophys Mol Biol., 85(2-3):179–195, 2004.

[94] JS Robb and RC Robb. The normal heart. anatomy and physiology of the structural units. Am Heart J., 23:455–467, 1942.

[95] B Rodriguez, L Li, JC Eason, IR Efimov, and NA Trayanova. Differences between left and right ventricular chamber geometry affect cardiac vulnerability to electric shocks. Circ Res., 97(2):168–175, 2005.

[96] A. N. Rudenko and A. V. Panfilov. Drift and interaction of vortices in two-dimensional heterogeneous active medium. Studia Biophysica, 98:183–188, 1983.

[97] AN Rudenko and AV Panfilov. Drift and interaction of vortices in two-dimensional heterogeneous active medium. Studia Biophysica, 98:183–88, 1983.

[98] RF Rushmer, DK Crystal, and C Wagner C. The functional anatomy of ventricular contraction. Circ Res, 1:162–170, 1953.

[99] Faramarz H Samie and Jose Jalife. Mechanisms underlying ventricular tachycardia and its transition to ventricular fibrillation in the structurally normal heart. Cardiovascular Research, 50(2):242–250, 2001.

[100] P Schmid, P Niedered, PP Lunkenheimer, and F Torrent-Guasp. The anisotropic structure of the human left and right ventricles. Technol Health Care, 5:29–44, 1997.

[101] G Seemann. Modeling of Electrophysiology and Tension Development in the Human Heart. PhD thesis, Universitat Karlsruhe, 2005.

[102] TK Shajahan, S Sinha, and R Pandit. Spiral-wave dynamics depend sensitively on inhomogeneities in mathematical models of ventricular tissue. Phys Rev E Stat Nonlin Soft Matter Phys, 75:011929, 2007.

[103] Sitabhra Sinha, Kenneth M. Stein, and David J. Christini. Critical role of inhomogeneities in pacing termination of cardiac reentry. Chaos: An Interdisciplinary Journal of Nonlinear Science, 12(3):893–902, 2002.

[104] S Sridhar, S Sinha, and AV Panfilov. Anomalous drift of spiral waves in heterogeneous excitable media. Phys. Rev. E, 82:051908, Nov 2010.

[105] DDJR Streeter. Handbook of physiology. Sec. 2. Vol. I. The Heart, chapter Gross morphology and fiber geometry of the heart, pages 61–112. Bethesda, Maryland: Am. Physiol. Soc, 1979.

[106] T Sulman, LB Katsnelson, OE Solovyova, and VS Markhasin. Mathematical modeling of mechanically modulated rhythm disturbances in homogeneous and heterogeneous myocardium with attenuated activity of na+ - k+ pump. Bull Math Biol., 70(3):910–949, 2008.

[107] B Taccardi, E Macchi, R L Lux, P R Ershler, S Spaggiari, S Baruffi, and Y Vyhmeister. Effect of myocardial fiber direction on epicardial potentials. Circulation, 90(6):3076–90, 1994.

[108] K. H. W. J. ten Tusscher and A. V. Panfilov. Alternans and spiral breakup in a human ventricular tissue model. American Journal of Physiology - Heart and Circulatory Physiology, 291(3):H1088–H1100, 2006.

[109] K.H.W. ten Tusscher, Noble D., Noble P.J., and A.V. Panfilov. A model for human ventricular tissue. Am. J. Physiol. Heart Circ. Physiol., 286:1573–1589, 2004.

[110] HE ter Keurs, T Shinozaki, YM Zhang, ML Zhang, Y Wakayama, Y Sugai, Y Kagaya, M Miura, PA Boyden, BD Stuyvers, and A Landesberg. Sarcomere mechanics in uniform and non-uniform cardiac muscle: a link between pump function and arrhythmias. Prog Biophys Mol Biol., 97(2-3):312–331, 2008.

[111] F Torrent-Guasp. The Cardiac Muscle. Madrid: Fundacion Juan March, 1973.

[112] F Torrent-Guasp. Zarco P, Perez J (eds) El Fallo Mecnico del Corazon, chapter Organizacion de la musculatura cardiaca ventricular, pages 3–36. Ediciones Toray, Barcelona, 1975.

[113] F Torrent-Guasp, WF Whimster, and K Redman. A silicone rubber mould of the heart. Technol Health Care, 5:13–20, 1997.

[114] Francisco Torrent-Guasp, Mladen J Kocica, Antonio F Corno, Masashi Komeda, Francesc Carreras-Costa, A Flotats, Juan Cosin-Aguillar, and Han

Wen. Towards new understanding of the heart structure and function. European Journal of Cardio-thoracic Surgery, 27:191–201, 2005.

[115] NA Trayanova, J Constantino, and V Gurev. Electromechanical models of the ventricles. Am J Physiol Heart Circ Physiol, 301:H279–H286, 2011.

[116] Natalia A. Trayanova and Patrick M. Boyle. Advances in modeling ventricular arrhythmias: from mechanisms to the clinic. Wiley Interdisciplinary Reviews: Systems Biology and Medicine, 2013.

[117] ML Trew, BJ Caldwell, GB Sands, IJ LeGrice, and BH Smaill. Three-dimensional cardiac tissue image registration for analysis of in vivo electrical mapping. Ann Biomed Eng, 39(1):235–248, 2011.

[118] KH Ten Tusscher, R Hren, and AV Panfilov. Organization of ventricular fibrillation in the human heart. Circ. Res., 100:87–101, 2007.

[119] KH Ten Tusscher and AV Panfilov. Alternans and spiral breakup in a human ventricular tissue model. Am. J. Physiol. Heart Circ. Physiol., 291:H1088–1100, 2006.

[120] KHWJ Ten Tusscher, D Noble, PJ Noble, and AV Panfilov. A model for human ventricular tissue. Am. J. Physiol. Heart Circ. Physiol., 286:H1573–H1589, 2004.

[121] F Vadakkumpadan, H Arevalo, AJ Prassl, and et al. Image-based models of cardiac structure in health and disease. Wiley Interdiscip. Rev. Syst. Biol. Med., 2(4):489–506, 2010.

[122] H Verschelde, H Dierckx, and O Bernus. Covariant stringlike dynamics of scroll wave filaments in anisotropic cardiac tissue. Physical Review Letters, 99(16), 2007.

[123] H. Verschelde, H. Dierckx, and O. Bernus. Covariant stringlike dynamics of scroll wave filaments in anisotropic cardiac tissue. Phys. Rev. Lett., 99:168104, 2007.

[124] FJ Vetter and AD McCulloch. Three-dimensional analysis of regional cardiac function: a model of rabbit ventricular anatomy. Prog Biophys Mol Biol, 69(2-3):157–183, 1998.

[125] Y W Vicky. Modelling In Vivo Cardiac Mechanics using MRI and FEM. PhD thesis, Auckland Bioengineering Institute, The University of Auckland, New Zealand, 2012.

[126] EJ Vigmond, R Weber dos Santos, AJ Prassl, M Deo, and G Plank. Solvers for the cardiac bidomain equations. Progress in Biophysics and Molecular Biology, 96(13):3–18, 2008.

[127] M. Wellner, O.M. Berenfeld, J. Jalife, and A.M. Pertsov. Minimal principle for rotor filaments. P Natl Acad Sci USA, 99:8015–8018, 2002.

[128] AA Young and AF Frangi. Computational cardiac atlases: from patient to population and back. Exp Physiol, 94(5):578–596, 2009.

[129] RJ Young and AV Panfilov. Anisotropy of wave propagation in the heart can be modeled by a riemannian electrophysiological metric. Proc. Natl. Acad. Sci. USA, 107:14964–14967, 2010.

[130] R.J. Young and A.V. Panfilov. Anisotropy of wave propagation in the heart can be modeled by a riemannian electrophysiological metric. Proc Natl Acad Sci USA, 107:15063–8, 2010.

[131] Yongjie Zhang, Xinghua Liang, Jun Ma, Yiming Jing, Matthew J. Gonzales, Christopher Villongco, Adarsh Krishnamurthy, Lawrence R. Frank, Vishal Nigam, Paul Stark, Sanjiv M. Narayan, and Andrew D. McCulloch. An atlas-based geometry pipeline for cardiac hermite model construction and diffusion tensor reorientation. Medical Image Analysis, 16(6):1130–1141, 2012.

[132] V.S. Zykov and S.C. Müller. Spiral waves on circular and spherical domains of excitable medium. Phys D, 97:322–332, 1996.